EXPERIMENTAL EVALUATION OF ROTOR MOTION WITH RADIAL RUB

by

NITINDRA R. JOGLEKAR
B.Tech (Hons), I.I.T., Kharagpur, India (1977)
M.Eng., Memorial University, St. Johns, Canada (1985)

SUBMITTED IN PARTIAL FULFILLMENT
OF THE REQUIREMENTS FOR THE
DEGREE OF

MASTER OF SCIENCE IN OCEAN ENGINEERING
and
MASTER OF SCIENCE IN MECHANICAL ENGINEERING

at the

MASSACHUSETTS INSTITUTE OF TECHNOLOGY

June 1987

Signature of Author_____
Department of Ocean Engineering
June 1987

Certified by_____
Professor J. Kim Vandiver
Thesis Supervisor

Certified by_____
Professor Richard H. Lyon
Thesis Reader

Accepted by_____
Professor A. Douglas Carmichael, Chairman
Ocean Engineering Department Graduate Committee

Accepted by_____
Professor Ain Sonin, Chairman
Mechanical Engineering Department Graduate Committee

EXPERIMENTAL EVALUATION OF ROTOR MOTION WITH RADIAL RUB

by

NITINDRA R. JOGLEKAR

Submitted to the Departments of Ocean Engineering and Mechanical Engineering in June 1987 in partial fulfillment of the requirements for the degrees of Master of Science in Ocean Engineering and Master of Science in Mechanical Engineering.

ABSTRACT

A single degree of freedom model incorporating normal and tangential forces caused by rubbing predicts the regions of full synchronous rub. An extension of this model predicts the stiffness modification effects caused by the rubbing between a drill string and its enclosing casing. In this investigation experimental studies have been carried out to study the behavior a planar model, a disc rotating within a casing, as well as a drill string model that has a shaft whirling and rubbing within a fluid-filled casing.

The design, construction, and testing of the planar model are described. The tests show that the theoretical model predicts the speed of initiation of rub and the region and the type of rubbing accurately. It is also learned that the real system shows a considerable amount of partial rub at rotation rates just below and above the synchronous rub range. The stiffness modification effects for speeding up and slowing down the rotor are different.

The design, construction, and testing of the drill string model are described and plots of X versus Y orbits and spectra of the displacement time series are presented. The nature of the rubbing phenomena is discussed and added mass coefficient is calculated from the shift in the natural frequency of the system.

Thesis Supervisor: J. Kim Vandiver
Title: Professor of Ocean Engineering

ACKNOWLEDGEMENTS

I wish to express my gratitude to Professor J. Kim Vandiver for his guidance and for all the help and support I have received in the past two years.

I want to thank Professor Lyon for reading this thesis. I am grateful to Professor Steven Crandall for allowing me to work on his experimental set up and for the benefit of his advice on rotor dynamic modelling.

Thanks are due to Mrs. Sheila McNary for typing the manuscript. I am also indebted to fellow graduate students at the Acoustics and Vibration Laboratory and at the Arctic Acoustics Laboratory for the help during the course of the research. Edward Cashman has carried out the construction and testing of the drill string model.

My friends Kumar and Apurva have been a constant source of help and encouragement. Finally, to my parents, for all the years of love and support - thank you.

TABLE OF CONTENTS

CHAPTER 1: INTRODUCTION

The flexural vibrations of a shaft undergoing rotating motion are potential problems in a wide variety of machines. If the shaft is enclosed by a casing, then these vibrations are constrained, leading to motions accompanied by rubbing. In general the contact is intermittent during each cycle of the shaft whirl, and the motion is termed as partial rub. When the shaft is fully in contact with the casing, it is said to undergo radial or full annular rotor rub.

Flexural vibrations can arise due to a number of sources. Any imbalance in the shaft causes a rotating force synchronous with the running speed, which leads to whirling. Other sources of vibrations are traceable to instabilities in the system. For instance, self-excited vibrations may be caused by the interaction of the system with the fluid bearings. In the simplest case, flexural vibrations without rubbing can be predicted by a single degree of freedom system model accounting for the rotor mass, stiffness, damping, and the imbalance represented by the eccentricity. This is called the Jeffcott Model.

The dynamics of rotor motion accompanied by rub involves the effects of system geometry (clearance) as well as the rubbing forces. Stackley (1986) has attempted to model the full annular synchronous rub by including the normal (reaction) and tangential (frictional) forces at the point of contact. This study showed that the radial rub leads to a modification in the system stiffness, and that it results in synchronous rubbing over a wider range of speed, than would be expected by using the Jeffcott Model.

In the research presented here an experimental investigation has

been carried out to study the behavior of the system over a range of speeds close to the critical speed. The objective of this study is to understand the mechanism of rotational motion accompanied by rubbing, and ascertain the range of validity for the radial rub model. Further, the intent of this thesis is to apply the radial rub model to the vibration analysis of a drill string. Thus the rotor rub is studied with the presence of fluid in the annular space.

In the first part of this thesis, analytical and experimental work involving whirling and rubbing has been reviewed. The nature of the forces dominating the response is discussed and the full annular synchronous rub is studied experimentally as a two-dimensional model. The finding of this study is that the full annular synchronous rub model predicts the behavior closely, but the real system also shows a considerable amount of partial rub at rotation rates just below and above the synchronous rub range.

The second part of the thesis deals with the experimental study of a three-dimensional drill string model that incorporates fluid in the annular space. The nature of whirling accompanied by rubbing is examined, and the added mass coefficient is computed from the experimental data.

CHAPTER 2: BACKGROUND

2.1 Motivation

The problem of shaft rotation accompanied by whirling has been studied by designers and operators of rotating machines for an appropriate choice of clearance between the high speed rotor and its enclosure. In general, a reduction in the clearance increases the system efficiency but also increases the possibility of rubbing. Certain types of turbomachines have been built with rubbing as a design condition. The need for better understanding of the rubbing phenomena is well established.

The motivation for this particular investigation comes from the application of the classical rotor dynamics model to the analysis of the down hole drilling devices used by the oil industry. The drilling unit consists of a long rotary shaft that tends to whirl and rub against the bore hole.

The distinguishing features of the drill string rotor dynamics need some elaboration. The drill string has a large aspect ratio l/κ (length/radius of gyration) compared to normal rotor (see Table 1). The fluid in the annular space is viscous. The clearance (r_c) to diameter (d) ratio is small and the casing can be viewed as a rigid boundary. The comparison of the properties of a typical machine rotor and a drill collar between the bit and the first stabilizer are given in Table 1.

Table 1
Comparison of an Example Drill Collar to a Typical Machine Rotor

Item	Drill String	Typical Rotor
l/κ	108	23 (l/d = 1 at the bearing)
$r_{c/d}$	0.17	0.29 (at the bearing)
Fluid Viscosity	0.175 poise	0.96×10^{-4} poise
Natural Frequency	0.81 Hz	36.71 Hz
Reference	Belkheria (1986)	Subbiah et al (1985)

2.2 Literature Review

The state of the art of rotor dynamic analysis and testing is well established. Interested readers may refer to the body of references and texts cited in the Bibliography. The investigation of rotor rub is comparatively a new area.

Ehrlich (1969) studied the dynamic stability of radial rub and computed whirl frequencies as a function of rotor and natural frequency and damping. He got a general qualitative agreement between his calculations and a simple experimental model. Stability criteria for the motion was established.

Childs (1981) simulated the fractional frequency responses of rotor due to non-symmetric clearance (partial rubbing). There has been considerable data available on forced subharmonic dynamic behavior of rotors. (Refer Ehrlich (1966), Childs (1978), Bentley (1979).)

Kasack and Tomko (1980) carried out numerical studies on smearing rub models and demonstrated the existence of a threshold which when exceeded caused rotors to proceed in backward whirl.

Experimental investigation of these phenomena are few. Matsushita et al (1982) studied the vibrations of rotors caused by

external excitation and rub. Their model also demonstrated backward whirl. Experimental simulation of backward whirl has also been presented by Subbiah et al (1985).

A very comprehensive study of partial as well as full rub has been reported by Muszynska (1984, 1985). The results of this work are very instructive in terms of understanding the partial rub. She has presented experimental evidence to demonstrate the modification in the system stiffness caused by rubbing. Some of these findings are discussed in Appendix A.

A recent thesis by Stackley (1986) has studied the analytical modelling of full annular rotor rub. It models the rotor as a two-dimensional disc. This thesis has been used as the basis of the first part of the experiments dealing with a two-dimensional study. The findings of this thesis are incorporated in the next chapter.

All of the literature deals with the classical rotor and not with drill strings. While the basic theory is valid for the rubbing of a drill string, no directly applicable experimental work has been carried out.

The theoretical analysis of drill string vibration is also quite recent. Most studies have emphasized longitudinal and torsional vibration. Very few attempts at analyzing whirling with or without rub have been made. Vandiver (1985) presented a basis for the dynamic analysis of the unbalanced, 'Woodpecker' drill collar. Following that, Belkheria's thesis (1986) was the maiden attempt to numerically study the effects of rubbing on the drill string vibrations. His thesis forms the background for the second part of the experiments in which a flexible rod is allowed to whirl within a casing. The

findings are presented in Chapter 6.

There is hardly any literature covering the hydrodynamic effects of the fluid in the confined space on the drill string vibrations. Chen et al (1976) have presented a model for the added mass and damping of a vibrating rod in a confined fluid, as well as some experimental results.

Very little data is available on the measurement of friction and wear of drill strings. Bol (1986) has presented some data on the friction between the casing and the tool joints.

CHAPTER 3: FULL ANNULAR RUB

3.1 General Formulation

The configuration of this model is shown in Figure 1. The rotating element consists of a disc of mass M , mounted on a laterally flexible but torsionally rigid shaft of stiffness K . The shaft is supported on rigid bearings (B) without clearance. In the plane of the disc, the radially symmetrical clearance is r_c. The casing is rigid. The damping of the rotor is D . The natural frequency of this system is

$$\omega_n = \sqrt{\frac{K}{M}}$$

The imbalance in the system is characterized by the eccentricity (δ). Both radial and longitudinal symmetry are assumed, so that the model may be analyzed as a planar situation. The effects of the force of gravity are neglected. Effects of the fluid in the annular space are not considered in this case. It is assumed that the rotor is driven at a constant speed ω.

First the dynamic response of the unconstrained rotor is discussed. This is the so-called Jeffcott model. Subsequently the response with a full annular rub is analyzed under the assumption that when the rotor goes into rub it is in constant contact with the casing. Finally, the special situation of backward whirl is considered.

3.2 The Jeffcott Model

Figure 2 demonstrates the nature of unconstrained motion. The forces that come into play are elastic, damping and centrifugal forces which are balanced by the inertial force.

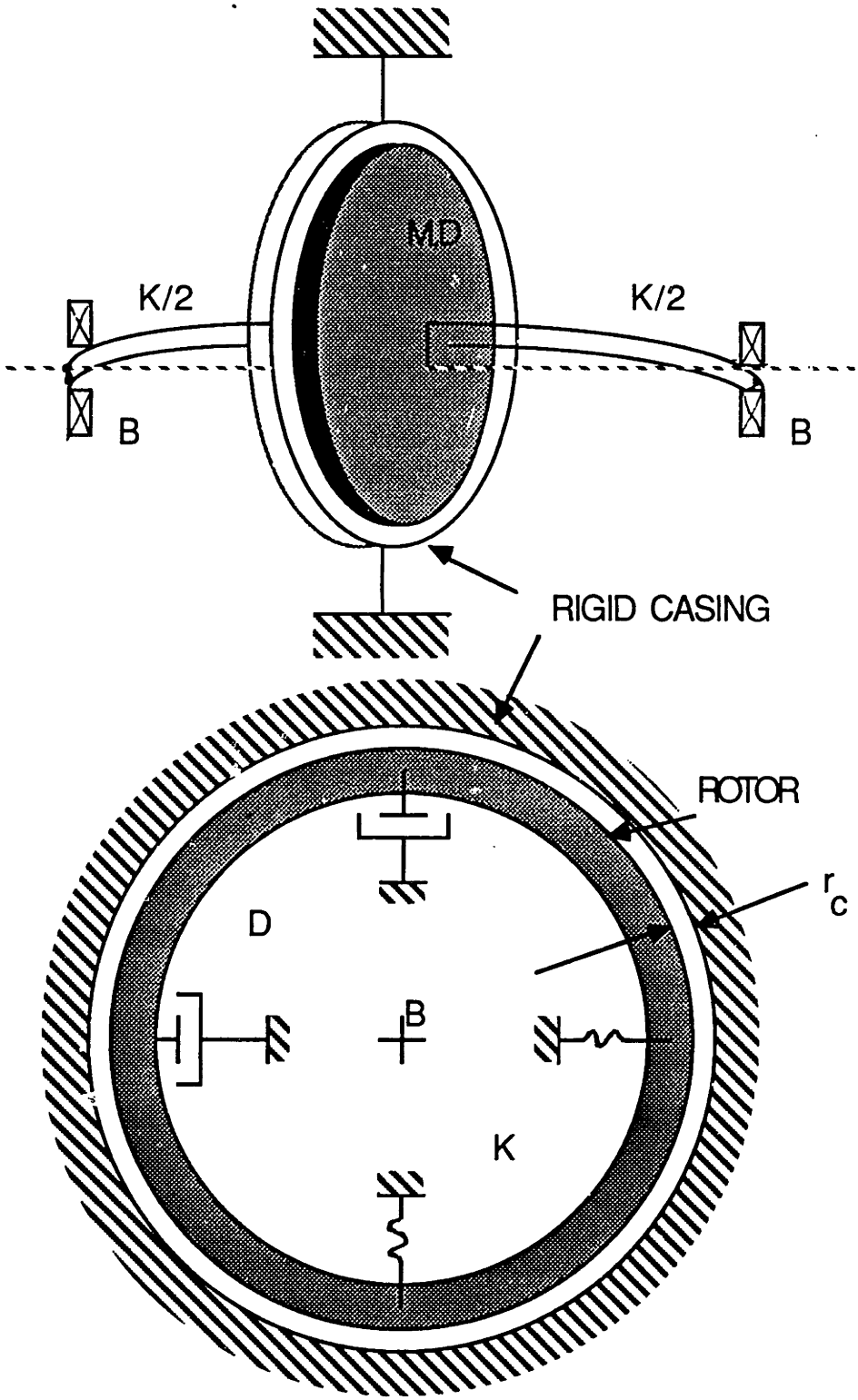

FIGURE 1: PLANAR MODEL

The centrifugal force is caused by the mass imbalance. It acts at the center of gravity in a direction that is radially outward from the bearing axis. The elastic force acts at the rotor center, radially inward from the bearing axis. The damping force acts in a manner so as to resist the translational motion of the rotor.

Let the frame of reference XY be fixed at the bearing axis as shown in Figure 2. Defining z (a complex number) as the time dependent position of the rotor center (C), and z_g as the instantaneous location of the center of gravity of the rotor. Then the equation of motion is

$$M\ddot{z}_g + D\dot{z}_c + Kz_c = 0 \tag{1}$$

but

$$z_g(t) = z_c(t) + z_{gc}(t)$$

$$z_{gc}(t) = \delta e^{j\omega t}$$

where δ is the eccentricity and harmonic motion at frequency is assumed. Therefore the free dynamics of the rotor is characterized by a single degree of freedom system given by

$$M\ddot{z}_c + D\dot{z}_c + Kz_c = M\omega^2\delta e^{j\omega t} \tag{2}$$

The response is maximum in the vicinity of the natural frequency (ω_n) which is often referred to as the critical speed. Clearly, the system must have sufficient damping in order to avoid an unacceptabally large response.

3.3 Constrained Dynamics

If the rotor displacement $|z_c|$ is less than the radial clearance the Jeffcott model is applicable. As soon as the displacement equals the clearance, it is assumed that full annular rub is established.

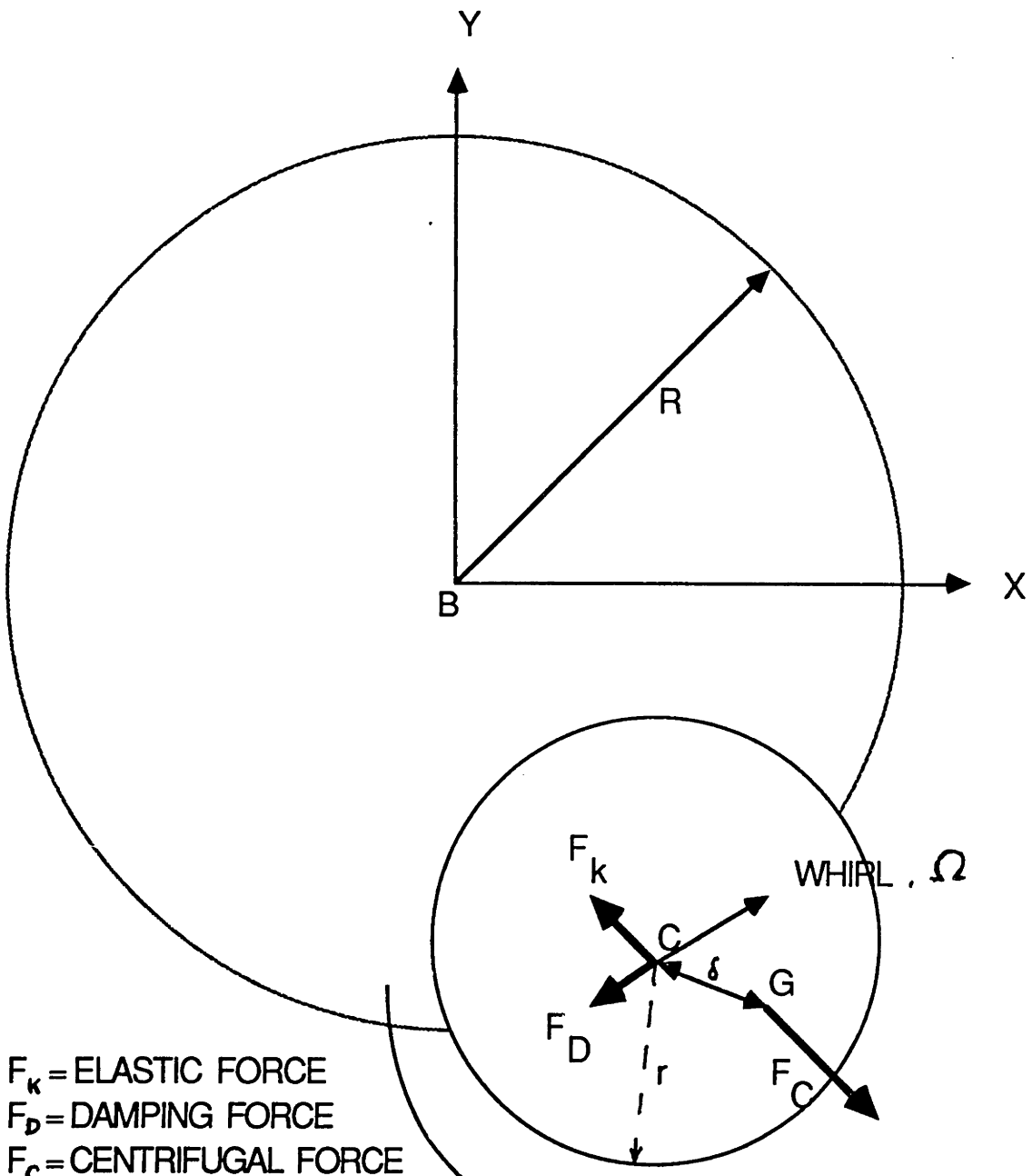

F_K = ELASTIC FORCE
F_D = DAMPING FORCE
F_C = CENTRIFUGAL FORCE
R = RADIUS OF WHIRL
r = RADIUS OF DISC
B = BEARING AXIS
C = INSTANTANEOUS CENTER OF DISC
G = CENTER OF GRAVITY

FIGURE 2: WHIRLING OF AN UNCONSTRAINED ROTOR

The model for this situation is shown in Figure 3, where N is the normal force and μ is the coefficient of friction. The equation of motion assuming synchronous precession is:

$$M\ddot{z}_c + D\dot{z}_c + Kz_c = M\ddot{z}_{gc} - (N+j\mu N)e^{i\omega t} \tag{3}$$

The frictional force can be interpreted as an additional load on the machine. Introducing the non-dimensional constants

$\varepsilon = \delta/r_c$: the eccentricity ratio

$n = N/Kr_c$: the normalized reaction force

$\zeta = D/2M\omega_n$: the damping ratio

$\beta = \omega/\omega_n$: the normalized rotor speed

then the normalized displacement is:

$$\frac{z_c(t)}{r_c} = \frac{[\varepsilon\beta^2 - (n+j\mu n)]e^{j\omega t}}{[(1-\beta^2) + j(2\zeta\beta)]} \tag{4}$$

Since rub is imposed, the left hand side of equation (4) has a unit magnitude. This leads to values of n in terms of ε, β, ζ, and μ as:

$$n = \frac{-(1-\beta^2+2\zeta\beta\mu) \pm \{(1-\beta^2+2\zeta\beta\mu)^2 - (1+\mu^2)\,((1-\beta)^2+(2\zeta\beta)^2 - \varepsilon^2\beta^4)\}^{1/2}}{(1+\mu^2)} \tag{5}$$

Only the values of n greater than zero are physically meaningful. The speed at which the rub initiates is computed from the condition n=0.

$$\beta_{rub} = \frac{(2\zeta^2-1) + [(2\zeta^2-1)^2 + (\varepsilon^2-1)]^{1/2}}{\varepsilon^2-1} \tag{6}$$

Figure 4(a) shows that for rotor speeds $\beta_{rub} < \beta < \beta'$ the rotor is assumed to be in contact with the casing. Depending upon the system's damping ratio, displacement to clearance ratio and the friction coefficient the rotor response can be characterized as one of the following. The value of β' can be computed numerically from equations

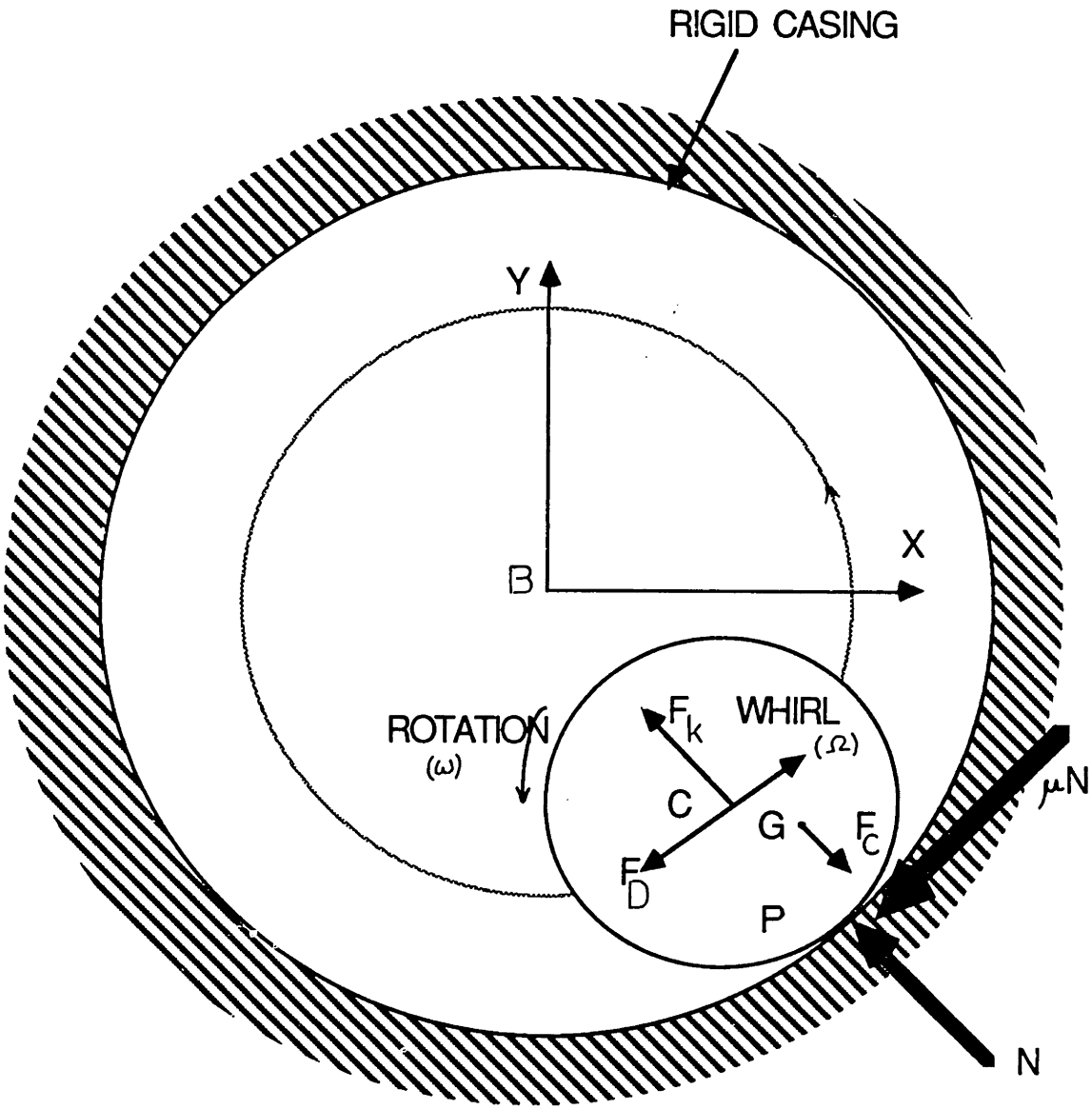

FIGURE 3: FULL ANNULAR RUB MODEL

(2), (3), and (4).

i. Limited synchronous rub:

$$2\zeta < \varepsilon < \frac{\mu}{(1+\mu^2)^{1/2}}$$

The rub is initiated at β_{rub}. Any further increase in speed leads to an increase in the normal force (and a larger frictional force). Larger friction force and damping causes a decrease in whirl amplitude, loss of contact, and a disruption in the rub orbit. The system comes out of rub to follow the action of a free rotor. This is shown in Figure 4(a).

ii. Synchronous rub limited discontinuity:

$$\frac{\mu}{(1+\mu^2)^{1/2}} < \varepsilon < \frac{\zeta^2 + \mu^2}{\mu(1+\mu^2)^{1/2}}$$

For values of μ, ζ and ε the system in this range will exhibit a limited synchronous rub (Figure 4(b)), but on further increasing the speed the dynamic conditions may cause it to go into stable synchronous rub. At higher speed some perturbation is needed to initiate the rub. In certain cases, reverse whirl is also possible (see section 3.4).

iii. Continuous synchronous rub:

$$\varepsilon > \frac{\zeta^2 + \mu^2}{\mu(1+\mu^2)^{1/2}}$$

If the damping and friction are not sufficiently high the rotor will continue to rub indefinitely (as shown in Figure 4(c)).

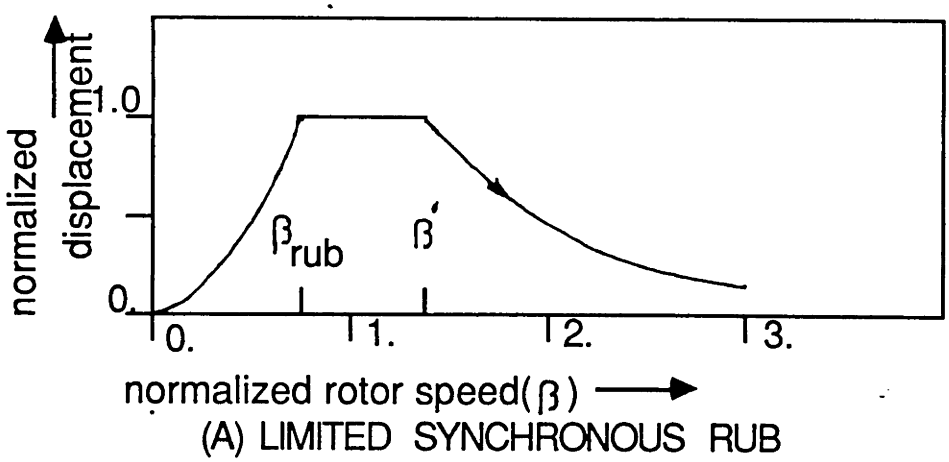

(A) LIMITED SYNCHRONOUS RUB

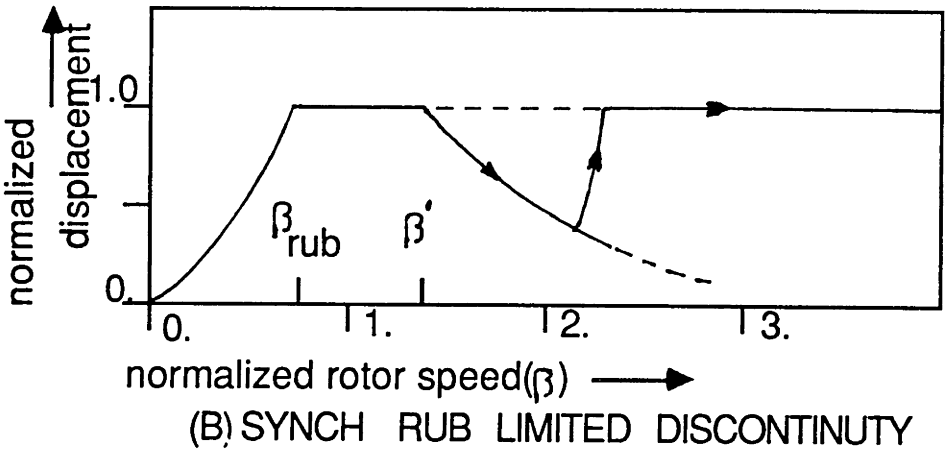

(B) SYNCH RUB LIMITED DISCONTINUTY

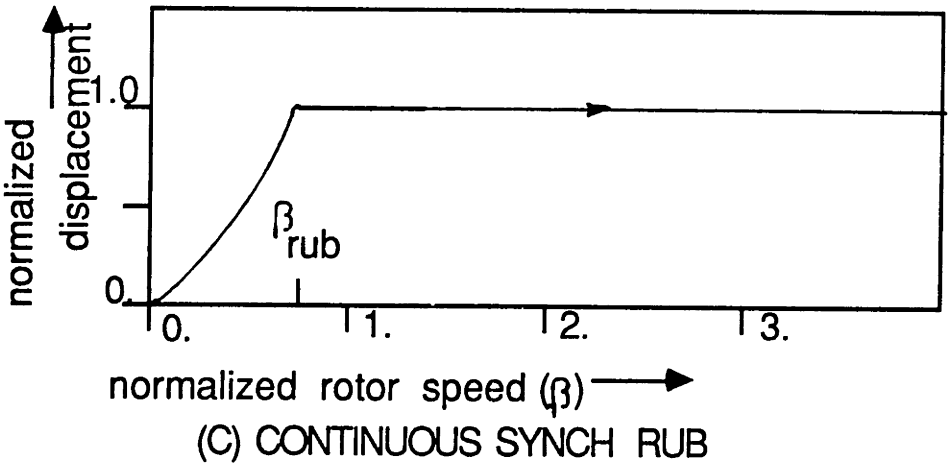

(C) CONTINUOUS SYNCH RUB

FIGURE 4 : TYPES OF FULL ANNULAR RUB

3.4 Reverse Whirl

The reverse synchronous whirl is witnessed when the direction of the rotor precession about the center of the casing is opposite the direction of rotation of the rotor about its own axis. The rotor rolls without slipping around the wall.

In the tangential direction the friction force is balanced by the damping force:

$$\mu N = D r_c \Omega \tag{7}$$

In the radial direction:

$$M r_c \Omega^2 = N + K r_c \tag{8}$$

Defining

Ω = whirl velocity -

$f = \Omega/\omega$ = normalized whirl velocity

Then

$$\mu n = 2\zeta\beta f \tag{7a}$$

$$f^2\beta^2 = n+1 \tag{8a}$$

ω and Ω are kinematically related through the slip condition.

The slip ratio S is defined as

$$S = \frac{\text{Rotor Whirl Speed}}{\text{Rotor Whirl Speed Without Slip}} = -\frac{\Omega}{(\frac{r}{r_c})\omega}$$

from equations (7) and (8):

$$\mu n = 2\zeta\beta(\frac{r}{r_c}) \tag{7b}$$

$$(\frac{r}{r_c})^2 \beta^2 = n+1 \tag{8b}$$

Solving for β, from equations 7(b) and 8(b):

$$\mu\{[\frac{rS}{r_c}]^2 \beta^2 - 1\} = 2\zeta\beta(\frac{rS}{r_c})$$

Then

$$\beta_{reverse} = (\frac{\zeta+(\zeta^2+\mu^2)^{1/2}}{\mu})(\frac{r_c}{r} \cdot \frac{1}{S}) \tag{9}$$

This is the critical speed above which reverse whirl is possible.

where

β is the normalized speed

r_c is the clearance

r is the radius of the rotor

S is the slip ratio

ζ is the damping ratio

μ is the coefficient of friction

For a given problem r_c and d are fixed. The effects of μ , ζ, and S on the occurrence of backward whirl are examined.

A. Let μ and ζ be constant

In this case the rub will be governed by the occurrence of slip. The slip ratio S is defined with the help of a kinematic relation between ω (the rotational angular velocity) and Ω (the angular velocity of whirl). The slip ratio is very difficult to determine experimentally. The useful concepts to remember of course are

i. $\beta_{reverse}$, the velocity for initiation of backward whirl is inversely proportional to slip ratio. In other words, an increase in the whirl speed due to slip will reduce the (threshold) speed at which backward whirl can be initiated.

ii. For no slip condition (s=1):

$$\Omega r_c = r\omega$$

$$\beta_{reverse} = \frac{\omega}{\Omega} \left(\frac{\zeta+(\zeta^2+\mu^2)^{1/2}}{\mu}\right)$$

B. Let S be constant

In the equation (7b) the effect of friction and the damping ratio

on the whirl are dependent on the actual value of n and Ω. Assuming that S is constant, the nature of response for relative values of μ and ζ is examined:

1. If $\zeta >> \mu$ (the damping is much larger than the frictional force), $\beta_{reverse}$ will be proportional to ζ. And since ζ is larger than μ (which is of the order of 0.3-0.5), $\beta_{reverse}$ will be quite high.

2. If $\zeta \simeq \mu$

   then $\beta_{reverse} \simeq (1+\sqrt{2})(\frac{r_c}{rS})$

3. If $\zeta < \mu$

   then $\beta_{reverse} \geq (\frac{r_c}{rS})$

In no slip condition (s=1),

For a typical drill collar (see Table 1), $\frac{r_c}{r} \simeq 0.35$

For a typical drill collar, backward whirl due to rubbing in first mode ($\beta \simeq 1$) is possible if $\zeta \leq \mu$. In general, μ (0.3 or more) is greater than ζ for drill string operations. It is therefore concluded that backward whirl is a distinct possibility for a drill collar during full annular rub.

A general comment is offered here about the original equations (7, 8). It is assumed that in backward whirl the damping force exactly balances the frictional force. The amount of damping force depends on slip. The magnitude of the frictional force (μN) is such that it compensates the damping. Thus the amount of friction varies with the amount of slip. The extreme value of frictional force is of course limited by the nature of the joint. If the damping force were to increase any further, the friction force will not be sufficient to maintain this assumed equilibrium. However, an increased damping force will lead to forward whirl and then this type of interpretation

will not be valid.

Finally, for a given set of values of r_c and r it is possible from equations (7) and (8) to plot a family of curves for different values of μ, ζ and S. This will indicate the (threshold) drive speeds above which backward whirl is feasible during full annular rub. Prediction of backward whirl ought to be the prime concern for the bottom hole drilling studies. The rubbing experiments, such as the ones studies in this thesis, offer insight into the nature of the orbits and the key parameters μ, ζ and S.

It must be pointed out here that equation gives the value of drive speeds above which the full annular rubbing could lead to backward whirl. It is not possible, based on the present understanding of the problem, to predict precisely forward or backward whirl. This type of conclusion could be derived from a stability analysis of the equilibrium. It is suggested that this is a topic for future research.

3.5 Example

The computation of $\beta_{reverse}$ is illustrated here with the help of an example. This exercise gives the range of speeds for which backward whirl is not feasible and suggests the speeds at which either forward or backward full annular rub is feasible.

Input Data:

For the purpose of this illustration the full annular rub of a typical drill collar (described in Appendix D) is examined. The collar is expected to rub while in the first mode of vibration.

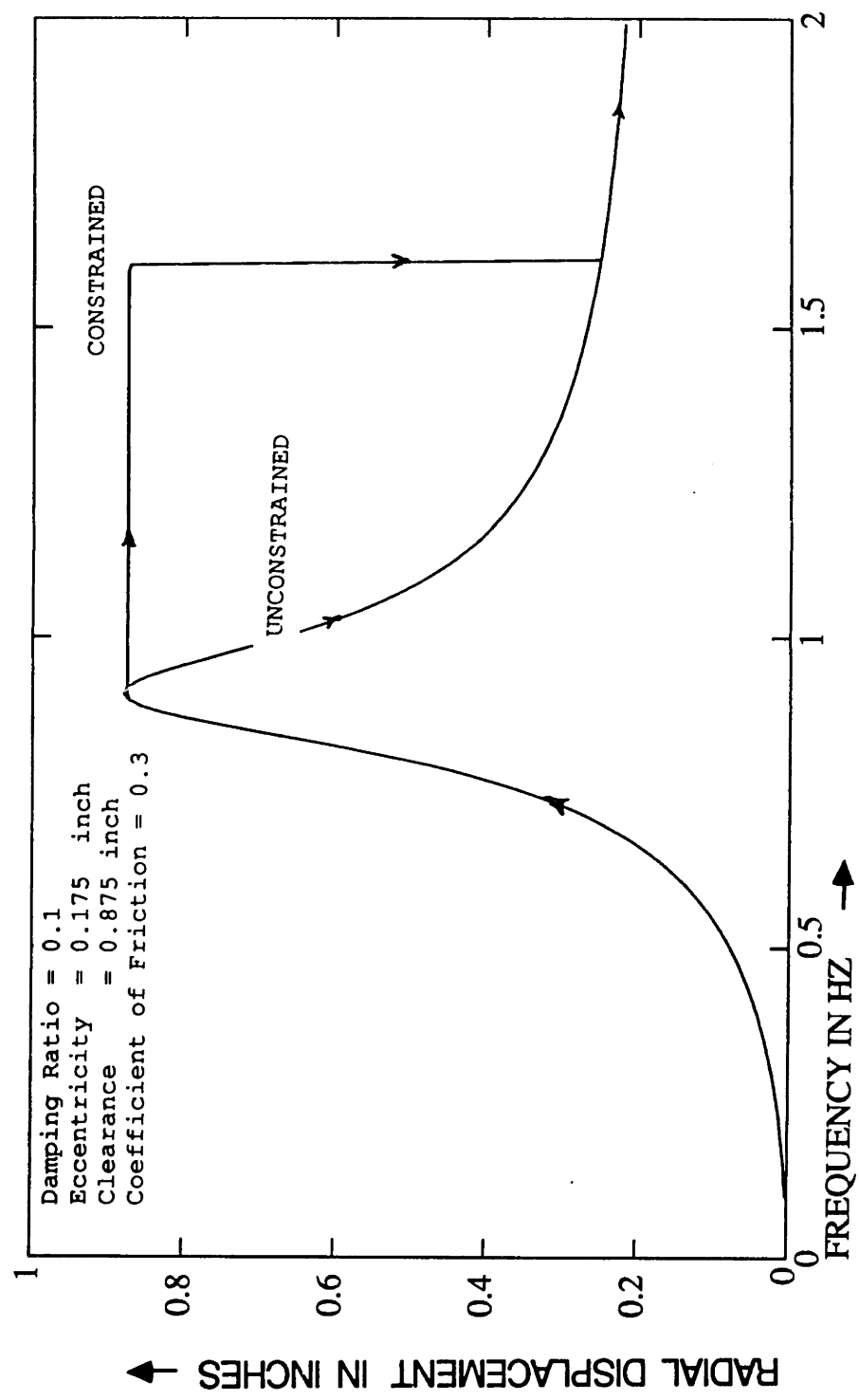

FIGURE : 5 RESPONSE OF THE DRILL COLLAR

1. Hole diameter = 8.75 inches
2. Rotor/Drill Collar diameter = 7.0 inches
3. (Assumed) modal damping ratio for the first mode = 0.1
4. (Assumed) effective eccentricity in the first mode = 0.175 inches (taken as 5% of the radius of the rotor)
5. Assumed coefficient of friction = 0.3
6. The natural frequency of the rotor = 0.9 Hz

Step I: Computation of the Range of Rubbing

Using equations (2) through (6) a sample analysis is carried out to establish the range of speeds at which the system is expected to rub. Figure 5 shows the unconstrained as well as constrained radial response of the rotor. It is seen that the rotor will go into full annular rub at 0.89 Hz drive speed (corresponds to $\beta = 0.98$) and come out of rub at the speed of 1.62 Hz (corresponds to $\beta = 1.8$).

Step II: Computation of $\beta_{reverse}$

From equation (9):

$$\beta_{reverse} = \left(\frac{r_c}{r}\right) \left[\frac{\zeta+(\zeta^2+\mu^2)^{1/2}}{\mu}\right] \frac{1}{S}$$

If S=1, this equation indicates that backward whirl is possible at any full annular rub for drive speeds corresponding to the nondimensional drive speed (β) greater than 0.3468. Since the full annular rub takes place between $\beta = 0.98$ and $\beta = 1.8$, backward whirl is a distinct possibility in this range. Further it is possible to compute the backward whirl speed as a function of slip ratio, S, as shown in Table 2.

TABLE 2

S	$\beta_{reverse}$	Ω
1.0	0.3468	$-4.0\ \omega$
0.75	0.4624	$-3.0\ \omega$
0.50	0.6936	$-2.0\ \omega$
0.25	1.3872	$-1.0\ \omega$

It is therefore concluded for the chosen values of (μ, ζ) that backward whirl is a distinct possibility for the drive speeds where the rotor goes into full annular rub. There is no known solution for specific values of slip ratio which will actually occur. The results indicate a continuum of possible solutions.

Step III: A Parametric Study

As hinted at the end of Section 3.4 it is useful to study the sensitivity of $\beta_{reverse}$ (threshold value for backward whirl) in terms of the geometry (clearance, rotor diameter) as well as the slip ratio (S), the coefficient of friction (μ), and damping ratio (ζ).

Table 3 shows the computed values of $\beta_{reverse}$ for different values of μ and ζ assuming S=1. (Since $\beta_{reverse} \alpha \frac{1}{S}$, the effect of variation of S is easy to guess.) This table shows that at low values of the coefficient of friction $[0.01 < \mu < 0.06]$ and high values of damping $(\zeta > 0.03)$, $\beta_{reverse}$ is greater than unity and thus the rotor will not experience backward whirl under these conditions.

The accurate estimation of the coefficient of friction and damping ratio and slip are very difficult. Table 3 shows that a wide range in parameters may lead to backward whirl.

TABLE 3 Computed $\beta_{reverse}$ Values for S=1

For ζ / μ	0.01	0.03	0.05	0.10	0.15	0.20
0.010	0.604	1.541	2.525	5.012	7.508	10.006
0.035	0.331	0.544	0.793	1.471	2.172	2.879
0.060	0.295	0.405	0.534	0.903	1.298	1.703
0.085	0.281	0.353	0.437	0.680	0.948	1.227
0.110	0.274	0.327	0.388	0.565	0.764	0.973
0.135	0.269	0.312	0.359	0.496	0.651	0.817
0.160	0.266	0.301	0.340	0.451	0.577	0.713
0.185	0.264	0.294	0.327	0.419	0.525	0.638
0.210	0.262	0.288	0.317	0.396	0.486	0.583
0.235	0.261	0.284	0.309	0.378	0.456	0.541
0.260	0.260	0.281	0.303	0.364	0.433	0.508
0.285	0.259	0.278	0.298	0.353	0.414	0.481
0.310	0.258	0.275	0.294	0.343	0.399	0.459
0.335	0.258	0.273	0.290	0.336	0.386	0.440
0.360	0.257	0.272	0.287	0.329	0.375	0.425
0.385	0.257	0.270	0.285	0.323	0.366	0.412
0.410	0.256	0.269	0.282	0.318	0.358	0.400
0.435	0.256	0.268	0.280	0.314	0.351	0.390
0.460	0.255	0.267	0.279	0.310	0.344	0.381
0.485	0.255	0.266	0.277	0.307	0.339	0.374
0.510	0.255	0.265	0.276	0.304	0.334	0.367

CHAPTER 4: EXPERIMENTAL STUDY OF PLANAR MODEL

4.1 General Description

The objective of this experiment has been prescribed as simulation of rotor dynamic rub in a planar model in order to study the nature of rubbing and demonstrate the validity of the full annular rub model.

The most attractive feature of the planar model of a high speed rotor is that it lends itself readily to visual study and filming, especially with the help of a strobe light. This type of study serves as a powerful learning method for the understanding of the rubbing mechanism. Detailed visual studies were carried out over a wide range of speeds.

Data on the rotor speed and the displacement of the shift in the X and Y directions was gathered simultaneously. This data was analyzed by making time domain orbital plots (X versus Y) and by computing response spectra of X and Y motion.

In this chapter the rationale behind the design of the model is discussed. It is followed by a brief description of the test set up and the instrumentation. The test matrix for the rubbing tests is presented. The methods of data acquisition and reduction are outlined.

4.2 Modelling

The reader may recall that a schematic diagram of the planar model capable of whirling (and rubbing) has been shown in Figure 1. The essential element of this model is a disc mounted on a flexible shaft. The shaft is simply supported on bearings. At zero speed the

disc sits concentrically within a rigid casing. The following features were identified as the requirements for a reasonable model:

(1) The system must model a single degree of freedom reponse as closely as possible.

(2) The system ought to be able to reach a speed that excites vibration well beyond its first natural frequency, but should not excite the second natural frequency.

(3) The system must have enough eccentricity to simulate a wide range of rub.

(4) All the flexibility must be achieved through the shaft. All the other elements must have a much greater stiffness.

(5) The rotor must be able to withstand the rubbing and wear.

(6) The bearings ought to have minimal clearance.

(7) Ease of measurement.

(8) Ease of visual study.

Ideally, the choice of dimensions and material properties are governed by the laws of similitude. In reality, however, compromises must be made to account for existing experimental equipment. The guiding factors in the choice of the various elements were:

(1) A fixed spacing of 30 inches between two existing bearings with 1/2" inch diameter.

(2) An existing drive unit with a 1 HP motor with a maximum speed of 6000 RPM.

(3) Two available non-contact proximity probes, which can sense steel surfaces 0.0 to 0.25 inches away.

(4) Maximum possible disc diameter was limited to 7 inches.

The actual design choices based on these factors were made

through an iterative procedure. A number of shafts (with different sizes and/or materials) were tried out, and the system was fine tuned for the best possible results. The final choice was a solid mild steel shaft with an outer diameter of 1/2 inch. It was decided that the disc be made of Lexan, an easily machineable plastic that has a very high stiffness and impact strength. The size of the rotor was chosen as 6 inches in diameter with (1/2 inch thickness). The casing was made from (1/2 inch thick aluminum plate. It was decided to have the largest possible clearance (0.1 inch) that could be accommodated by the dynamic range of the probes. Steel discs were mounted symmetrically on either side of the Lexan disc to reduce the critical speed to the vicinity of 15 Hz. The natural frequency of the shaft without discs is given by

$$\omega_n = (\frac{n\pi}{L})^2 \kappa C_L$$

where

L = span = 30 inches

κ = radius of gyration = 0.707 r = 0.176 inch

C_L = speed of sound = 2.04×10^5 in/sec

This leads to the first two natural frequencies

f_1 = 44.43 Hz

f_2 = 177.73 Hz

Therefore additional weight of 5.5 pounds was added to make the total weight of the rotor (shaft, steel, and Lexan discs) 10 pounds. This brings down the first natural frequency to 15 Hertz. The first and second natural frequencies are well separated.

4.3 Test Set Up

The layout of the experimental set up is shown in Figure 6. The rotor model was connected (through a flexible coupling) to a drive. The system is driven by a DC motor. The specifications of this motor is GE - Statotrol Motor Full Wave, 1 HP, 1750 RPM type CDL182 ACY (Model Number 5C 142FE009B005). A 1:3 step up in speed is obtained by introducing pulleys between the motor and the system. The motor control unit is configured as shown:

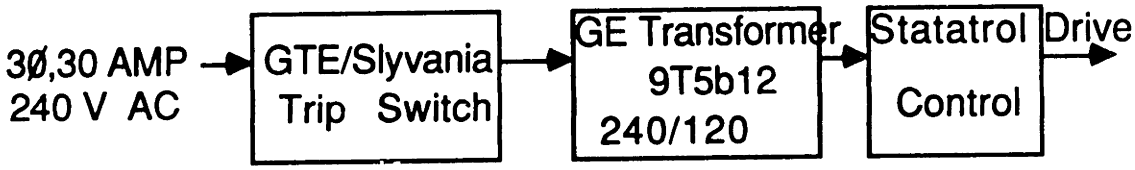

The instrumentation was configured as shown in Figure 7. The X and Y displacements were measured using non-contact proximity probes (Electro Mike - eddy current type).

Signals from the X and Y sensors were passed through low pass filters (cut-off frequency 300 Hz) to suppress the high frequency noise. All the signals were monitored on two oscilloscopes (to view the X versus Y as well as X and Y versus the time history).

Calibration tests were made on the set up with the help of an EG&G (Mode 117) signal generator. An HP 3542A spectrum analyzer was used to make spot checks on the nature of the signal.

Alternative vibration measurements were made with the help of a PCB impulse hammer and Wilcoxson accelerometers. The objective of the tests was to measure the natural frequency and the damping ratio of the rotor and to examine if the system (supports, casings, etc.) has any other resonance in the speed range of interest.

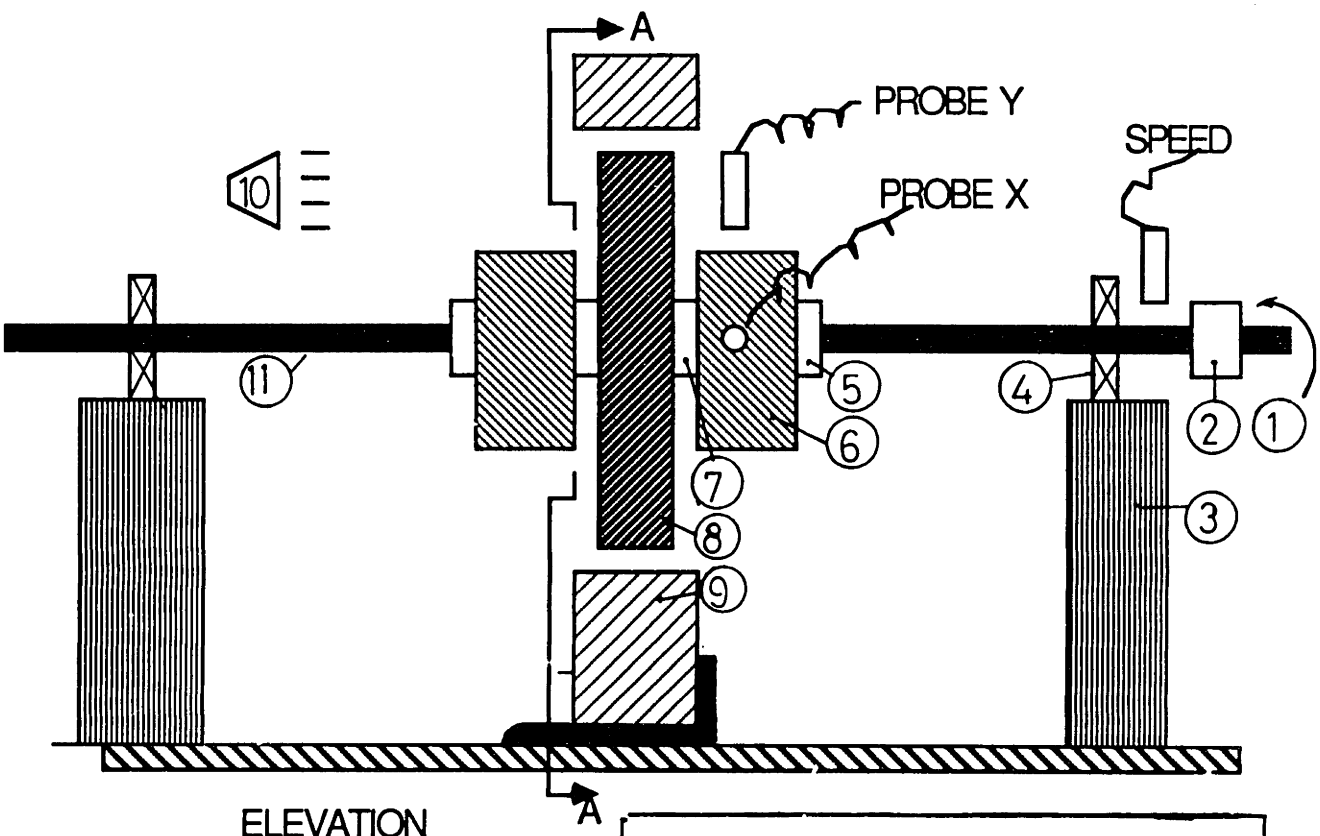

ELEVATION

VIEW 'AA'

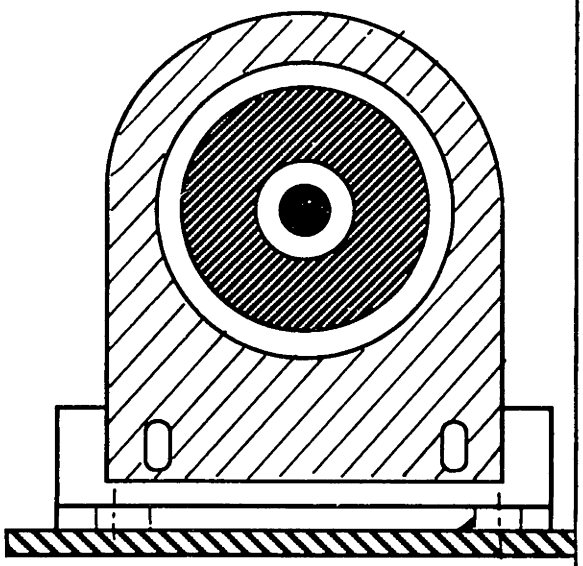

NOT TO SCALE

#	Part	Detail
1	Drive	: See Section 4.1
2	Flexible Coupling	: 0.5 id, 0.75 od
3	Mounting	:Adjustable in XY Plane
4	Bearing	: 0.5 id, self lub
5	Locking Collar	:0.5 id, 0.75 od
6	Steel Disc	:0.5 id, 4.0 od, w = .8
7	Flange Coupling with set screws	
8	Lexan Disc	: 0.5 id, 6.0 od, w = .5
9	Alum Casing	: 6.2 id, width = .5 Adjustable in XY plane
10	Strobe Light	
11	Shaft	: 0.5 od span = 30.

ALL DIMENSIONS IN INCHES

FIGURE 6: SET UP FOR THE PLANAR MODEL

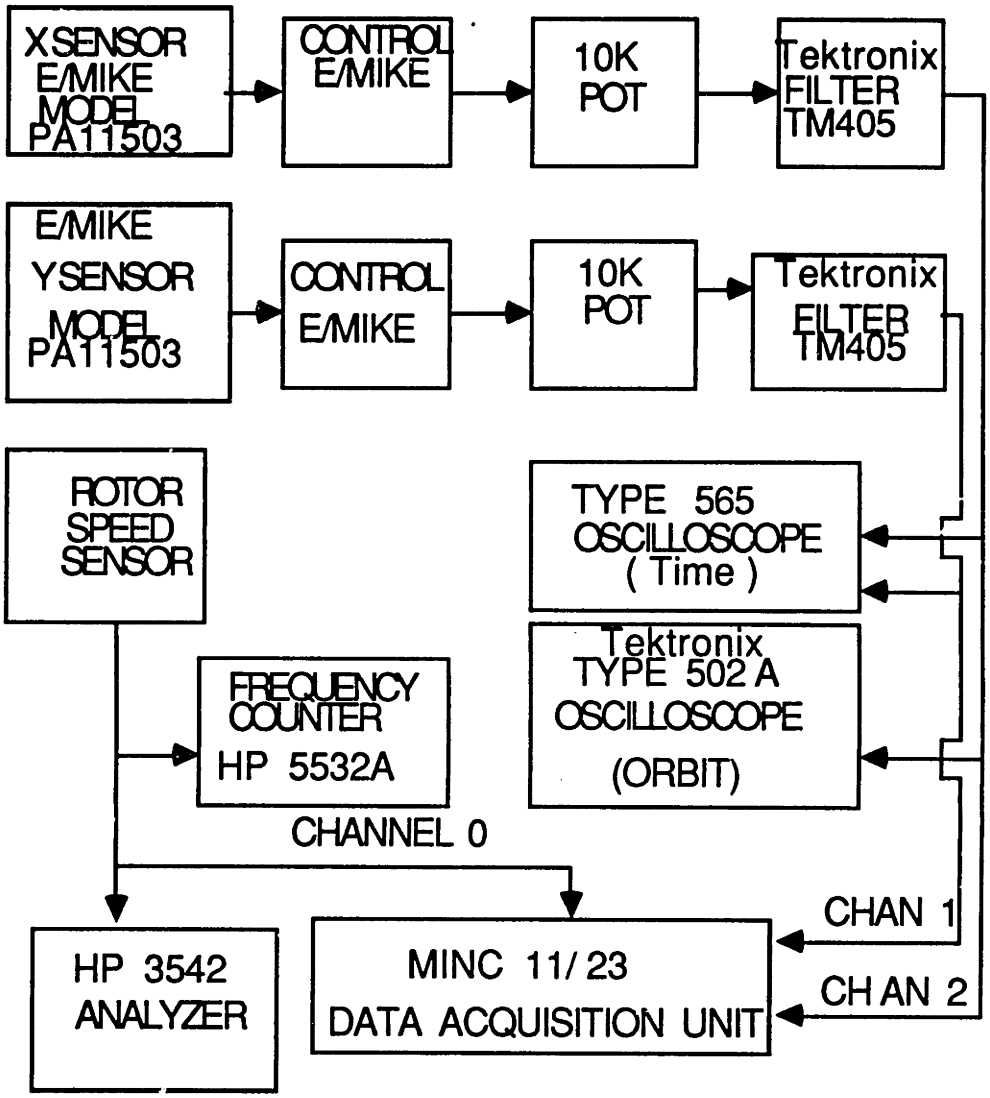

FIGURE 7: INSTRUMENTATION

4.4 Test Procedure

Two types of tests were performed. Initially, a vibrational analysis of the system was carried out to evaluate the characteristics of the system. This was followed by the tests involving rotor dynamics.

Following the preliminary tests the coefficient of friction between lexan and aluminum was measured, and the probes were calibrated (in situ). The gap between the probe and the steel disc was 0.125 inches. For the rotor dynamic tests the rotor speed was increased in discrete steps to reach beyond the first natural frequency, and then reduced in steps through the critical speed to zero speed. For each of the speeds two sets of data was acquired. First 210 points were taken at a sampling frequency of 500 Hertz to be used in x-y plots. Then 4096 points were taken at a sampling frequency of 200 Hertz for use in spectral analysis. Details of the test matrix are tabulated in Appendix B.

4.5 Data Reduction

All the calibrations were done on a Digital Equipment Corporation Minc 11/23 computer with a program named ECALIB. This program takes the input file named AXXX.DAT and the calibration constants and puts out the calibrated displacements in a file named AXXX.CLB. (The XXX are user designated numbers for the test.)

All the data was processed on a PDP 11/34 system. The raw data acquired by the MINC 11/23 is stored on floppy discs. This data was read on the PDP 11/34 with the help of a program named PROG1.FOR. This program takes the name of the raw data file (AXXX.DAT) and the

calibration constant and puts out the output from the three channels into files BXXX.C0, BXXX.C1, BXXX.C2, which correspond to the speed, X and Y measurements respectively.

The time series in files BXXX.C0 is processed by carrying out a spectral analysis using FFT by a program named PROG3.FOR.

The data from BXXX.C1 and BXXX.C2 (sampled at 500 Hz) is processed by a program called PROG2N.FOR. This program plots the orbit (X versus Y). The data sampled at 200 Hz (in the files BXXX.C1 and BXXX.C2) was processed by a program PROG3N.FOR. This program carries out a 1024 point FFT on the time series. For each of the spectral estimates 4 averages were taken. The resolution of the spectral estimate is 0.2 Hertz. It is possible to process up to ten time series (one after the other) and obtain a cascade plot of their spectra. The computed spectrum is put out in a file called BXXX.SPC.

Program RES.FOR computes the response of the rotor according to the full annular rub model. The experimental response is computed by taking the root means square value of a band of width 1 Hz centered at the peak response. This is done using the program PEAK.FOR.

CHAPTER 5: RESULTS AND DISCUSSION OF PLANAR MODEL TEST

5.1 General Description

Plots of X versus Y displacement represent the orbit traced by the center point of the rotor in the time domain. These plots are presented in Appendix E. The box made up by the axes of the plot represents the (fixed) frame of reference. Thus these plots indicate the nature of the motion of center point as seen with the help of a strobe light (sampling at 500 Hz). For the full annular rub the orbits overlap (roughly) in each successive cycle, such that their diameter is equal to twice the clearance between the shaft and the casing. In the case of partial rub, the orbit usually shifts forward or backward after each cycle. In the case of pure whirl (without rub) these orbits overlap but their diameter is smaller than twice the clearance. The speed indicated on these plots is the speed of the rotor drive (ω in Hz). Typically three cycles have been plotted in each case. The arrow on the orbit indicates the direction of whirl (clockwise for forward whirl). The arrow outside the plot indicates the direction in which the orbit shifts.

Spectra of the X displacement and Y displacement time series are estimated using an FFT algorithm. The speed on thess plots identifies the drive rotational velocity (ω in Hz). From these plots conclusions about the frequency content of the vibrational response are drawn. The resolution of these estimates is 0.2 Hz. Averaging has been done on these estimates to arrive at smooth results.

In the next two sections inferences from these plots are drawn. Based on these inferences the validity of the full annular rub model and the partial rub phenomena are discussed. Finally, a critique of

the investigation is presented along with some recommendations for future research work.

5.2 The Planar Model Test

The vibrational response of the rotor is considered first. Figure C3 shows that the first two natural frequencies of the shaft are 16.5 Hz and 113 Hz respectively in the horizontal direction. Figure C4 shows that the first two natural frequencies in the vertical direction are 16.5 Hz and 113 Hz. The theoretical value of the natural frequency (from section 4.2) is 15 Hz. The modal damping value in the first mode is computed as

$$\zeta_1 = \frac{\Delta\omega}{2\omega_1} = 0.01$$

The clearance is $r_c = 0.1$ inches.

The eccentricity (δ) is of the order of 0.01 inches. The coefficient of friction is 0.3 . Therefore

$$\varepsilon = \frac{\delta}{r_c} = 0.1$$

From equation (6)

$$\beta_{rub} = \frac{(2\zeta^2-1) + [(2\zeta^2-1)^2 + (\varepsilon^2-1)]^{1/2}}{\varepsilon^2-1} \simeq 0.91$$

This means that the rub ought to initiate at (0.91 x 16.5) = 15 Hz.

The nature of the response is dictated by the following parameters (refer to section 3.3).

$$2\zeta = 0.02$$

$$\mu/(1+\mu^2)^{1/2} = 0.287$$

$$(\zeta^2+\mu^2)/\mu(1+\mu^2)^{1/2} = 0.2876$$

In this case $2\zeta < \varepsilon < \frac{\mu}{(1+\mu^2)^{1/2}}$. Hence the mode of the motion is

LIMITED SYNCHRONOUS RUB (see Figure 4(a).

The speed required for initiating backward whirl (refer to section 3.4), assuming no slip is:

$$\beta_{reverse} \simeq \left(\zeta + \frac{(\zeta^2+\mu^2)^{1/2}}{\mu}\right) \simeq 1.033$$

so speed for the initiation of rub is, ω = 17 Hz.
Therefore (for motions without slip) reverse whirl is possible at speeds greater than 17 Hz, assuming (of course) that the rotor stays in full rub beyond this speed.

The results of the rotor dynamic tests are summarized in Table 4. Spectra of response (one from each typical condition) are given in Figures 8 through 13. These results are discussed here:

1. It is seen that for drive speeds below 14 Hz the rotor whirls without rubbing.

2. While increasing the speed, partial rub sets in between 14.0-15.0 Hertz. Full annular rub occurs between 15.0 and 17.5 Hertz. Partial rub occurs between 18.0 and 24 Hertz. A closer look at column 6 shows that the major component of vibration response does increase in magnitude until the full rub is reached, stabilizes during the limited full synchronous rub region, and then tapers off.

3. While decreasing the speed, full synchronous rub occurs only in the vicinity of 15.5 Hz. Partial rub is noticed between 24.5 to 16.0 Hz and 15.0 to 14.4 Hertz.

The following inferences can be drawn:

1. The nature of the motion is indeed LIMITED SYNCHRONOUS RUB as predicted earlier.

2. The response for increasing and decreasing speeds is not identical. This validates the theoretical prediction (see section

TABLE 4: Results of Planar Rub Experiment

(1)	Test Number (2)	Drive Speed Hz (3)	Spectrum				Orbital Plot		
				Major Peak		Minor Peaks			
			Figure (4)	Frequency in Hz (5)	Magnitude in inches (6)	Frequency in Hz (7)	Figure Number (8)	Nature of Orbit (9)	Shift in the Orbit Direction (10)
	700	14.1	-	13.3	0.0287	15.2, 17.2	E1	Minimal Rub	-
	701	14.5	-	15.2	0.0751	13.2, 17.2	E2	Minimal Rub	-
	702	14.8	7	15.2	0.0757	13.2, 17.2	E3	Minimal Rub	-
	703	15.6	-	15.2	0.1011	-	E4	Full	-
	704	15.95	-	15.2	0.0876	17.2	E5	Full with wobble	Wobble
	705	16.5	-	17.2	0.0892	15.2	E6	Full	-
	706	16.9	-	17.2	0.121	-	E7	Full	-
	708	17.5	8	17.2	0.121	-	E8	Full	-
	707	18.0	-	15.2	0.0669	13.2, 17.2	E9	Part	Backward
	709	18.6	-	15.2	0.068	13.2, 17.2	E10	Part	Backward
	710	19.0	-	15.2	0.0689	13.2, 17.2, 19.2	E11	Part	Forward
	711	20.0	9	15.2	0.0714	13.2, 17.2, 19.2, 21	E12	Part	Backward
	712	24.4	-	15.2	0.0601	11.2, 13.2, 17.2, 19.2, 21, 24	E13	Part	Minimal
	713	20.4	-	15.2	0.0601	11.2, 13.2, 17.2, 19.2, 21, 24	E14	Part Rub (Limited)	Forward
	714	19.1	10	17.2	0.0622	15.2, 19.2, 21	E15	Part Rub (Limited)	Backward
	715	18.6	-	17.2	0.0636	13.2, 17.2, 19.2, 21	E16	Part	Backward
	716	17.8	-	15.2	0.06032	13.2, 17.2, 19.2	E17	Part	Backward
	717	17.5	-	15.2	0.06506	13.2, 17.2, 19.2	E18	Part	Backward
	718	17.1	-	15.2	0.059134	13.2, 17.2	E19	Part	Minimal
	719	15.5	11	15.2	0.0905	-	E20	Full	
	720	14.8	-	15.2	0.0729	13.2, 17.2	E21	Part	Minimal
	721	14.4	12	15.2	0.054	11.2, 13.2, 17.2, 19.2	E22	Part	Minimal
	722	13.5	-	13.2	0.02	15.2, 17.2	E23	No Rub	-

Test # 702
Planar Model (Speeding up)
Drive Shaft speed 14.5 Hz
Sampled at 200 Hz, 1024 point FFT
4 Averages, Resolution 0.195 Hz

Minimal Rub

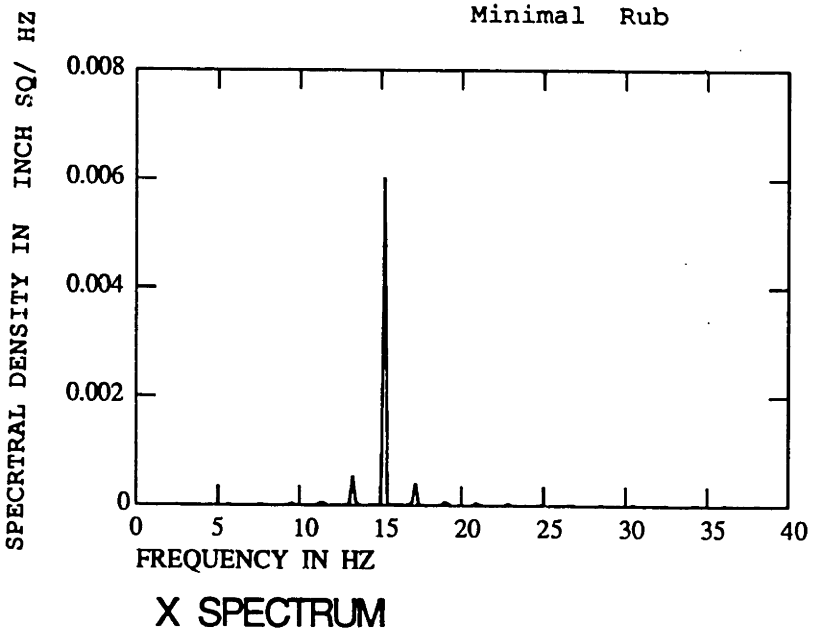

X SPECTRUM

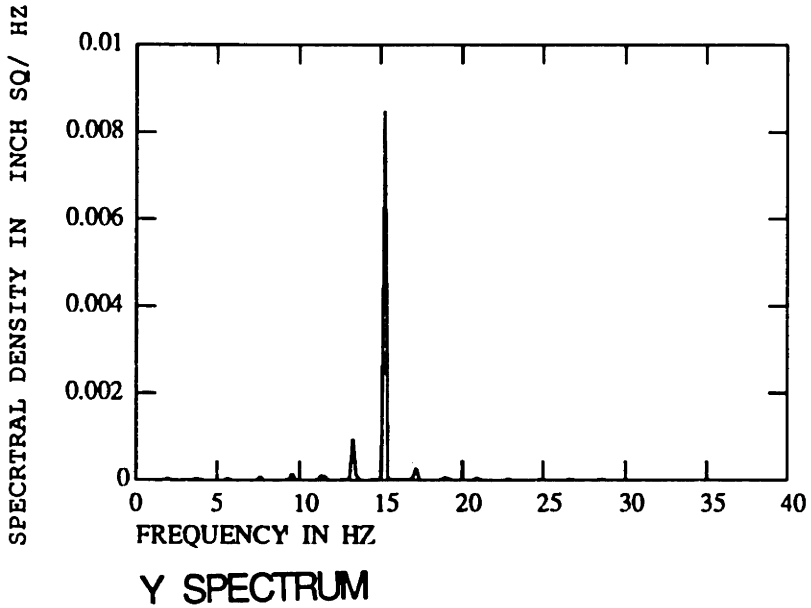

Y SPECTRUM

FIGURE 8

Test # 708
Planar Model (Speeding up)
Drive Shaft speed 17.5 Hz
Sampled at 200 Hz, 1024 point FFT
4 Averages, Resolution 0.195 Hz

Full Annular Rub

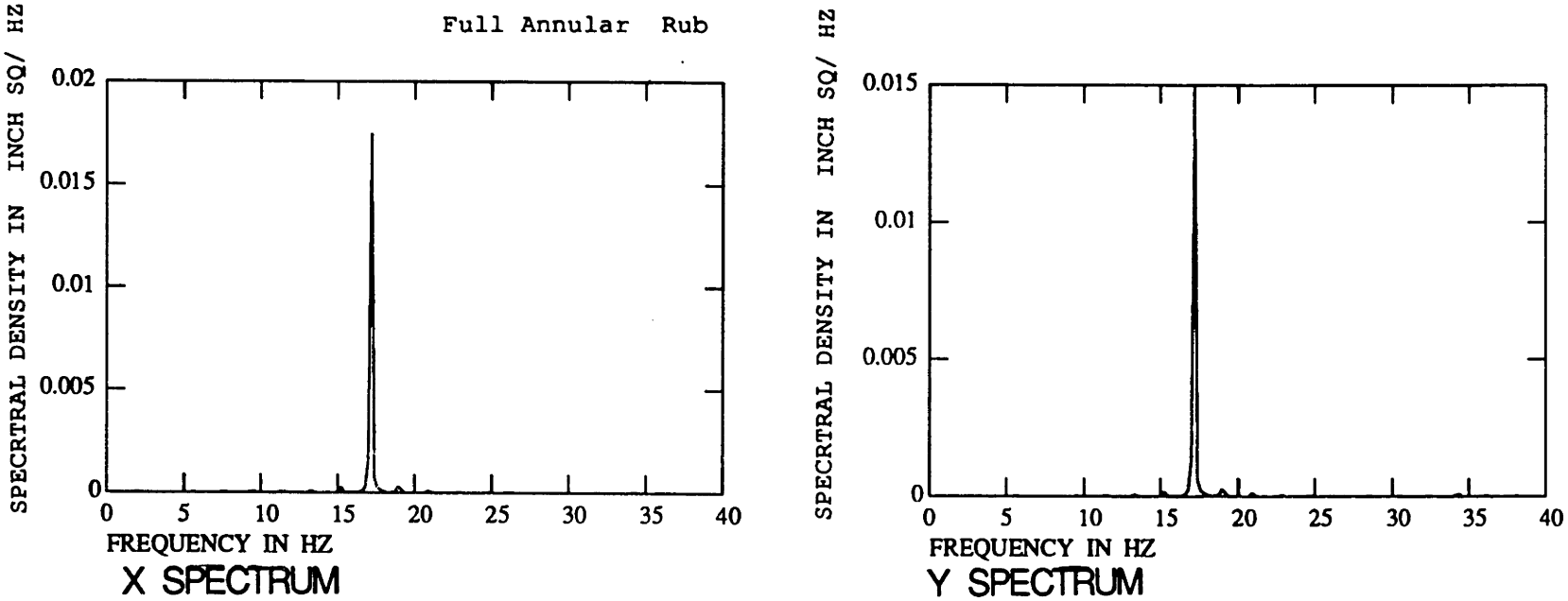

FIGURE : 9

Test # 711
Planar Model (Speeding up)
Drive Shaft speed 20.0 Hz
Sampled at 200 Hz, 1024 point FFT
4 Averages, Resolution 0.195 Hz

Partial Rub

SPECRTRAL DENSITY IN INCH SQ/ HZ

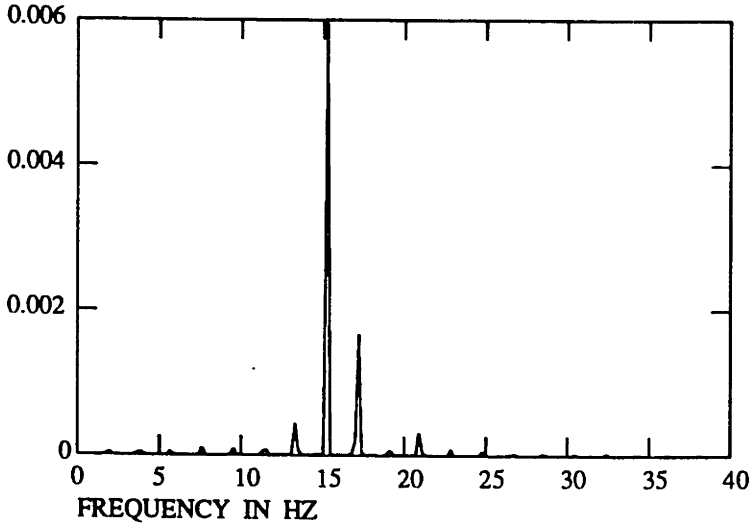

X SPECTRUM

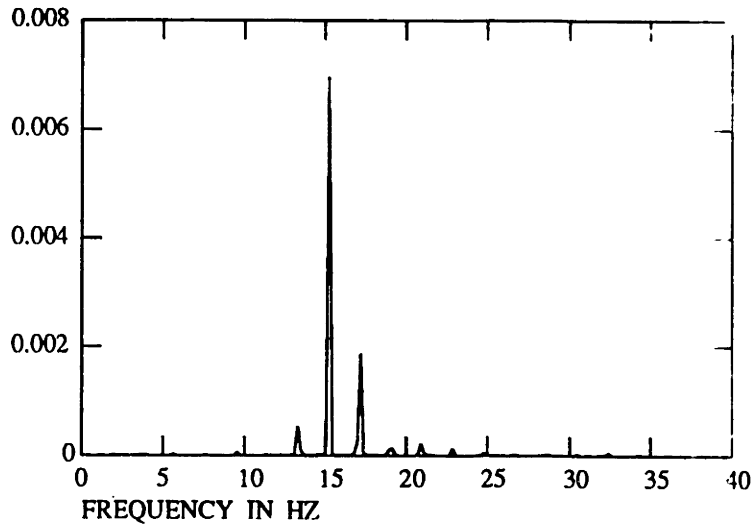

Y SPECTRUM

FIGURE : 10

Test # 714
Planar Model (Slowing Down)
Drive Shaft speed 19.1 Hz
Sampled at 200 Hz, 1024 point FFT
4 Averages, Resolution 0.195 Hz

Partial Rub

SPECRTRAL DENSITY IN INCH SQ/ HZ

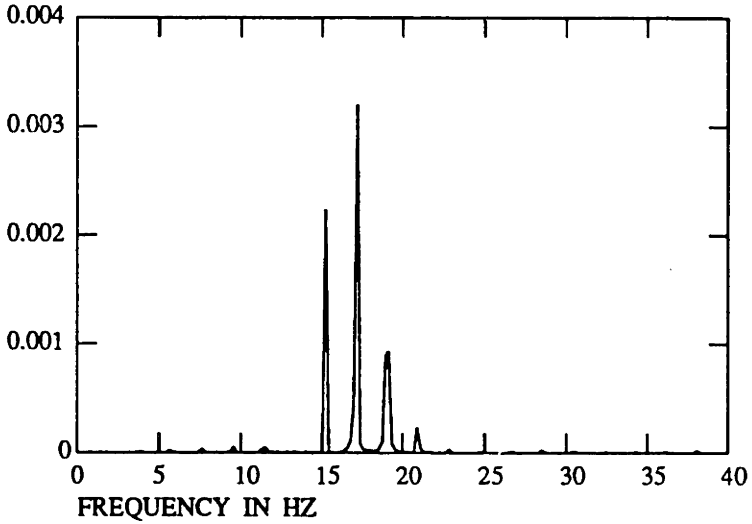

X SPECTRUM

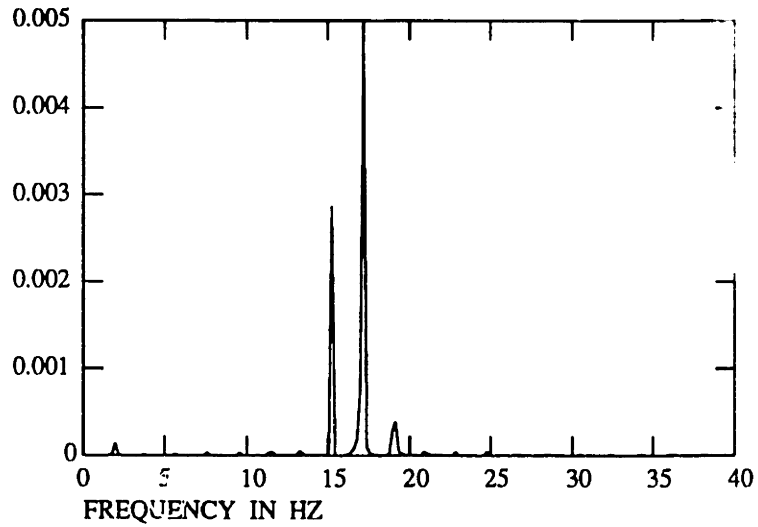

Y SPECTRUM

FIGURE : 11

Test # 719
Planar Model (Slowing Down)
Drive Shaft speed 17.5 Hz
Sampled at 200 Hz, 1024 point FFT
4 Averages, Resolution 0.195 Hz

Full Annular Rub

SPECRTRAL DENSITY IN INCH SQ/ HZ

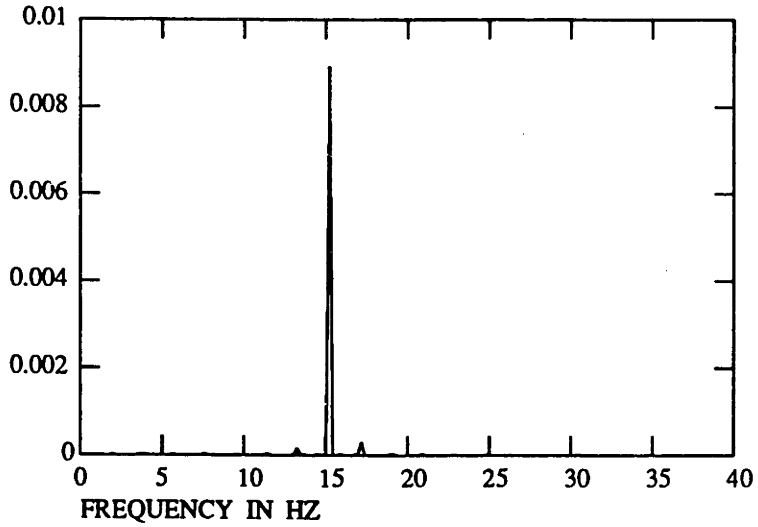

X SPECTRUM

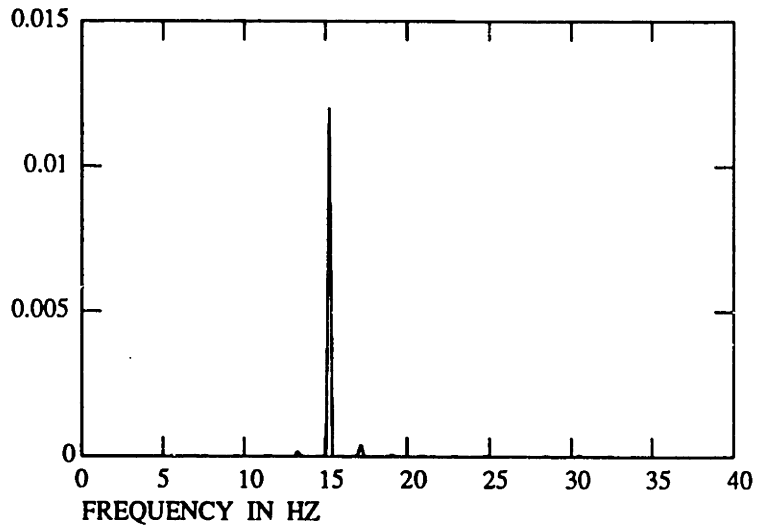

Y SPECTRUM

FIGURE : 12

Test # 721
Planar Model (Slowing Down)
Drive Shaft speed 14.4 Hz
Sampled at 200 Hz, 1024 point FFT
4 Averages, Resolution 0.195 Hz

Partial Rub

SPECRTRAL DENSITY IN INCH SQ/ HZ

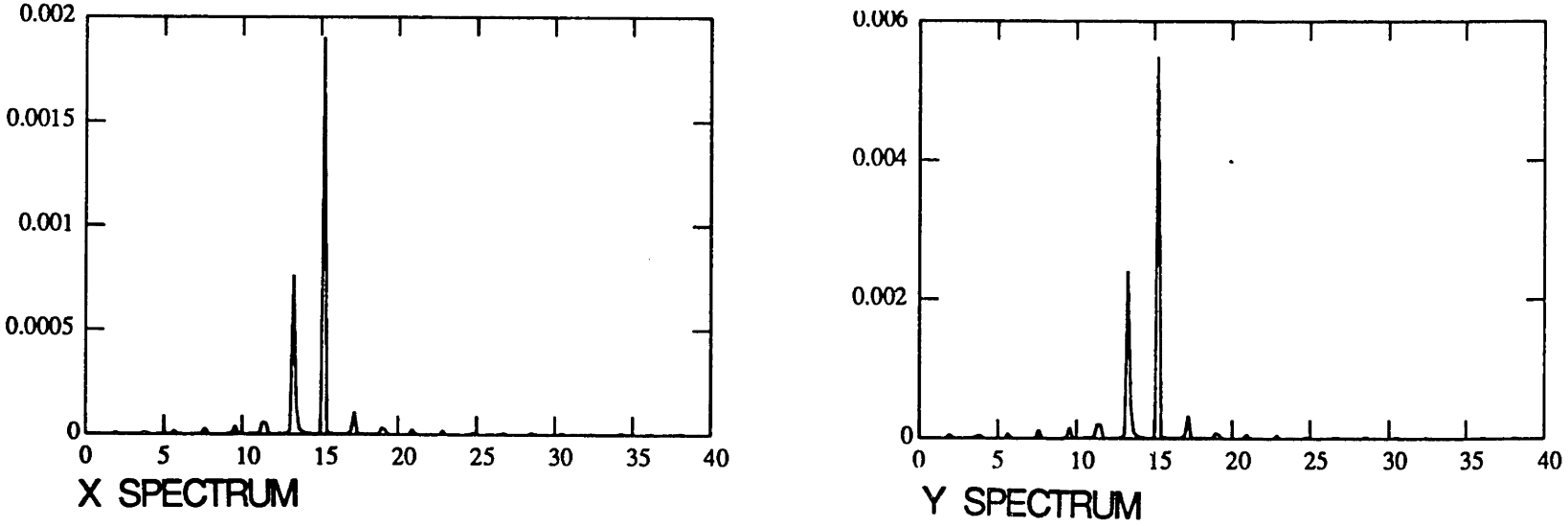

FIGURE : 13

4.3).

3. The predicted value of ω_{rub}(15 Hz) is well within the acceptable experimental accuracy.

4. Contrary to the theoretical prediction, backward whirl does not take place. This can be explained by the fact that the full synchronous rub does not sustain itself beyond 17.5 Hz. In fact a closer look at column 6 around 17.5 Hz shows that the displacement is maximum. As discussed in section 3.3 (limited synchronous rub), any further increase in speed increases the normal force and the larger frictional force causes a decrease in the whirl amplitude and a loss of contact.

Spectra for typical conditions are presented in Figures 8 through 13. The resolution of these estimates is 0.195 Hz. In each of these plots the X and Y displacement time series spectra are shown separately. Figure 8 shows spectrum at drive speed of 14.5 Hz while speeding up. The orbital plots confirm that there is a minimal amount of (partial) rub. Most of the energy is concentrated at 15.2 Hz, with some side bands at 11.2, 13.2, 17.2, and 19.2 Hz. This type of behavior is noticed in all the partial rub spectra (Figures 8, 10, 11, 13).

Figure 10 shows the partial rub spectrum at a drive shift speed of 20 Hz while speeding up after the rotor has passed through the full annular rub range. Figure 11 shows the spectra for partial rub while the rotor is running at 19.1 Hz while slowing down (but above the critical speed of 16.5 Hz).

Figure 9 shows the spectra in the full annular rub condition at drive speed of 17.5 Hz while speeding up. There is only one major

component in these spectra (at 17.2 Hz). Figure 12 shows the full annular rub spectra at the drive speed of 15.5 Hz (while slowing down). Again, the full annular rub has only one major peak (at 15.2 Hz). The inference drawn from these plots is that the rotor has a tendency to run at a number of preferred speeds during the partial rubbing. For this particular case these speeds are 11.2, 13.2, 15.2, 17.2, 19.2, and 21.2 Hz. As soon as the rotor starts rubbing (partially), most of the vibrational energy is located in some of these frequencies (usually in a band closest to the drive speed). The full annular rub ought to be viewed as an extreme case of partial rub, such that almost all the energy is at particular frequency. It is also noticed that regardless of the type of rub (full or partial), the peak response frequency (whirl frequency) is not necessarily the same as the drive frequency. This means that the rubbing is accompanied by slip. It is also noticed that during the full annular rub the peak (that is the whirl speed) was at 15.2 (Ω) Hz for the drive speed of 15-15.5, but on further increase in the drive speed (16-17.5 Hz) the full annular rub shows the whirl at 17.2 Hz. It is concluded that the rotor changes its preferred orbital speed (and the amount of slip).

The theoretical values of (frequency) response of the rotor for various driving speeds is presented in Figure 14. The first part shows the response while speeding up, the second part shows the response while slowing down. In each case the theoretical values of free (unconstrained) as well as full annular rub response are plotted. Finally, the measured value of the peak is plotted too. (This peak value was computed by estimating the r.m.s. value of the peak, for a band width of 1 Hz, and raising it appropriately.)

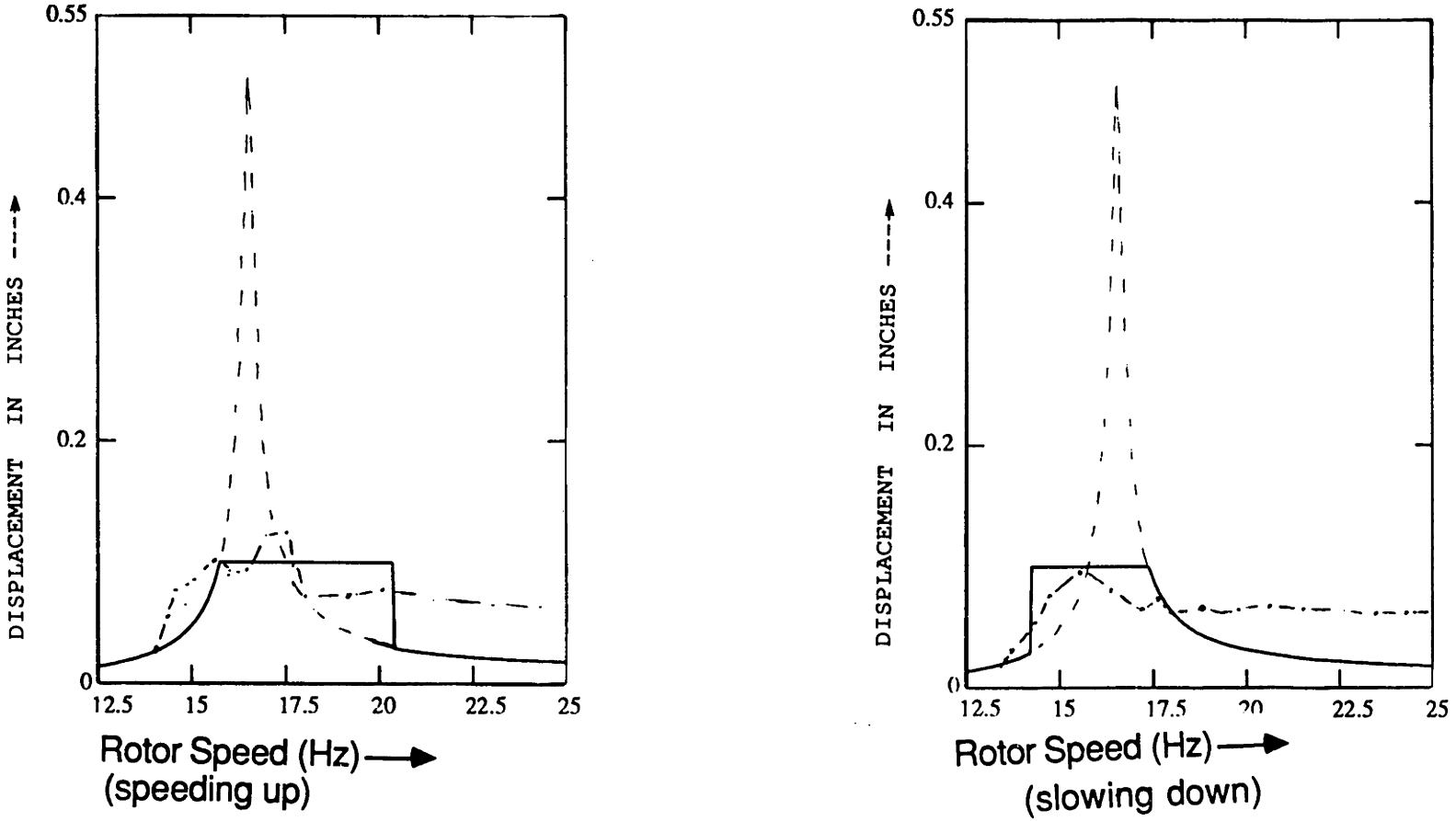

FOR μ = 0.3
ϵ = 0.01
δ = 0.10
ζ = 0.01

UNCONSTRAINED (THEORY) - - - - - -
FULL ANNULAR RUB (THEORY) ————————
MEASURED RUB -.-.-.-.-.-.-.-

FIGURE 14: RESPONSE OF PLANAR MODEL

A few comments are offered on these results:

1. One basic assumption of Stackley's theoretical model is that the rotor response switches directly from free whirling into a full synchronous rub. Based on this study it is concluded that real systems go through a transitional region of partial rubbing. The nature of partial rubbing is in agreement with the type behavior suggested by Muszynska (see Appendix A for details). The partial rub response is characterized by a spectrum that is broad band. Most of the energy of the vibration is centered at the natural frequency (regardless of the speed of the rotor drive). There are usually two side bands located symmetrically about the major component. There is very little energy at the drive speed.

2. One of the more complicated issues involved in the understanding of the rub phenomenon is the role of dry friction. It has been implicitly assumed in the discussions to far that the coefficient of friction is constant. The value of the coefficient of friction measured by the classical sliding experiment (one material is slid over the other and the force required to slide is measured) is not strictly applicable to the rotational situation. Rabinowicz (1965) states that sliding of one body over another proceeds on occasions at velocities that vary widely. This situation is termed as stick slip. All stick-slip processes are caused by the fact that the friction force does not remain constant but is oscillatory. It was observed repeatedly during the visual study of the rotor rub that at times the rotational motion was oscillatory. (The visual evidence can be established from the fact that if the strobe light is locked at the frequency of the synchronous rub, often the rotor moved ahead and

behind.) The exact reason for the occurrences are not known, but a number of factors could influence this behavior. These factors include fluctuation in the motor load, wear, temperature, etc. It is then possible for a rotor in midst of a stable (theoretically) full synchronous rub to show fluctuations. This kind of behavior is seen in the orbital plot E5.

3. Figure 14 shows some discrepancy between the measured and theoretical values of the response. The following comments are offered by the way of possible sources of inconsistency.

a. The effect of gravity has been ignored in the theoreetical model under the assumption that the rotational acceleration is much larger than the gravitational acceleration. In reality this is not always true. Gravity causes the shaft to bow under its own weight.

b. The shaft is assumed to be straight and perfectly aligned. The experimental model must have been out of alignment to a certain extent.

c. The abscissa of Figure 14 is the rotor speed in Hertz. This was measured with an HP5532A frequency counter that has a least count time of 0.1 seconds. The circuit averages 100 measurements. There was some fluctuation ($\pm$ .5 Hz, maximum) in the rotor speed while the data was being acquired. This non-stationary input would cause variation in the assumed steady state dynamic response.

d. The inputs to the theoretical model are the parameters μ (co-efficient of friction), ε (the eccentricity ratio), and ζ (the modal damping).

An attempt is made here to study the effect of errors in the

estimation of μ, ε and ζ on the final results. It is speculated that the estimates of the coefficient of friction could vary widely (0.3 $\pm$ 50%). The damping ratio (0.01) could be between (0.0075 and 0.0125) and the eccentricity could vary between (0.0075 and 0.0125 inches). Figure 15 shows the theoretical estimate of the radial response for three different values (0.0075, 0.01, 0.0125) of the damping ratio. It is seen that the variation in the damping ratio does not affect the result at all. Figure 16 shows the effect of eccentricity on the estimate for the increasing speed lose. It is seen that the low speed of initiation of full annular rub (ω_{rub}) is slightly affected by the variation in the eccentricity. However the high speed termination of the full annular rub region varies considerably ($\pm$ 10%) with a ($\pm$25%) variation in eccentricity. Finally Figure 17 shows that the value of the coefficient of friction strongly affects the range of the full annular rub. It is therefore concluded that the variability between the theoretical and the experimental data in Figure 14 is, to a large measure, due to the error in the measurement of the coefficient of friction value.

An attempt was also made to vary the coefficient of friction by greasing the contact surface. However, a systematic study of this phenomenon was not carried out. In general it was seen that the occurrence of partial rub was suppressed by the introduction of the grease, and the region of rub was broadened. This finding is in agreement with the trend exhibited in Figure 17.

5.3 Critique

In this section a few of the issues regarding modelling and test

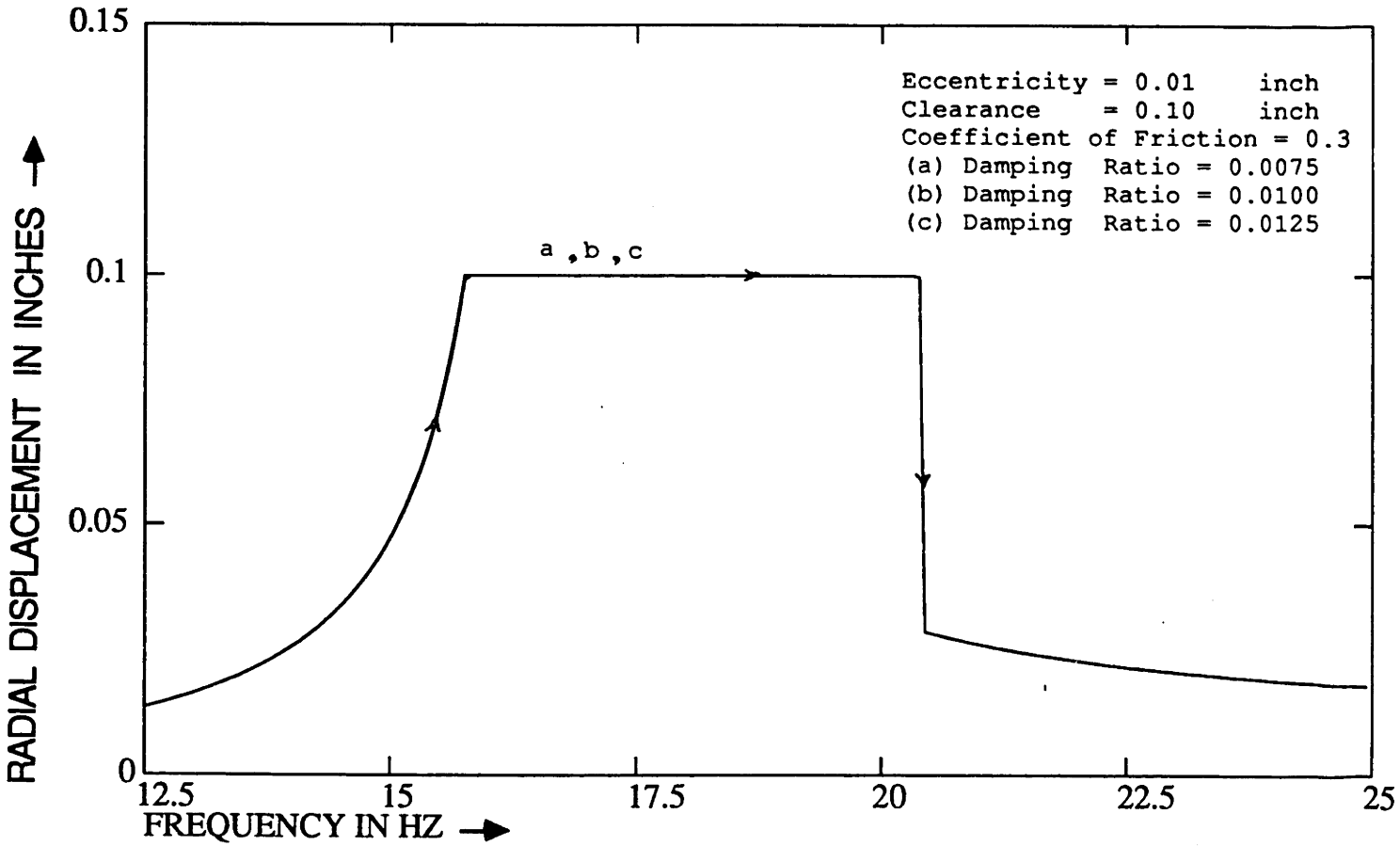

FIGURE : 15 EFFECT OF VARYING DAMPING

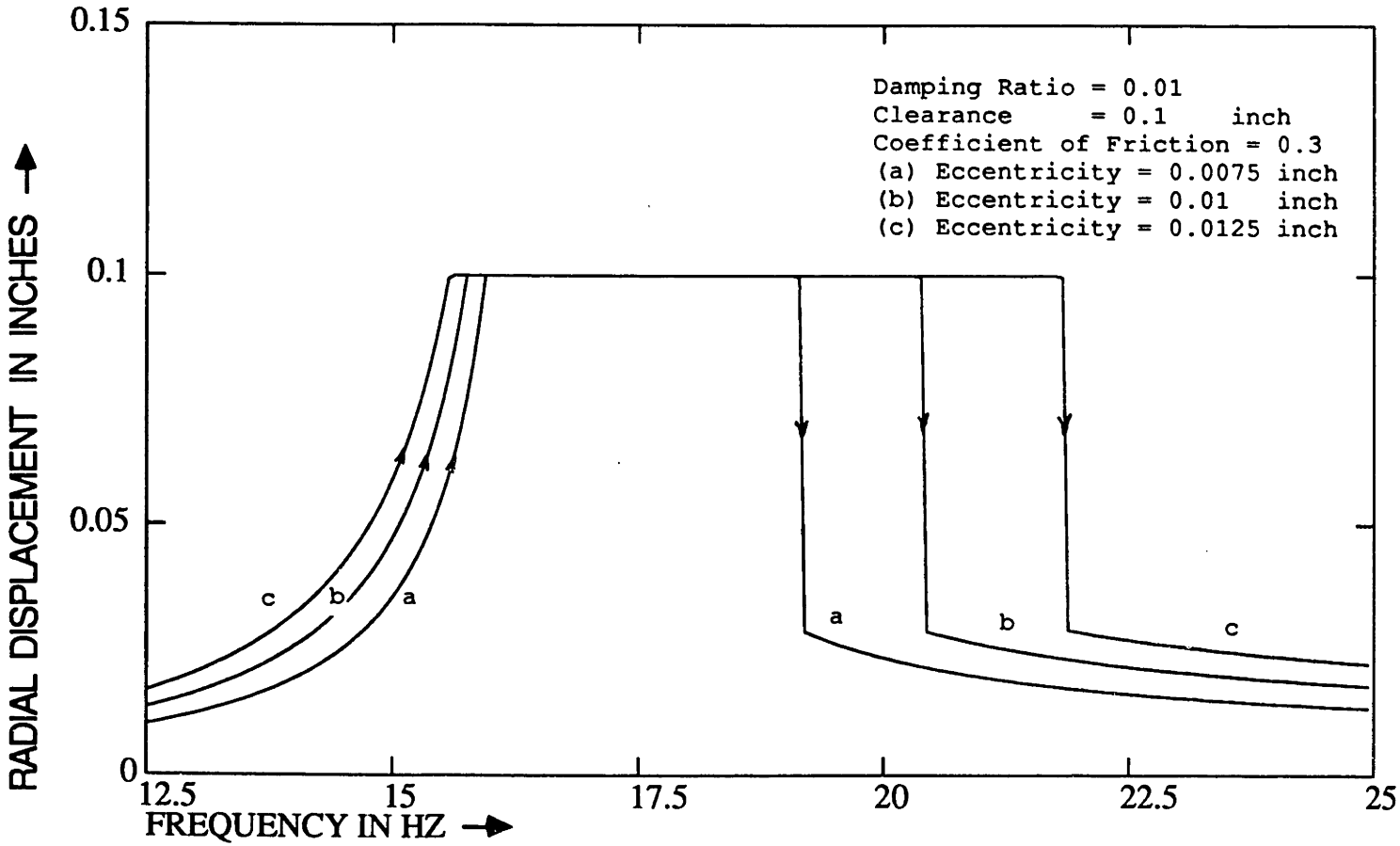

FIGURE : 16 EFFECT OF VARYING ECCENTRICITY

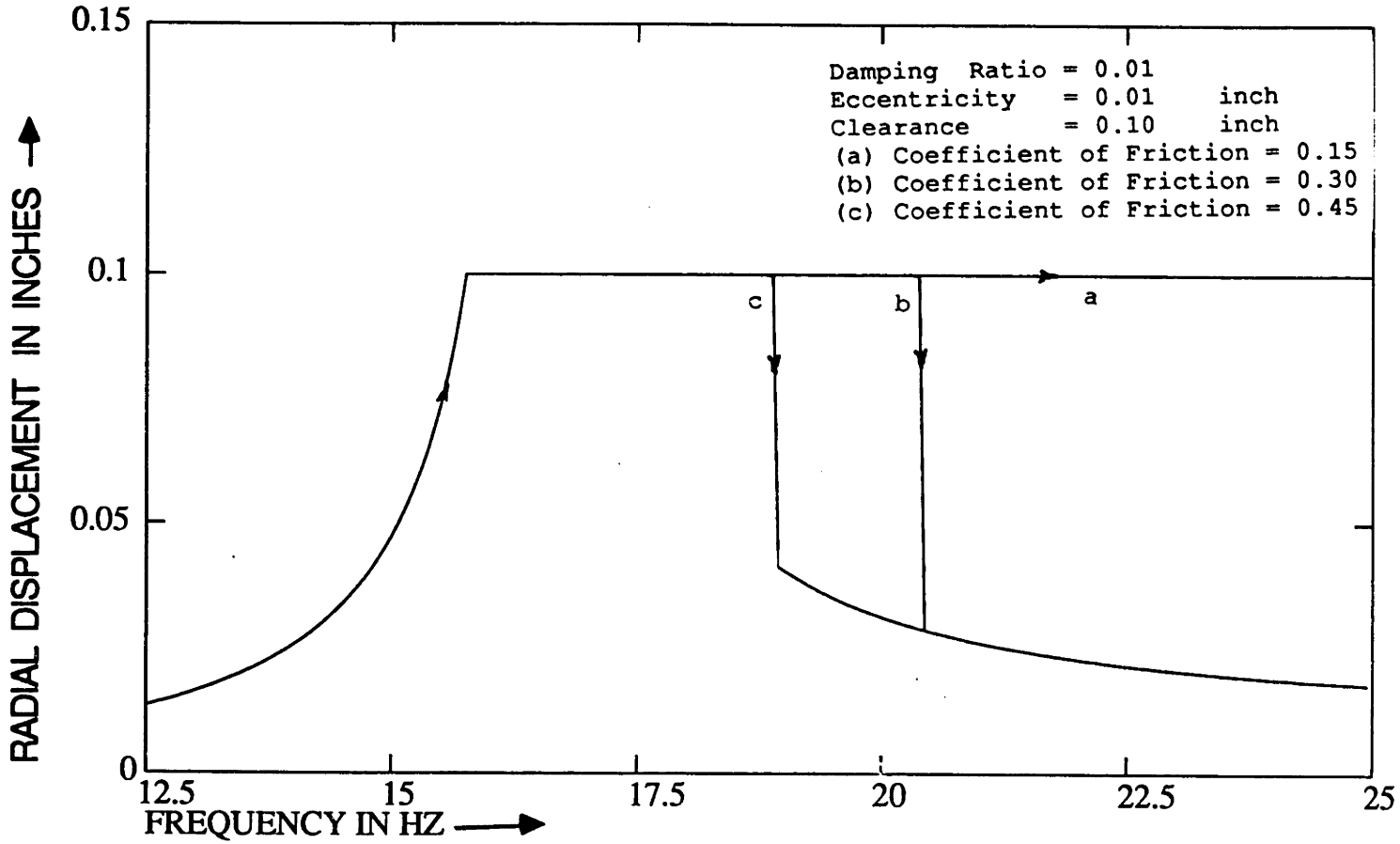

FIGURE : 17 EFFECT OF VARYING COEFFICIENT OF FRICTION

procedures are reviewed.

On the whole, the performance of the planar model has been deemed satisfactory. But three items need further discussion. These are the measurement of eccentricity and coefficient of friction, the performance of the probes, and wear of the rotor.

Each part of the rotor was originally balanced on a lathe. When the rotor was assembled it showed an eccentricity. The accuracy of the balancing process was clearly not very high. The value of the coefficient of friction has a considerable variability. Both these parameters figure prominently in the model proposed by Stackley. They must be estimated as accurately as possible.

The performance of the probes was not really linear. This has affected the accuracy of the measurement. The range of the probes has been a major limiting factor in the design of the experiment. Perhaps a set of probes with a larger range would have provided more flexibility in the design choices.

The wear of the model has not figured in any discussion so far. But inevitably, as the tests progress, the lexan disc wears. This would change the surface conditions as well as modify the configuration at the point of contact.

The orbital plots for full annular rub seem to be oval in shape. Perhaps the last two items discussed here could account for this discrepancy.

5.4 Recommendations

It will be appropriate to change the probes and use a system that is linear and has a wider range.

In terms of experiments, it would be interesting to study the performance of the planar model with a much higher coefficient of friction. This could lead to simulation of backward whirl. The drawback of this test is that it might destruct the system.

CHAPTER 6: RADIAL RUBBING OF A DRILL COLLAR

6.1 Unbalanced Response of the Drill String

Figure 18 shows the configuration of the drill collar model. The drill string lies along the longitudinal axis S between two simple supports (stabilizers). The shaft is hollow and conveys fluid inside. The annular space allows the external flow.

In the following analysis a number of assumptions have been made. The string is assumed to be flexible with one end free to move along the S direction. It has a uniform cross section made up of homogeneous material, and is subjected to uniform axial stress. The bending behavior of the shaft is modelled as the so-called "Euler Bernoulli" beam. The hole is vertical and the effects of gravity are neglected. The fluid is assumed to be incompressible. All flow is steady state. Circulation losses are neglected. The effect of axial frictional forces on this fluid cancels out with that of the pressure gradient. The equation of motion for the lateral vibration of the rotating drill string is given by:

$$\underset{(1)}{EI\frac{\partial^4 Z}{\partial S^4}} + \underset{(2)}{\{m-\rho(A_e-A_i)+m_H\}\frac{\partial^2 Z}{\partial t^2}} + \underset{(3)}{(P-\rho(A_eU_e^2-A_iU_i^2))\frac{\partial^2 Z}{\partial S^2}}$$
$$+ \underset{(4)}{[m-\rho(A_e-A_i)]\,[-gS\frac{\partial^2 Z}{\partial S^2} - g\frac{\partial Z}{\partial S}]} + (dm+m_H b)\frac{\partial^2 Z}{\partial S^2}$$
$$- 2\rho(A_eU_e-A_iU_i)\frac{\partial^2 Z}{\partial S\partial t} + (m+\rho A_i)\,\delta\omega^2 e^{i\delta t} = 0 \qquad (10)$$

where

EI = bending stiffness

m = mass per unit length of the hollow cylinder

ρ = fluid density

A_e = outer sectional area of the cylinder

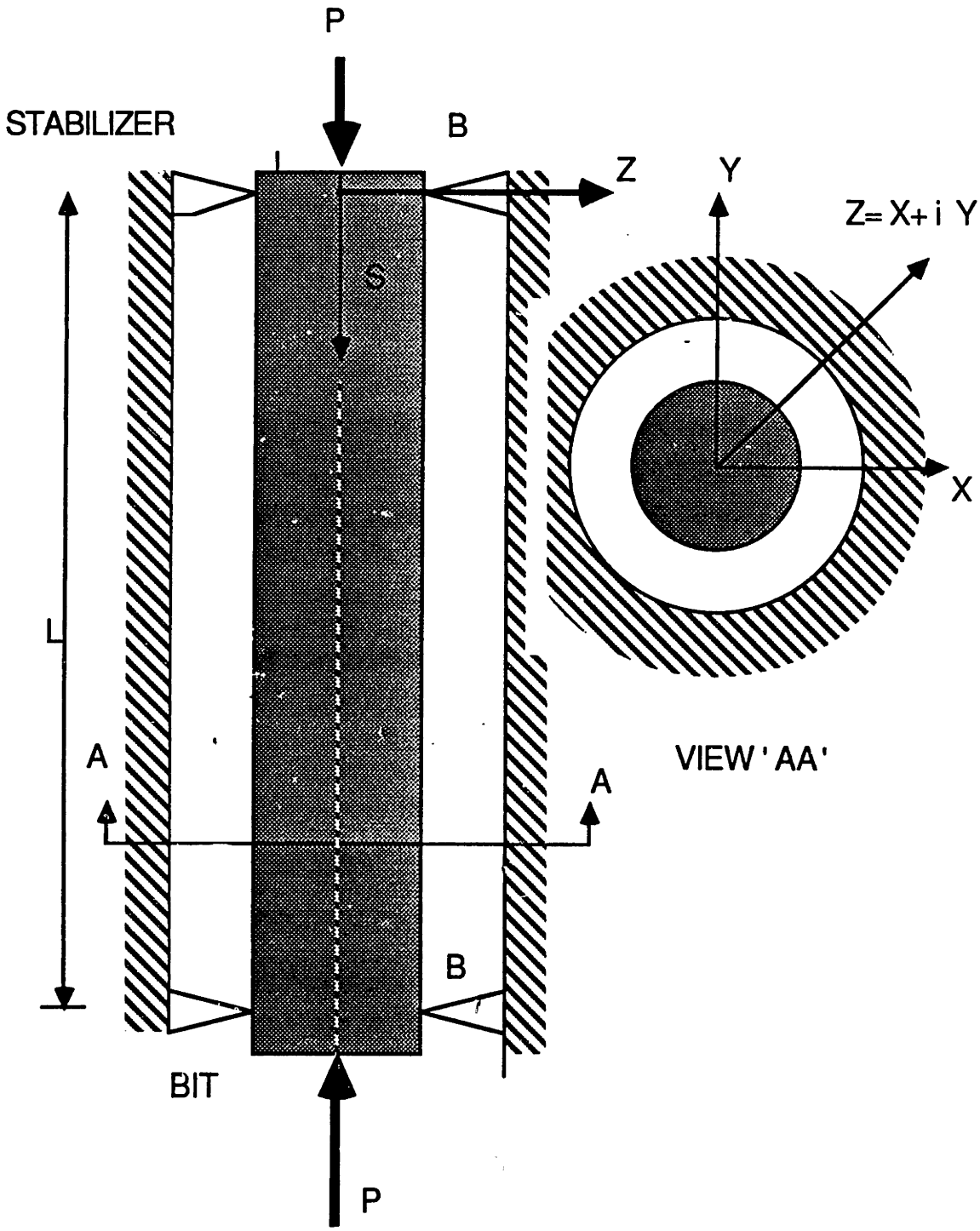

FIGURE 18: DRILL STRING MODEL

A_i = inner sectional area of the cylinder

m_H = hydrodynamic mass per unit length

P = axial compressive force

U_e = exterior axial flow velocity

U_i = interim axial flow velocity

d = structural damping parameter

b = hydrodynamic damping parameter in the annuli

δ = eccentricity due to unbalanced drill collar

The first and second terms in this equation are the bending stiffness and inertia terms, also accounting for the added mass and lift force effects. The third term represents the force required to change the direction of the fluid while the shaft is deformed. The fourth term is due to linearly varying gravity loads. This may be neglected for large axial compressive force P. The fifth term describes the energy loss due to structural and hydrodynamic damping. The sixth term is due to the Coriolis effect. Finally, the seventh term is due to the centrifugal force.

This equation does not lend itself to a closed form solution and is typically solved using a finite difference procedure. It has been shown by Belkheria that when L is on the order of 60 feet with a collar diameter of 7 inches, the predominant response for a typical drill collar is in the first mode. Therefore it is reasonable to study the system as an equivalent single degree of freedom model where the mode shape is that of a beam with pinned ends and is given by $(\sin \frac{\pi x}{L})$ The equation of motion reduces to

$$(\mu_1+m_H) \frac{L}{2} \ddot{q}_1 + Dq_1 + \frac{\pi^2}{2L} \left(P - \frac{EI\pi^2}{L^2}\right) = \frac{\mu_2 L \delta \omega^2 e^{i\omega t}}{\pi}$$

where

μ_1 = mass per unit length associated with gravity =

μ_2 = mass per unit length associated with the centrifugal form

D = damping constant (structural plus fluid damping)

P = axial load

EI = bending stiffness

L = span of the beam

δ = eccentricity

m_H = added mass coefficient

$q_1(t)$ = the modal response in first mode (and is the maximum mid span response)

A close look at this equation indicates that it is essentially of the same form as discussed in the Jeffcott Model. The distinguishing features are the hydrodynamic added mass (m_H) and damping (b), and the form of the elastic restoring force term. The hydrodynamic coefficients are discussed in the next section. Finally, the effect of rubbing on the elastic restoring force is discussed in the last section of this chapter.

6.2 Added Mass and Damping Coefficient

From a physical standpoint the added mass coefficient represents the amount of fluid accelerated due to the motion of the body. Strictly, the particles of the fluids adjacent to the body will accelerate to varying degrees, depending on their position as well as the type of body motion. The added mass then is a weighted integration of the entire mass of fluid. Similarly the damping

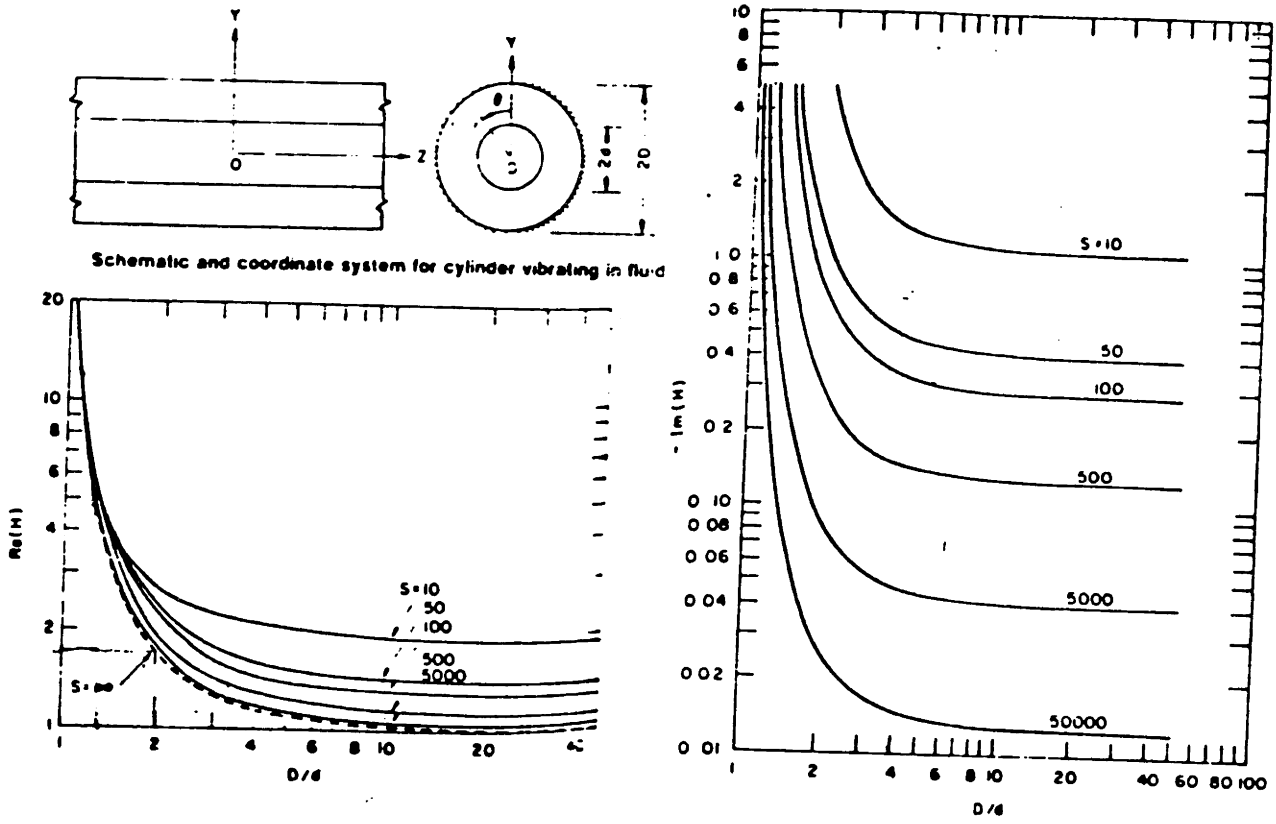

ADDED MASS COEFF = RE (H)

DAMPING COEFF = -m w IM (H)

d = Shaft Diameter
D = Casing Diameter
nu = Kinematic Viscocity
w = Frequency
m = Mass per unit Length of the Shaft
s = $w d^2 / nu$

FIGURE 19 ADDED MASS AND DAMPING COEFFICIENT

(From Chen et al , 1976)

coefficient gives a force proportional to the body velocity.

The effect of the fluid confinement on the hydrodynamic coefficients is very significant. In general the added mass coefficient for a rod in a confinement is much larger, as one would expect, than the added mass coefficient of the same body in an infinite fluid.

Chen et al (1976) have presented analytical as well as experimental data for cylinders vibrating in a fluid annulus. However, these cylinders are not whirling. This data may be used as reference for the estimation of the drill string added mass and damping coefficients. Figure 19 shows the plots of predicted added mass and damping coefficient against the clearance to diameter ratio for vibrating but not rotating confined cylinders.

6.3 Drill String Vibration With Rubbing

It has been pointed out in section 4.3 that the unconstrained motion of the drill string can be represented by a single degree of freedom model analogous to the Jeffcott Model from section 3.2. Extending this idea further, the rubbing of the drill string will show a behavior similar to the results expected according to the planar full annular rub model of section 3.3.

In the case of the drill string the system configuration with rub in mode 1 has been as visualized in Figure 20.

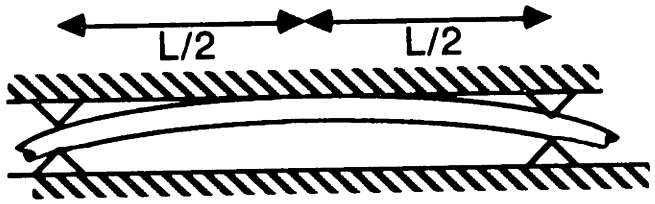

Figure 20: Rubbing of Drill String in Mode 1

Then in a manner analogous to equation (10) the modified elastic restoring force is computed as

$$K'q_1 = \frac{\pi^2}{2L}\left(P - 8\,\frac{EI\pi^2}{L^2}\right) \tag{11}$$

This result is introduced in a full annular rub model so that the system response is

$$q_1(t) = \left\{\frac{\mu_2 \frac{\delta\omega^2 L}{\pi} - 8EI\left(\frac{\pi}{L}\right)^2}{K^1 - M\omega^2 + j\omega D}\right\} \varepsilon^{i\omega t} \tag{12}$$

Figure 21 shows the response of an eccentric drill collar (such as the Woodpecker) with and without rubbing based on this formulation. For this example the input data is given in Appendix C. Two very characteristic features of this response are that

1. The stiffness modification causes the rubbing over a wider range of frequency than that predicted by the Jeffcott Model. This result is consistent with Stackley's findings.

2. The response for speeding up and slowing down can be different because in each case the modified stiffness does not come into play till the full annular rub is initiated. This happens at different rotation rates when increasing or decreasing speed.

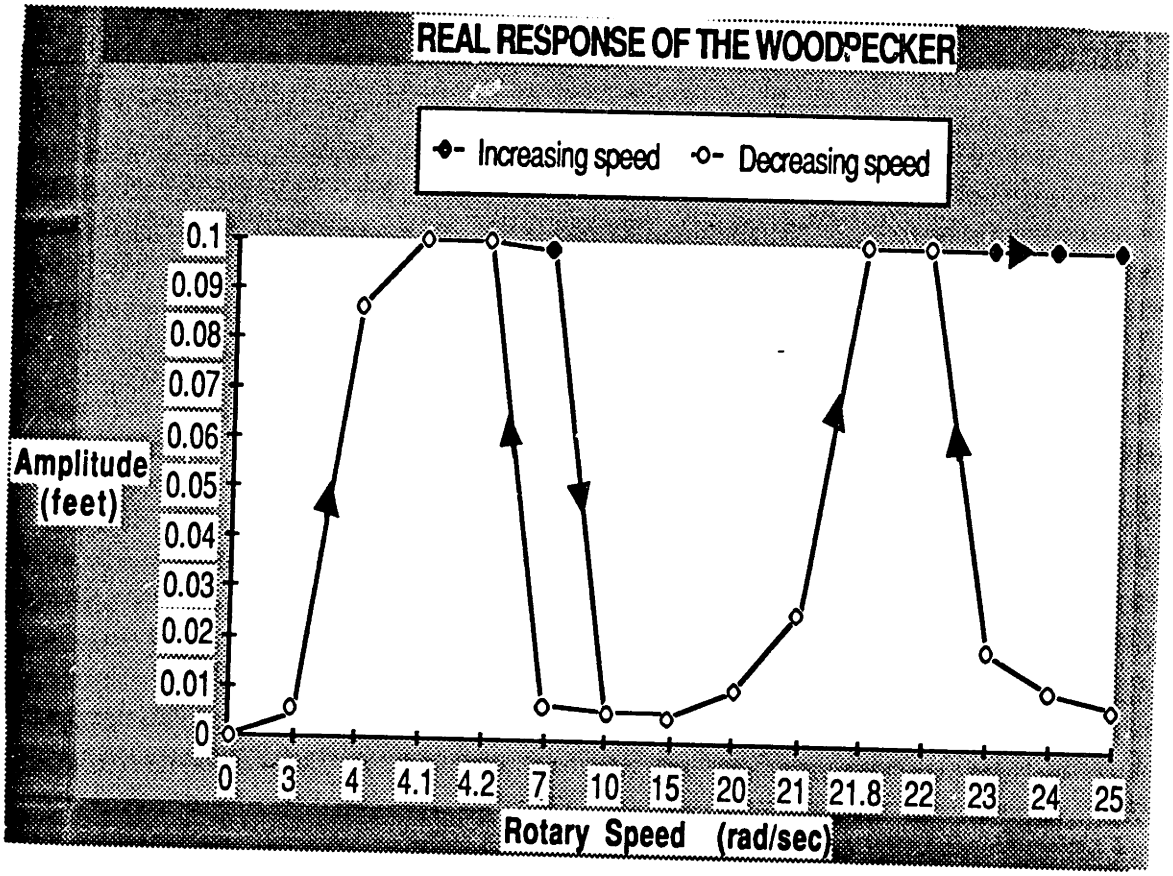

FIGURE : 21 TYPICAL RESPONSE OF A DRILL COLLAR
(From Belkheria, 1986)

CHAPTER 7: EXPERIMENTAL STUDY OF THE DRILL COLLAR MODEL

7.1 General Description

The objective of this set of tests has been identified as the modelling and testing of drill string vibrations in the presence of fluid in order to study the range of validity of the full synchronous rub model. One effect of the fluid present in the annular space is the so-called "Added Mass". The added mass can be computed from this test.

In this chapter the rationale behind the design of the model is discussed. Dimensionless parameters have been identified for the purpose of establishing similitude. These parameters offer a basis for modelling the drill string vibrations. A brief description of the model design and construction is presented. The test set up and instrumentation have been described. Finally, the test procedure is outlined.

It is not possible to study the motion (using a strobe light) because the shaft is confined within a casing. However, data on rotor speed and the displacement of the shaft in X and Y directions is gathered. This data is analyzed by making orbital plots as well as by estimating its spectral content, using a sequence identical to the analysis of the disc planar model.

In this chapter the rationale behind the design of the model is discussed. A brief description of the test set up and instrumentation is presented. Finally, the test procedure is outlined.

7.2 Modelling

The scaling calculations for the drilling dynamics experiment are

shown in Table 5. The prototype dimensions are consistent with the data presented in Appendix D. The dimensionless parameters can be grouped into two categories corresponding to geometric and dynamic similitude respectively. The geometric parameters are $(\frac{BD}{12L})$, $(\frac{D}{12L})$, $(\frac{d}{12L})$, where L is the length, BD is the bit diameter, D is the shaft outer diameter, and d is the shaft inner diameter and the units are as specified in column one of the table. The dynamic parameters are Reynolds number (the ratio of inertial and viscous forces), axial load/critical buckling load, weight of the shaft in fluid/critical buckling load, operating speed (ω)/natural frequency and flow velocity/(ωD^3). A spread sheet program was developed by Vandiver (1986) which calculates these parameters and allows for an iterative choice of model dimensions.

The following features were identified as the requirements for a reasonable model:

1. The system must model the non-dimensional parameters as closely as possible.
2. It ought to be able to reach a speed that excites vibrations well beyond the first natural frequency but should not exite the second mode.
3. It should have enough eccentricity to cause an appreciable amount of rubbing.
4. All the flexibility must be achieved through the shaft, all the other elements (especially the casing) must be rigid compared to the shaft.
5. The rotor must be able to withstand rubbing and wear.
6. The bearings must have a minimal clearance.

TABLE 5: Real Apparatus Parameters

Scaling Law Calculations for Drilling Dynamics Experiments

Prototype Parameters		Dimensionless Groups	
L, Length (ft) =	60	BD/12L	.0121528
BD, Bit Dia (in) =	8.75	D/12L	.0090278
D, Collar OD (in) =	6.5	d/12L	.0039167
d, Collar ID (in) =	2.82	(p-pm)/p	.85
p, Density (SL/ft^3) =	15	Phi	0
pm, Mud Density (SL/ft^3) =	2.25	Re = D^2W/Nu	586805.6
WOB (lbs) =	20000	WOB/Pcrit =	.4141398
E, Young's Mod (PSI) =	30000000	Wt in Fluid/Pcrit	.0953404
g, Gravity $(ft/S2)^2$ =	32.17	Mass Coef =	1.958678
ϕ, Hole Angle (DEG) =	0	W/Wncrit =	2.680746
RPM =	100	Q/EW^3 =	.7738216
$N\mu_2$, Kinematic VIS (ft^2/sec)	.00005		
Q, Mud Flow (ft^3/sec	.5		
Top Wt =	15395.74		
Pcrit =	48292.87		
Added Mass Coef =	5		
Mode Number n =	1	Nat Freq Mode n =	.6217175
		Wncrit(RPM) =	37.30305

7. Simulation of the correct flow regeme.

8. Ease of measurement.

The actual design involved a number of iterations. Concessions had to be made on some features in order to arrive at a feasible set up. The following factors governed the final design:

1. An existing drive unit that could run up to a speed of 65 Hz.
2. Two available non-contact proximity probes. These could sense steel rod of 3/4" outer diameter from 0 to 0.125 inches.
3. Since the primary aim of the test was to study the external rubbing, it was decided that the internal flow could be ignored. A solid shaft was used.
4. For the size of the model chosen, it would be extremely difficult to model the external flow rate accurately. The flow rate parameter was not modeled. The fluid inlet was kept under a pressure of one foot of water head, and the outlet kept open, so that the fluid was flowing at a very small speed during the test. This speed, however, was not recorded.
5. The effect of the axial load on the drill string is not included.
6. It was decided to orient the axis of the model in the horizontal direction.
7. The probes tend to exhibit a coupled behavior when mounted close to each other. Since the test is essentially geared to study the response in the first mode, it was decided to mount the probes symmetrically about the mid span of the shaft.

Further, the region of the casing enclosing the probes had to be made with plexiglass so as to avoid any effect of the casing on the measurements. The plexiglass construction also allowed a (partial) window to study the behavior of the shaft.

Based on these considerations, the actual parameters were chosen iteratively. Table 6 gives the model parameters in air. The natural frequency of the shaft (see section 4.2 for the formulation) was 49.206 Hz in air. Table 7 gives the model parameters in water. The natural frequency of the shaft assuming an added cass coefficient of 4.0 is 39.828 Hz. This particular choice of parameters does not match the dimensionless constants closely. However, they are within similar range. It was felt that as a first attempt (and under the available resources), this particular model could serve as an acceptable vehicle to study drill string vibrations with rubbing.

7.3 Test Set Up and Measurements

Figure 22 shows the plan view of the test apparatus and supports. Figures 23 and 24 show the details of the end coupling and the probe mounting arrangement respectively. These figures are taken from Cashman's (1987) thesis. This thesis also presents the details of the model fabrication and construction.

The length of the shaft between the two bearings is 2.9 feet. The shaft diameter is 0.75 inches. The shaft is made of mild steel. The internal diameter of the casing is 0.88 inches. The casing is made from a seamless stainless pipe of 1 inch outer diameter.

TABLE 6: Model Parameters (in air)

Actual Parameters		Actual Dimensionless Groups	
L, Length (ft) =	2.9	BD/12L	.0252874
BD, Bit Dia (in) =	.88	D/12L	.0215517
D, Collar OD (in) =	.79	d/12L	0
d, Collar ID (in) =	0	(p-pm)/p	.8684211
p, Density (SL/ft^3) =	15.2	Phi	0
pm, Mud Density (SL/ft^3) =	2	Re = D^2W/Nu	994531.3
WOB (lbs) =	0	WOB/Pcrit =	0
E, Young's Mid (PSI) =	30000000	Wt in Fluid/Pcrit	0
g, Gravity $(ft/S2)^2$ =	32.17	Mass Coef =	1
ϕ, Hole Angle (DEG)	0	W/Wncrit =	.8623565
RPM =	2546	Q/WD3	0
$N\mu$, Kinematic VIS (ft^2/sec)	.00001		
Q, Mud Flow (ft^3/sec) =	0		
Top Wt =	0		
Pcrit =	3798.800		
Added Mass Coef =	0		
Mode Number n =	1	Nat Freq Mode n =	49.20625
		Wncrit(ROM) =	2952.375

TABLE 7: Model Parameters (in water)

Actual Parameters		Actual Dimensionless Groups	
L, Length (ft) =	2.9	BD/12L	.0252874
BD, Bit Dia (in)	.88	D/12L	.0215517
D, Collar OD (in) =	.75	d/12L	0
d, Collar ID (in) =	0	(p-pm)/p	.8682211
p, Density (SL/ft^3) =	15.2	Phi	0
pm, Mud Density (SL/ft^3) =	0	Re = D^2W/Nu	994531.3
WOB (lbs) =	0	WOB/Pcrit =	0
E, Young's Mod (PSI) =	30000000	Wt in Fluid/Pcrit	0
g, Gravity (ft/S2) =	32.17	Mass Coef =	1.526311
ϕ, Hole Angle (DEG) =	0	W/Wncrit	
RPM =	2546	Q/WD3 =	0
Nμ, Kinematic VIS (ft^2/sec) =	.00001		
Q, Mud Flow (ft^3/sec) =	0		
Top Wt =	0		
Pcrit =	3798.800		
Added Mass Coef =	4	Nat Freq Mode n =	39.82888
Mode Number n =	1	Wncrit(RPM) =	2389.733

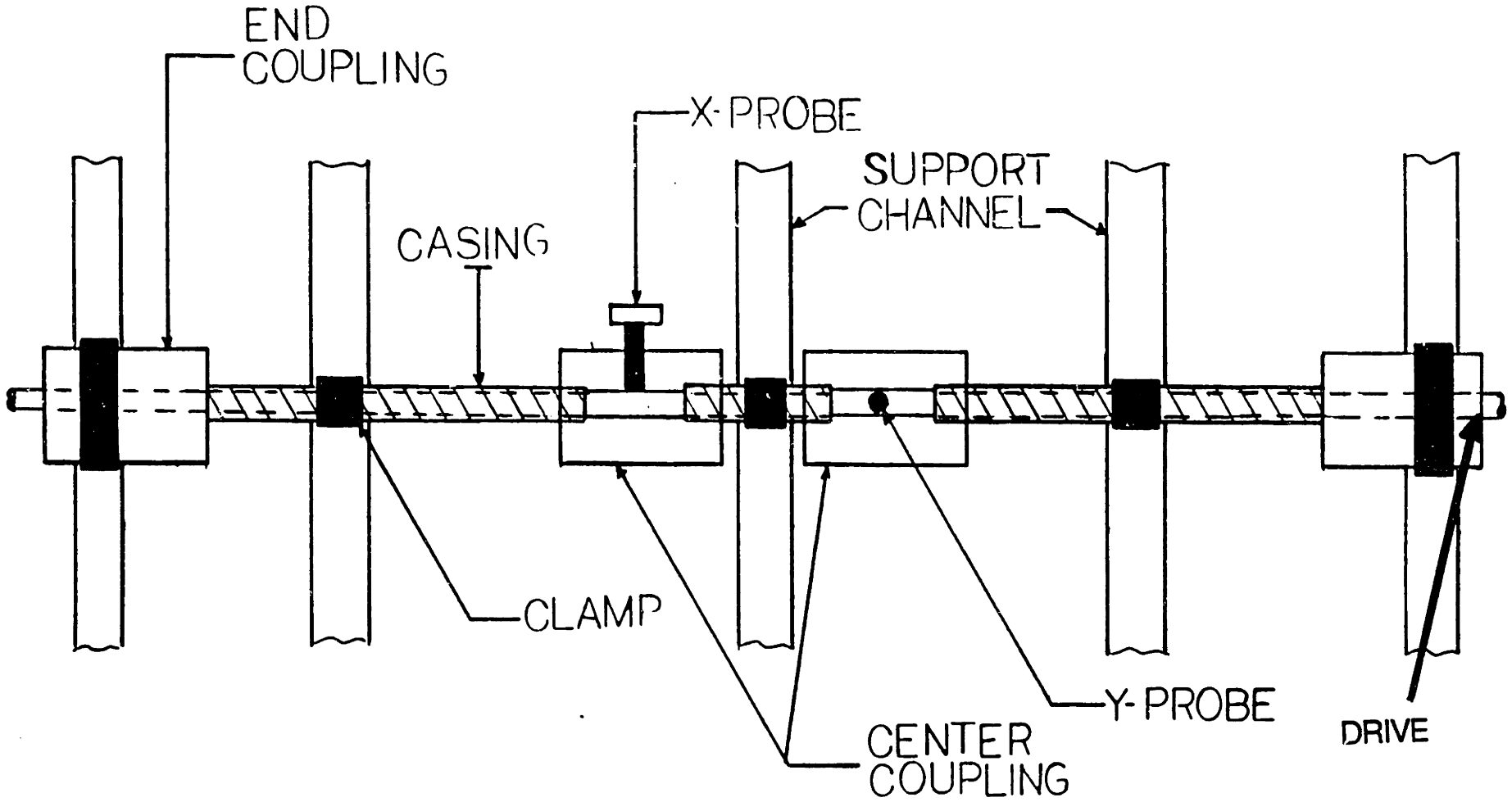

FIGURE: 22 TEST APPARATUS AND SUPPORTS
PLAN VIEW (SCALE 1/4" = 1 ")

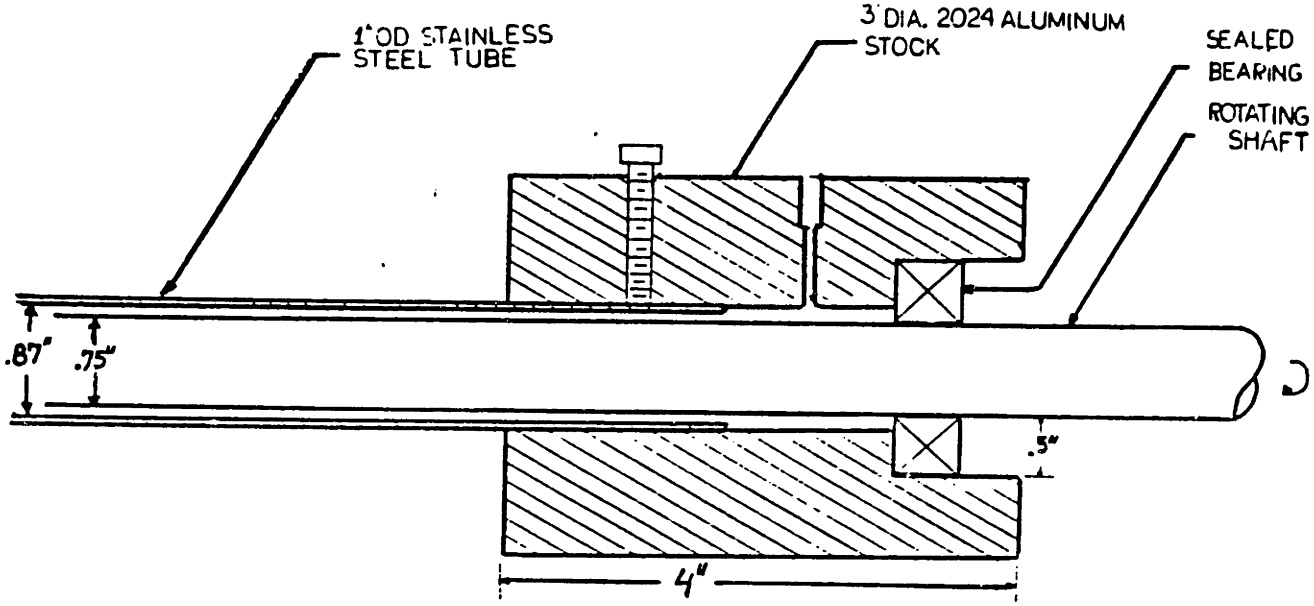

FIGURE : 23 END COUPLING

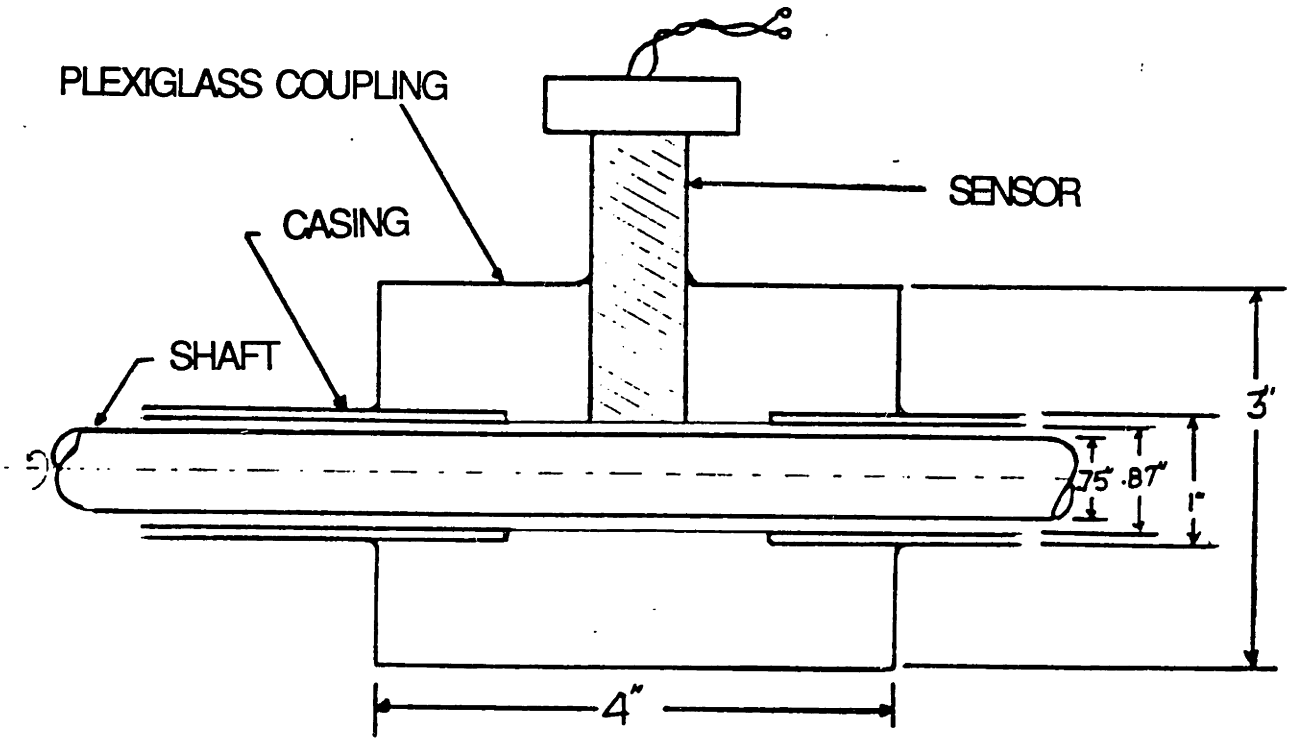

FIGURE : 24 CENTER COUPLING

The X and Y displacement as well as the speed of rotation of the shaft was recorded. The drive unit and the configuration of the instrumentation was identical to the system described in Section 4.3. The reader may also refer to section 4.5 for details of data reduction.

7.4 Test Procedure

The test sequence is essentially identical to the one used for the planar model. The three major stages were:

i. preliminary vibration tests

ii. calibrations

iii. rotor dynamic/rubbing tests in air

iv. rotor dynamic/rubbing tests in water

For the vibration test various parts of the system were excited with an impulse hammer. These are discussed in the Appendix.

Calibration tests were carried out on the probes by removing a part of the casing and displacing the shaft statically. The probes were mounted in their final position during these tests. The same data acquisition system/procedure was used for calibration and the final data collection. Typically 210 data points were sampled at 500 Hz for each calibration test. The gap between the probe and the shaft was set at 0.06 inches for the final measurements.

The rotor dynamic tests were conducted in air first. Subsequently, fluid was introduced. For each of these tests the rotor speed was increased in discrete steps to pass through the first natural frequency and then reduced in steps to zero speed. For each speed two sets of data were acquired. First 210 points were sampled

at 500 Hz. This data was used to make the X-Y plots. Then 4096 points were taken at 200 Hz. This data was used for spectral estimation and added mass computations.

The details of the test matrix are tabulated in Appendix B.

CHAPTER 8: RESULTS AND DISCUSSIONS OF DRILL COLLAR MODEL TESTS

8.1 Drill String Model Tests

The drill collar model has been assembled. Preliminary tests have been carried out to understand the nature of rubbing phenomena in the presence of fluid, and the added mass coefficient has been computed.

In this chapter some preliminary results of the tests have been reported. This is followed by a section on the computation of added mass coefficient. Finally a critique of the tests carried out so far is presented. This covers a discussion on some problems faced in the preliminary tests and recommendations for future tests.

8.2 Preliminary Test Results

Impulse response tests were carried out to measure the natural frequency and modal damping of the system.

Figures C6 and C7 show the transfer function for the response of the shaft in the horizontal and vertical planes respectively. First natural frequency in the horizontal direction was 50 Hz. The first natural frequency in the vertical direction was 55 Hz. Because of the difference in these responses, the transfer function showed split peaks. The half power bandwidth of these modes is 3.5 and 4.0 Hz respectively. The modal damping ratio (in air) is

$$\zeta_1 \simeq 0.06$$

The theoretical value of the first natural frequency in air is 49.2 Hz (from to Table 6). The first natural frequency in water is 39.82 Hz (from to Table 7).

The results of rotor dynamic tests are summarized in Table 8.

TABLE 8: Results of Drill String Model Tests

Speed of Shaft Hz	Test Number	Condition	Orbital Plots Number	Orbital Plots Nature of Rub
12.8	202	A, U	E24	No
17.5	203	A, U	E25	Full
20.2	204	A, U	E26	No
30.0	205	A, U	E37	No
43.0	206	A, U	E28	No
52.0	207	A, U	E29	Full
68.0	208	A, U	E30	No
55.0	209	A, D	E31	Full
42.0	210	A, D	E32	Part
30.0	211	A, D	E33	No
20.0	212	A, D	E34	Part
15.0	213	A, D	E35	Full
12.0	214	A, D	E36	No
9.5	216	W, U	E37	No
13.0	216	W, U	E38	Full
20	217	W, U	E39	Part
27.0	218	W, U	E40	No
38.6	219	W, U	E41	Full
53.0	220	W, D	E42	No
46.0	221	W, D	E43	Full
32.0	222	W, D	E44	No
19.4	223	W, D	E45	Full
15.4	224	W, D	E46	No
		Repeat Tests		
13.5	225	W, U	E47	Part
16.0	226	W, U	E48	Full
10.0	227	W, D	E49	Part

NOTE: U - speeding up; D - slowing down; A - air; W - water.

The orbital plots and spectra have been analyzed in the manner described in Section 5.1.

The spectral estimate of test #203 (driven at 17.5 Hz, see Figure 25) shows that the major component of the response is at its natural frequency (48.0 Hz). It was possible to run the in-water test at low speeds without loosing fluid (test #226, driven at 16 Hz, see Figure 26), and since the natural frequency was excited, two data sets of full annular rub are available, one in air and the other in water. Added mass coefficients can be extracted from this data.

A comparison of the spectra of the two cases show that the natural frequency in air and water is 48.0 and 38.0 Hz respectively. This is in close agreement with the theoretical values reported earlier. Further

$$\left(\frac{(\omega_1)a}{(\omega_1)f}\right)^2 = \frac{\rho_s + \rho_f C_m}{\rho_s}$$

where

$(\omega_1)a$ = first natural frequency in air

$(\omega_1)w$ = first natural frequency in waer

ρ_w = density of steel

ρ_f = density of water

C_m = added mass coefficient

Thus

$$C_m = 4.67$$

For comparison from the Figure 17, for

$$D/d = 1.13$$

$$S = \infty$$

The added mass coefficient is 5.5. It must be realized that this data

Test # 203 IN AIR
Drill Collar Model (Speeding up)
Drive Shaft speed 17.5 Hz
Sampled at 200 Hz, 1024 point FFT
4 Averages, Resolution 0.195 Hz

Full Annular Rub

SPECRTRAL DENSITY IN INCH SQ/ HZ

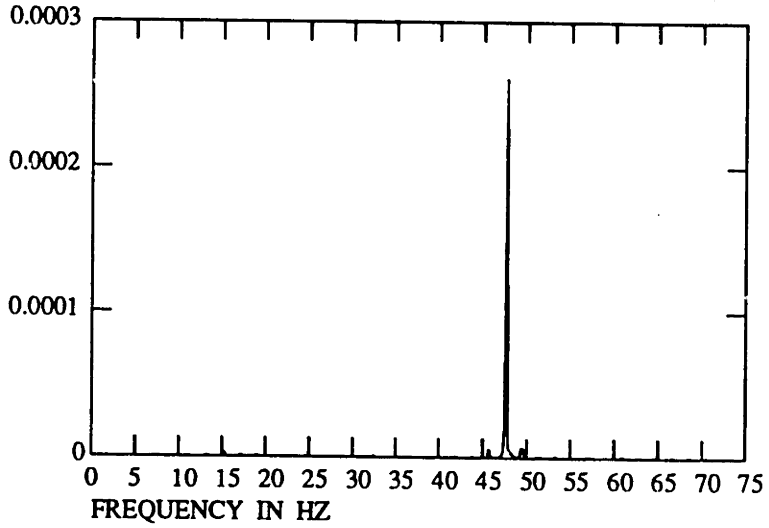

X SPECTRUM

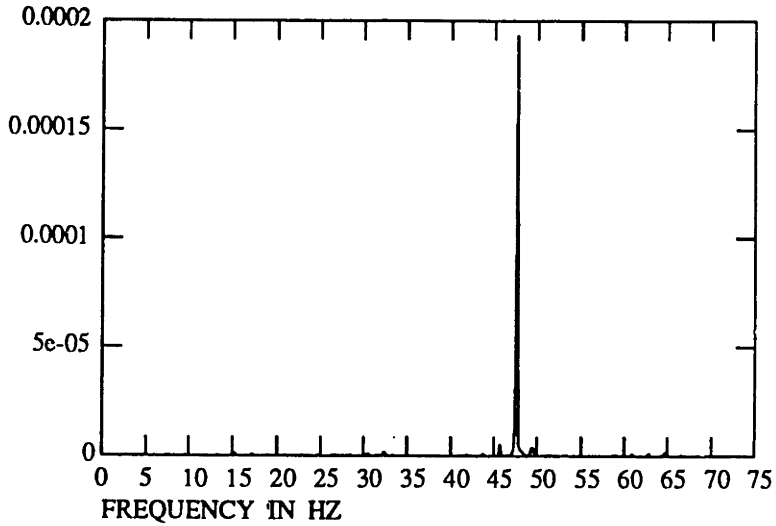

Y SPECTRUM

FIGURE : 25

Test # 226 IN WATER
Drill Collar Model (Speeding up)
Drive Shaft speed 16.0 Hz
Sampled at 200 Hz, 1024 point FFT
4 Averages, Resolution 0.195 Hz

Full Annular Rub

SPECRTRAL DENSITY IN INCH SQ/ HZ

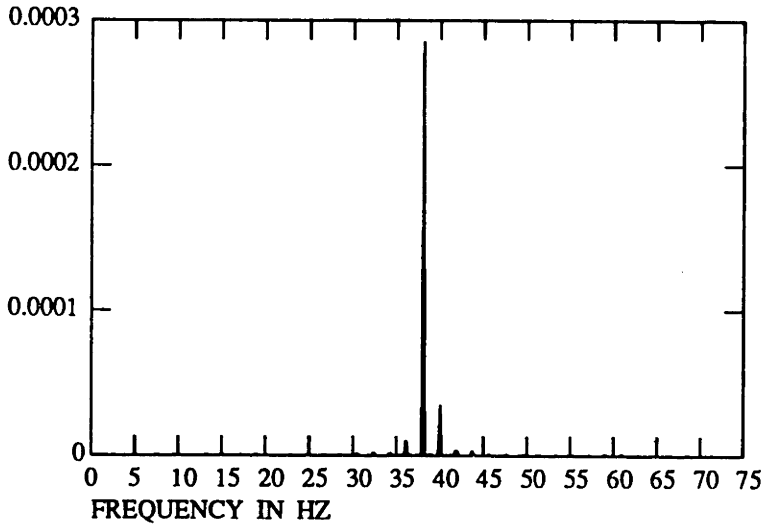

X SPECTRUM

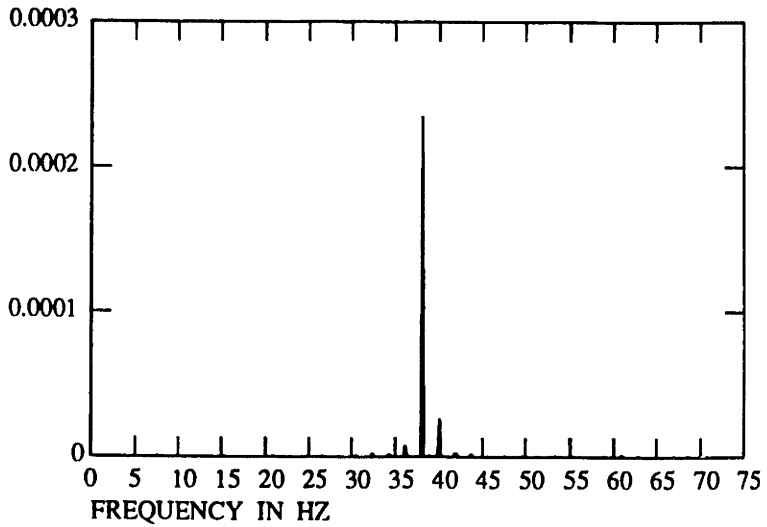

Y SPECTRUM

FIGURE : 26

from Figure 19 was valid for a vibrating rod that was not rotating.

The following general conclusions may be drawn from these tests:

1. The procedure for modelling and studying the experimental behavior of drill string model is established.
2. The added mass can be computed from these tests.
3. The system shows full synchronous rub in the vicinity of its natural frequency.
4. The added mass coefficient varies with the amount of fluid in the annular space.
5. The rubbing action is much smoother in the presence of fluid due to the reduction in the friction. The stick-slip action is almost negligible due to the lubricating action of the fluid.

8.3 Critique and Recommendations

A systematic analysis of the rotor dynamic test data has not been presented due to a problem encountered during these tests.

The rotor dynamic tests were carried out in air first, and fluid was introduced in the later tests. During the dry tests (in air) an unexpected full annular rub was registered at the speed of 17.5 Hz. The possible source of this occurrence was identified as subharmonic resonance excited due to stiffness asymmetry (in the X and Y plane, as evidenced by the difference in the natural frequencies). This type of excitation at $\frac{\omega_n}{3}$ can lead up to an instability (Riegger and Crofoot, 1978). It was also noticed that there was an unacceptably large play in the bearings (shown in Figure 23) that led the shaft to flop. Subsequently, when water was introduced in the annular space these

bearings lead to a significant amount of leakage. Further, as the rotor speed was stepped up, increasingly large quantities of fluid was lost. Eventually on returning to zero speed almost half the fluid was gone. Some more tests were tried by applying some external sealants, but there was feasibly only at low speeds (#225, 226, 227).

The performance of the bearings has been the major source of concern in the drill string model test. It has already been pointed out that the large clearance could have caused the resonance at $(\frac{1}{3})$ driving speed. It certainly caused unacceptably large leaks.

The range and linearity of the eddy current probe has been a constant source of error. It seems that the calibration on these probes could be largely inaccurate.

The wear of the shaft (steel rubbing on steel) may be significant, especially for the dry (in air) tests.

The most obvious recommendation is that the bearings on the drill string model be replaced by a set of bushings that have a much lesser clearance. This will alleviate the shaft flop as well as the leakage.

Similarly, the drill string tests ought to be tried in fluids of different viscosity. This would also lead to some useful added mass coefficient data.

CHAPTER 9: CONCLUSIONS

Two models were designed and constructed in order to study the rotor motion accompanied by radial rub.

The first set up was used to study the validity of a full annular rub theory proposed by Stackley. This model was able to simulate the behavior of a single degree of freedom (Planar) disc whirling within a casing. From this study it is concluded that:

i. Based on three dimensionless parameters (1) ζ (the damping ratio), (2) ε (the eccentricity to clearance ratio), and (3) μ (the friction coefficient) - the theory accurately predicted the limited synchronous rub.

ii. There is a good match between the theoretical prediction and the observed value of shaft speed at which the rub initiates.

iii. The range of speeds for full radial rub while increasing the speed is wider than that for slowing down.

iv. It was not possible to simulate backward whirl experimentally. This was attributed to the tendency of the drive system to change its speed so that it would have a minimal load.

v. Contrary to the assumptions made in the theoretical full annular rub model, the real system exhibits a significant region of partial rub at rotation rates just below and above the full annular rub range.

The second part of experimental study was aimed at the simulation of a drill string rubbing within a casing in the presence of fluid in the annular space. The procedure for modelling and studying the rub is established. The orbits of whirling accompanied by rubbing were studied. Finally, the added mass coefficient was computed from the

shift in the natural frequency of the system due to introduction of fluid in the annular space. The added mass coefficient is estimated as 4.67. This value is well within the acceptable limits of the value projected by theoretical analysis.

REFERENCES

1. Belkheria, Karem, The Effects of Radial Rubbing on Drill Collar Vibrations, Ocean Engineering Thesis, M.I.T., Cambridge, 1986.

2. Bol, G.M., Effect of Mud Composition on Wear and Friction of Casing and Tool Joints, SPE Drilling Engineering, pp. 369-376, October 1986.

3. Cashman, Edward, "An Experimental Investigation of Shaft Whirl with Rub", S.B. Thesis, M.I.T., Cambridge, 1987.

4. Chen, S. S., Wambsganss, M.W., Jendrzejczyk, Added Mass and Damping of a Vibrating Rod in Confined Viscous Fluids, Journal of Applied Mechanics, pp. 326-329, June 1976.

5. Childs, D.W., Fractional Frequency Rotor Motion Due to Non-symmetrical Clearance Effects, ASME Paper No. 81-GT-145, Journal of Eng. for Power, March 1981.

6. Crandall, S.H., Physical Nature of Rotor Instability Mechanism, Rotor Dynamical Instability, ASME Special Publication, AMD Vol. 55, pp. 1-18, 1983.

7. Daring, D.W., Livesay, B.J., Longitudinal and Angular Drill String Vibrations with Damping, Journal of Engineering for Industry, pp. 671-679, November 1968.

8. Dimaragonos, A.D. and Paipetis, S.A., Analytical Methods in Rotor Dynamics, Applied Science Publications, 1983.

9. Ehrlich, E.F., "The Dynamic Stability of Rotor/Stator Radial Rubs in Rotating Machinery", ASME, Vol. 56, No. 6, 1969.

10. Den Hartog, J.P., "Mechanical Vibrations", 2nd Ed., McGraw-Hill, New York, 1940.

11. Jeffcott, H.H., "The Lateral Vibration of Shafts in the Neighborhood of a Whirling Speed - The Effect of Want of Balance", Phil. Mag., Series 6, Vol. 37, page 304, 1919.

12. Kascak, A.F., Effects of Different Rub Models on Simulated Rotor Dynamics, NASA Technical Paper 2220, AVSCOM Technical Report 83-C-8-1984.

13. Matsusita, O., Tahegi, M., Kikuchi, K., Kaga, M., Rotor Vibration caused by External Exitation and Rub, Proceedings of Rotor Instability Problems in High Performance Turbomechanics, pp. 105-129, 1982.

14. Muszynska, A., "Synchronous and Self Exited Rotor Vibrations Caused by Full Annular Rub", Bentley Nevada Corporation, October 1985.

15. Muszynska, A., "Partial Lateral Rotor to Stator Rubs", Third International Conference: Vibration of Rotating Machinery, York, U.K., 1984.

16. Newkirk, B.L., "Shaft Whipping", General Electric Review, Vol. 27, p. 169, 1924.

17. Newkirk, B.L. and Taylor, H.D., "Oil Film Whirl - An Investigation of Disturbances on Oil Films in Journal Bearings", General Electric Review, Vol. 28, 1925.

18. Rabinowicz, E., Friction and Wear of Material, John Wiley and Son, New York, 1965.

19. Rankine, W.J., "On the Centrifugal Forces of Rotating Shafts", Engineer London, Vol. 27, p. 249, 1869.

20. Rao, J.S., Rotor Dynamics, Halsted Press Book, John Wiley and Sons, New York, 1983.

21. Riegger, N.F. and Crofoot, J.F., Vibrations of Rotating Machinery, Part I: Rotor-Bearing Dynamics, The Vibration Institute, Clarendon Hills, Illinois, 1977.

22. Stackley, S.J., Dynamics of Full Annular Rotor Rub, Ocean Engineering Thesis, M.I.T., Cambridge, 1986.

23. Subbiah, R., Bhat, R.B., Sankar, T.S., Rao, J.S., Backward Whirl in a Simple Rotor Supported on Hydrodynamic Bearings, Instability of Rotating Machinery, Proceedings of Symposium held at Carson City, Nevada, pp. 145-153, 1985.

24. Tondl, A., "Some Problems in Rotor Dynamics", published by Czechoslovikian Academy of Sciences, Prague, 1965.

25. Vandiver, J.K., Dynamic Analysis of Woodpecker Drill Collar, Department of Ocean Engineering Report (unpublished), M.I.T., Cambridge, 1985.

26. Wolf, S.F., Zackerhause, M., Arian, A., Field Measurements of Downhole Drill String Vibrations, Paper SPE 14330, Society of Petroleum Engineering.

APPENDIX A: PARTIAL RUB

The discussion presented here is largely based on Muszynska's (1984) work on partial lateral rotor to stator rub.

Partial rub occurs when the rotor contacts the stator occasionally during a fraction of the period of precession. The physical phenomena of the introduction of frictional force and modification of stiffness are similar in partial rub and full annular rub. In fact the full annular rub ought to be viewed as a limiting case of partial rub. But some additional phenomena occurs with partial rubbing. Consecutive impacting may create a significant average value of radial force with a resultant tendency of the shaft center to move away from the rub location. The characteristic features of partial rub: impact, friction, and modification of stiffness, are discussed here.

Impact

The precessional motion velocity is proportional to the displacement of rotor (from the center point of the orbit). This velocity is much lower in order of magnitude than the surface velocity which is proportional to the radius of shaft. This surface velocity has a significant effect on the impact. After impact, the rotor responds with transient lateral and torsional response. The direction of rebound depends on the relative locations of rotor and stator, surface of contact, and the rotational velocity at the circumference of the rotor. The rebounding can lead the rotor into the original forward orbit or into backward whirl. The frequency content of the response has a combination of the rotor natural

frequencies (the most dominant response is usually at the first natural frequency). The free vibration response of the rotor gets superposed on the prevailing rotational motion leading up to complicated, but often repetitive orbits.

Friction

It is well known that the magnitude of frictional force depends on the normal force and the surface properties. The direction of frictional force opposes the direction of the relative velocity between the rotor and the stator.

When the contact is made the direction of rotation is predetermined and the magnitude of the friction is influenced by the magnitude of imbalance. The resulting force varies depending on whether the contact is for a fraction of the cycle (partial) or continuous.

The frictional forces cause the drive to put out additional torque which interacts with the driving imbalance. This usually generates heat and wear and often decreases the rotational speed. The net effect is a variability in the rub conditions. Another commonly known side effect of this event is generation of a familiar noise - acoustic wave that contain a wide range of frequencies.

Presence of fluid in the annular space will always reduce the frictional force. The orbital plots of motions in presence of fluid are much more smoother than otherwise.

Finally, a comment about the friction values in real life drill strings. Usually there is a high amount of sand found in the drilling fluid. Sand can cause the frictional coefficient to run really high.

It is foreseeable to see friction coefficients as high as 1.0 at local spots. Backward whirl is a distinct possibility for partial rub in regions of high frictional coefficients.

APPENDIX B: TEST MATRIX

The details of the test are presented in tabular format.

TABLE B1: Rub Tests on Planar Model

Number	Test Number	Shaft Speed in Hz	Condition	Orbit Plot # (Appendix E)	Comment
1	700	14.1	Speeding up	E1	No rub
2	701	14.5	Speeding up	E2	
3	702	14.8	Speeding up	E3	
4	703	15.6	Speeding up	E4	
5	704	15.95	Speeding up	E5	
6	705	16.5	Speeding up	E6	Critical speed
7	706	16.9	Speeding up	E7	
8	708	17.5	Speeding up	E8	
9	707	18.0	Speeding up	E9	
10	709	18.6	Speeding up	E10	
11	710	19.0	Speeding up	E11	
12	711	20.0	Speeding up	E12	
13	712	24.4	Peak speed	E13	No rub
14	713	20.4	Slowing down	E14	
15	714	19.1	Slowing down	E15	
16	715	18.6	Slowing down	E16	
17	716	17.8	Slowing down	E17	
18	717	17.5	Slowing down	E18	
19	718	17.1	Slowing down	E19	Critical speed
20	719	15.5	Slowing down	E20	
21	720	14.8	Slowing down	E21	
22	721	14.4	Slowing down	E22	
23	722	13.5	Slowing down	E23	No rub

TABLE B2: Rub Tests on Drill Collar Model

Number	Test Number	Shaft Speed in Hz	Annular Space	Condition	Orbital Plot # (Appendix E)	Comment
1	202	12.8	Air	Speeding up	E24	
2	203	17.5	Air	Speeding up	E25	Unexpected full rub
3	204	20.2	Air	Speeding up	E26	
4	205	30.0	Air	Speeding up	E27	
5	206	43.0	Air	Speeding up	E28	
6	207	52.0	Air	Speeding up	E29	Critical speed
7	208	68.0	Air	Peak speed	E30	
8	209	55.0	Air	Slowing down	E31	
9	210	42.0	Air	Slowing down	E32	
10	211	30.0	Air	Slowing down	E33	
11	212	20.0	Air	Slowing down	E34	
12	213	15.0	Air	Slowing down	E35	
13	214	12.0	Water	Speeding up	E36	
14	215	9.5	Water	Speeding up	E37	The system lost water continuously as the rotor speeded up.
15	216	13.0	Water	Speeding up	E38	
16	217	20.0	Water	Speeding up	E39	
17	218	27.0	Water	Speeding up	E40	
18	219	38.6	Water	Speeding up	E41	
19	220	53.0	Water	Peak speed	E42	
20	221	46.0	Water	Slow down	E43	
21	222	32.0	Water	Slow down	E44	
22	223	19.4	Water	Slow down	E45	
23	224	15.0	Water	Slow down	E46	
24	225	13.5	Water	Speed up	E47	Repeat test with external seals.
25	226	16.0	Water	Peak	E48	
26	227	10.0	Water	Slow down	E49	No water loss.

APPENDIX C: IMPULSE RESPONSE TESTS

The objective of the impulse tests was to determine the vibrational response of the various components of the set up.

For the preliminary tests the system was excited with an impulse hammer. The output was measured with an accelerometer. The transfer functions (and coherence) were examined with the help of a B and K real time analyzer. Figure C1 shows the test set up. For all these tests the cutoff frequency was set at 400 Hz. The resolution of the estimates was set at 0.5 Hz. Eight averages were taken for each test. The sequence of the tests and observations are tabulated.

Plots showing the transfer function (in dB) between the acceleration (response) and the impulse input for the rotor and the casing are given. The coherence of these measurements is very close to unity (see plot C2 for a typical coherence reading). Unit coherence is an indication of the linearity of the system and implies that the transfer function measurements are reliable. The system natural frequency and modal damping are estimated from these plots. The transfer functions have a peak at each natural frequency (mode). If the bandwidth of the transfer function at a value 3 dB below the peak is $\Delta\omega$ (called the half power bandwidth), then the modal damping ratio is

$$\zeta_n = \frac{\Delta\omega}{2\omega_n}$$

where

ω_n = the natural frequency in mode n.

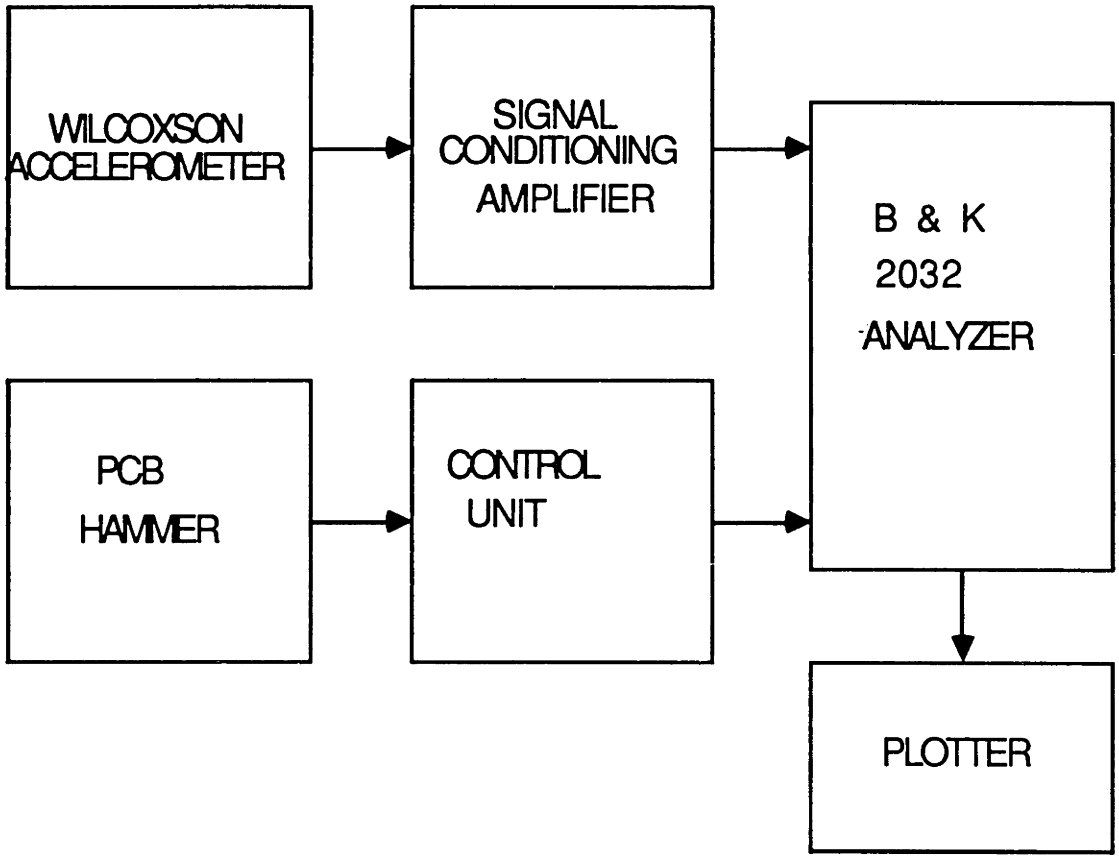

FIGURE C1 : INSTRUMENTATION FOR VIBRATION TESTING

TABLE C1: Impulse Response Tests on Planar Test Set Up

Test Number	Item	Accelerometer Location	Accelerometer Direction	Hammer Location	Hammer Direction	Result	Plot Number
V1	Shaft	$\frac{L}{4}$ from RMS	X	L/2	X	ω_1 = Hz	C3
V2	Shaft	"	Y	L/2	Y	ω_1 = Hz	C4
V3	Casing	Casing side	X	Casing side	X	First mode above 25 Hz	C5
V4	Casing	Casing top	Y	Casing top	Y	"	Not shown
V5	Bearing (left)	Left bearing	X	Shaft (L/2)	X	"	"
V6	Bearing (left)	Left bearing	Y	"	Y	"	"
V7	Bearing (right)	Right bearing	X	"	X	"	"
V8	Bearing (right)	Right bearing	Y	"	Y	"	"
V9	X Probe	Probe X	X	Probe support	X	"	"
V10	Y Probe	Probe Y	Y	"	Y	"	"
	Impulse response tests on Drill Collar Model						
T1	Shaft	$\frac{L}{2}$, shaft	X	Shaft (L/4) from RMS	X		C6
T2	Shaft	"	Y	"	Y		C7
T3	Coupling (left)	Coupling (left)	X	Left coupling	X	"	Not shown
T4	Coupling (left)	Coupling (left)	Y	Left coupling	Y	"	"
T5	Coupling (right)	Coupling (right)	X	Right coupling	X	"	"
T6	Coupling (right)	Coupling (right)	Y	Right coupling	Y	"	"
T7	Casing (left)	Casing (left)	X	Casing (left)	X	"	C8
T8	Casing (left)	Casing (left)	Y	Casing (left)	Y	"	Not shown
T9	Casing (right)	Casing (right)	X	Casing (right)	X	"	"
T10	Casing (right)	Casing (right)	Y	Casing (right)	Y	"	"
T11	Casing (center)	Casing (center)	X	Casing (center)	X	"	"
T12	Casing (center)	Casing (center)	Y	Casing (center)	Y	"	"
T13	X Probe	Probe X	X	Casing (center)	X	"	"
T14	Y Probe	Probe Y	Y	Casing (center)	Y	"	"

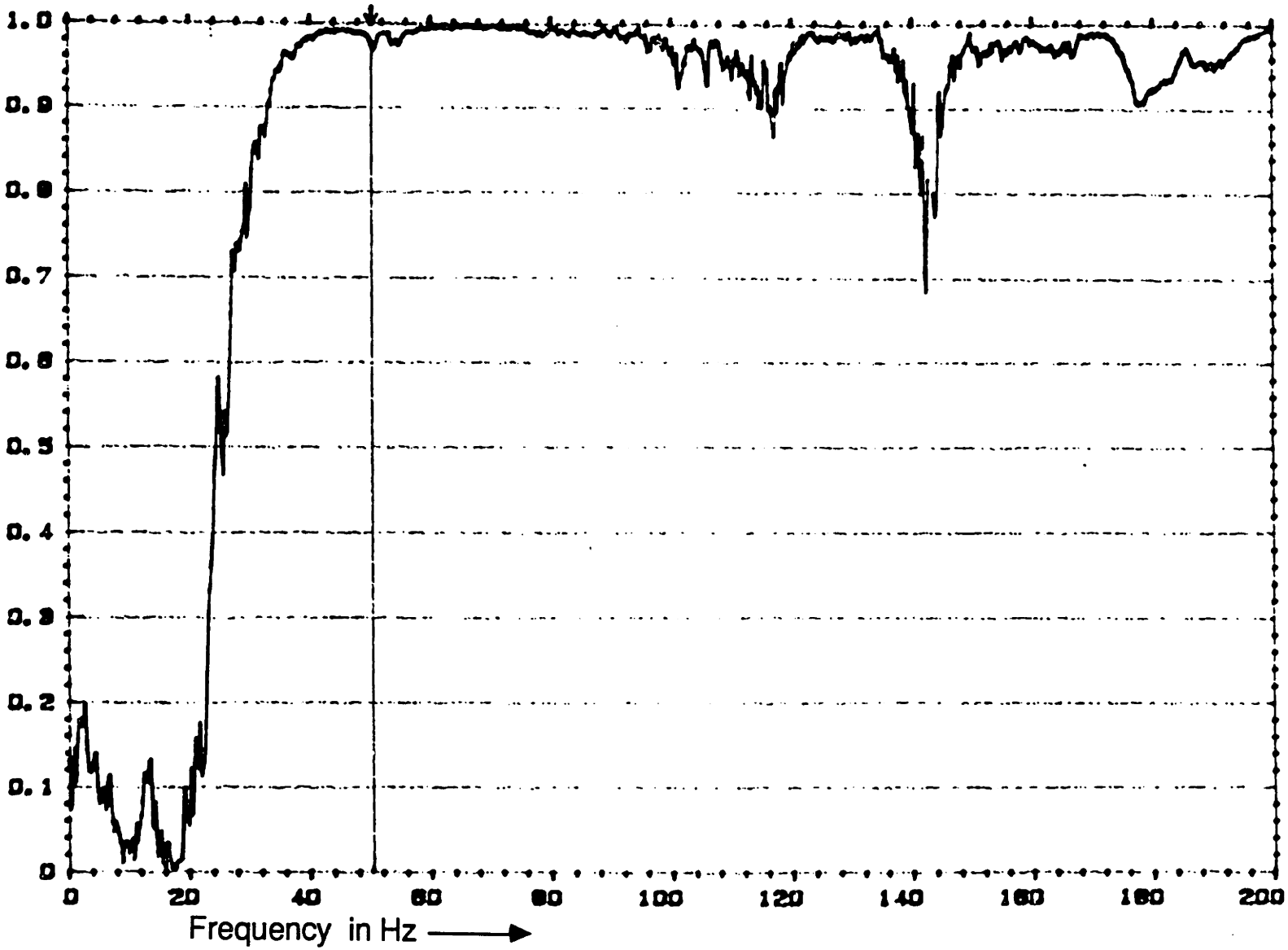

FIGURE C2: COHERENCE FOR TEST # T1

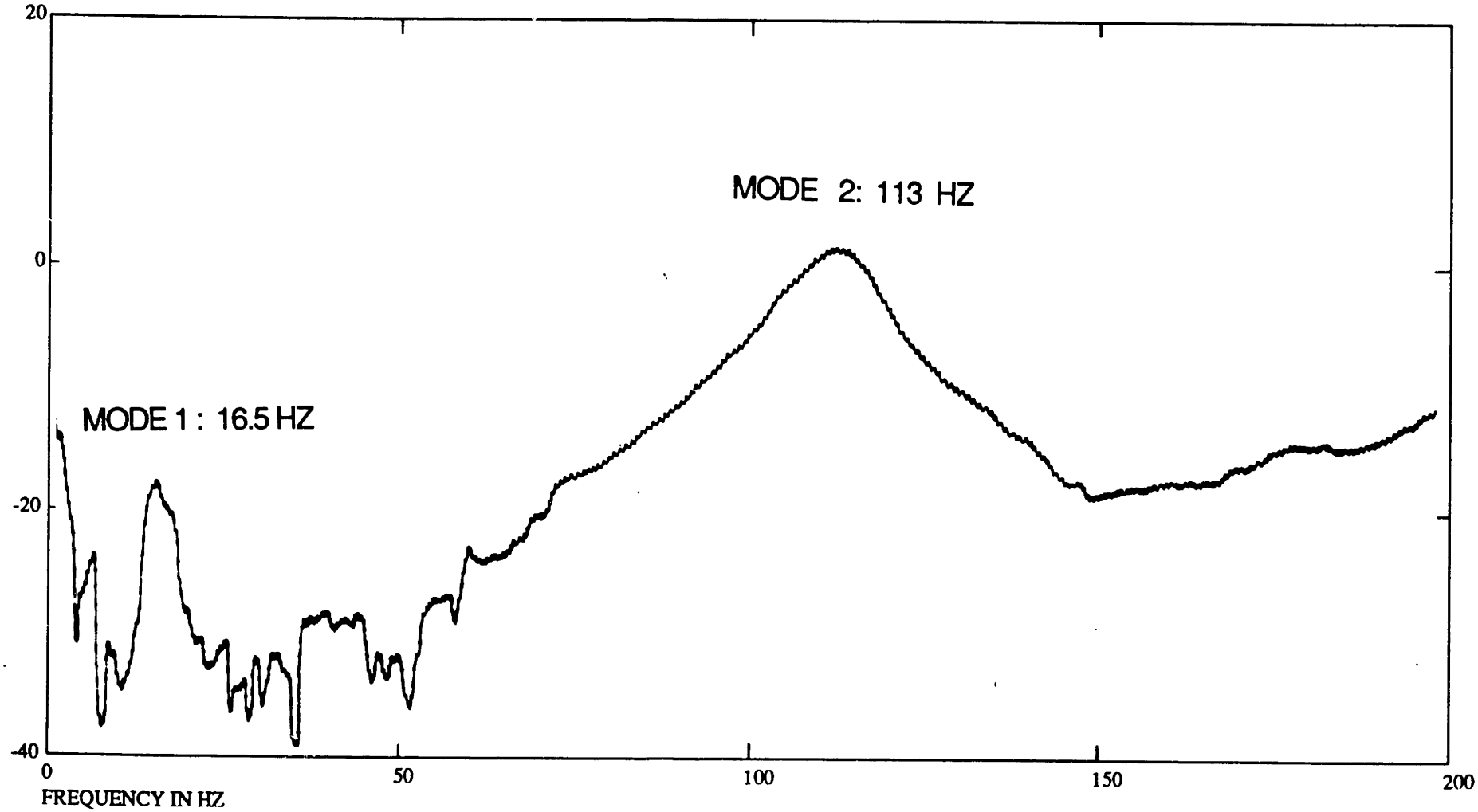

FIGURE C3 : TRANSFER FUNCTION (IN dB) FROM IMPULSE TEST
(Test # V1 , on the Planar model in X direction)

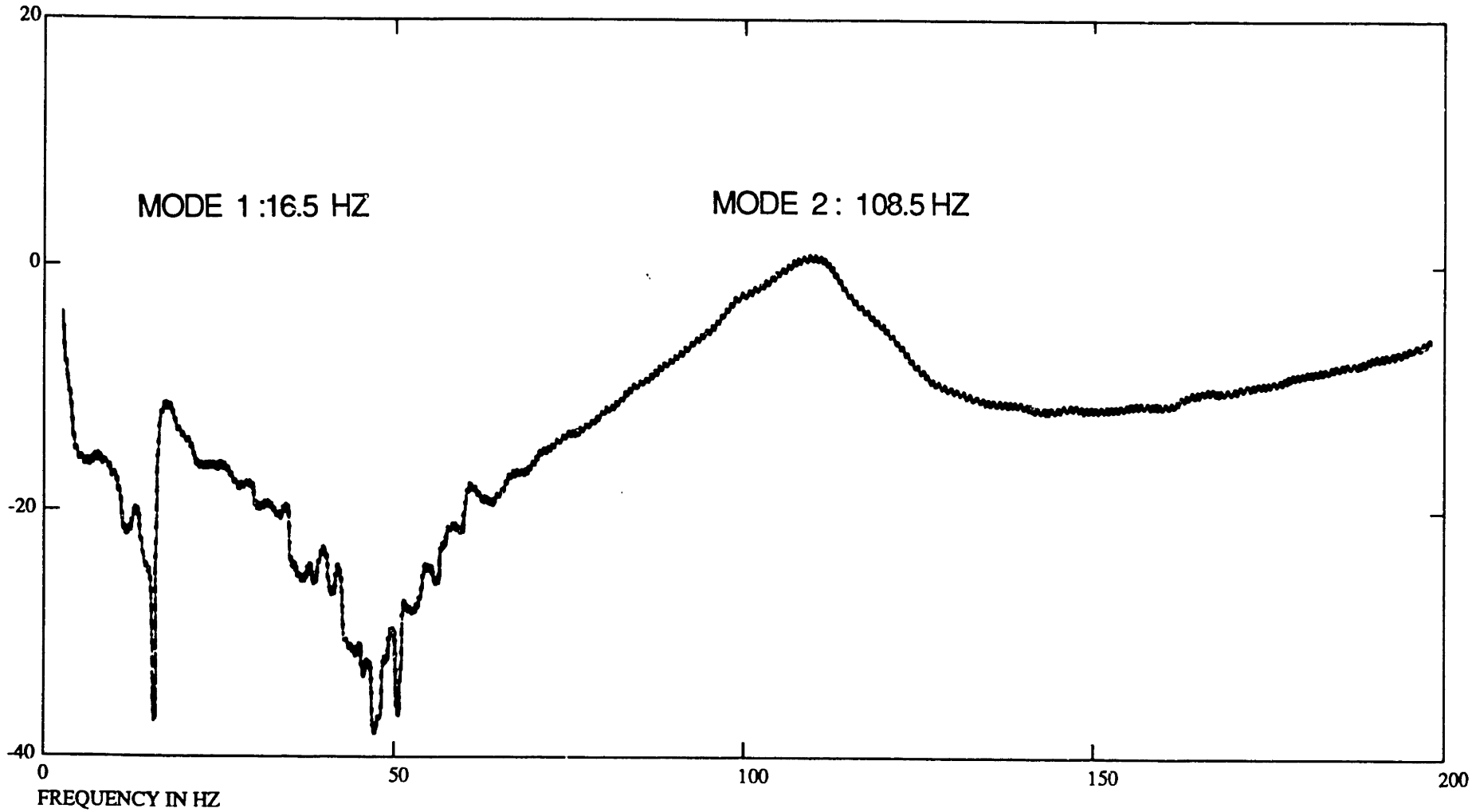

FIGURE C4 : TRANSFER FUNCTION (IN dB) FROM IMPULSE TEST
(Test # V2 , on the Planar model in y direction)

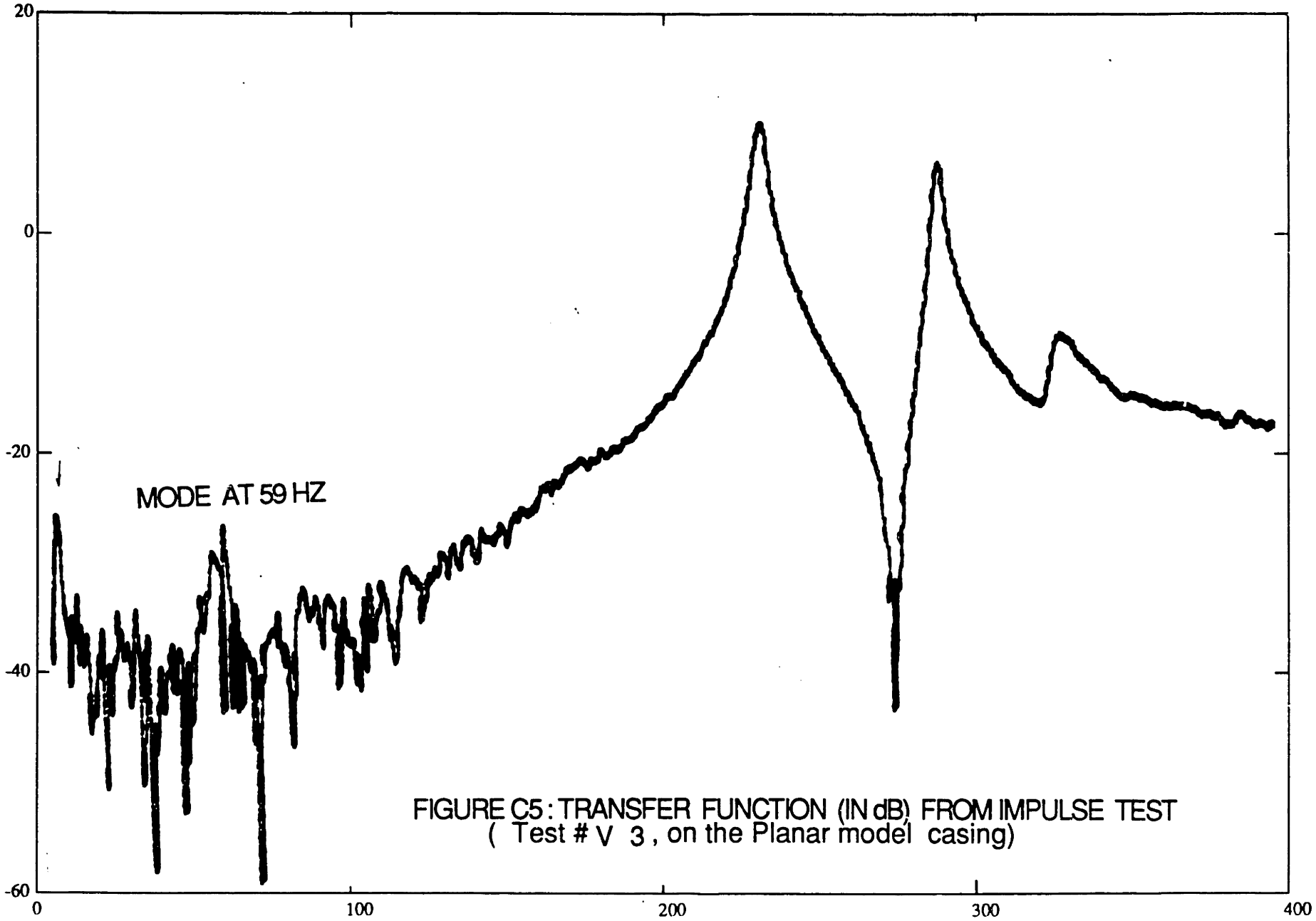

FIGURE C5 : TRANSFER FUNCTION (IN dB) FROM IMPULSE TEST
(Test # V 3 , on the Planar model casing)

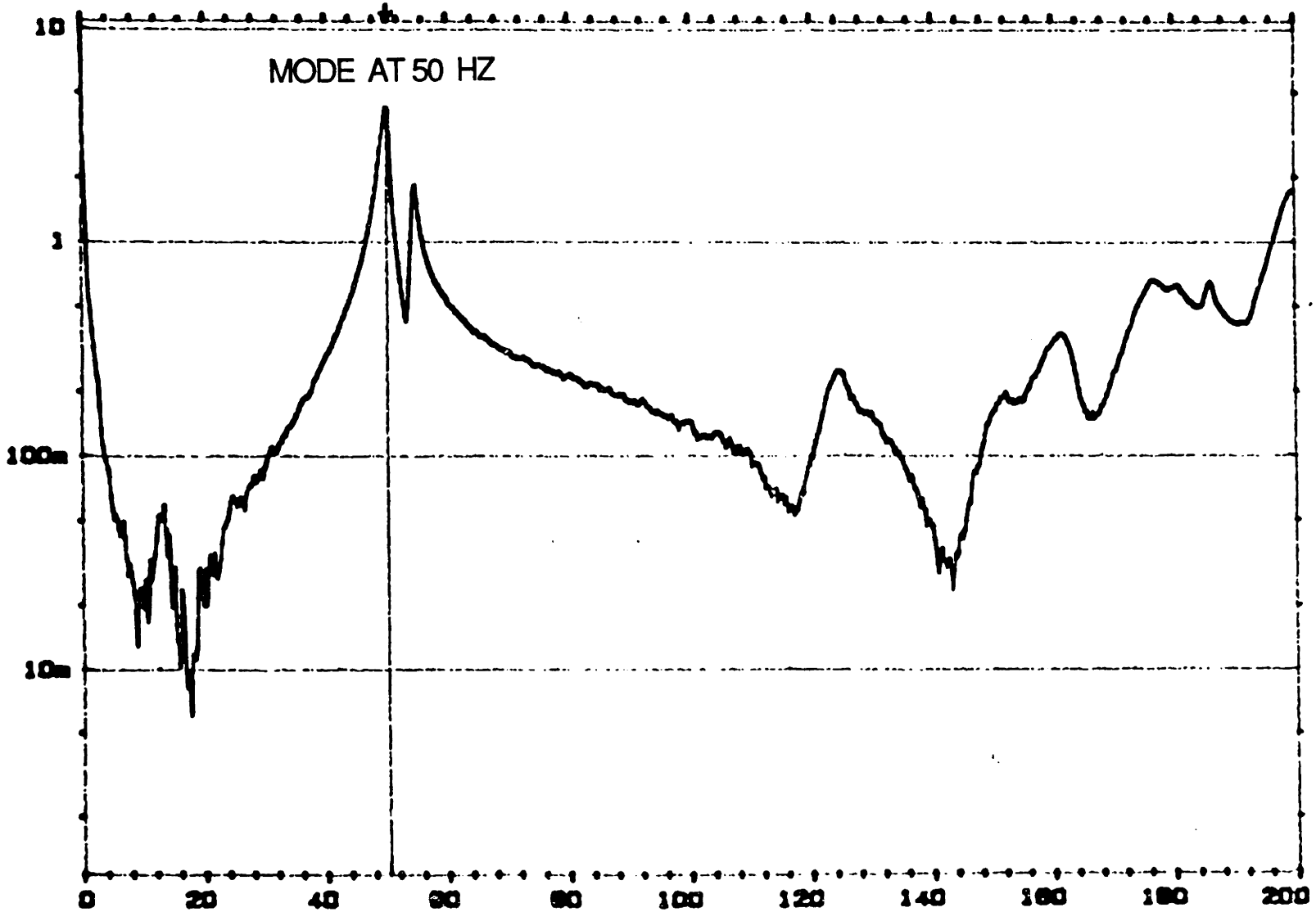

FIGURE C6 : TRANSFER FUNCTION (IN dB) FROM IMPULSE TEST
(Test # T1 , on the drill collar model in X direction)

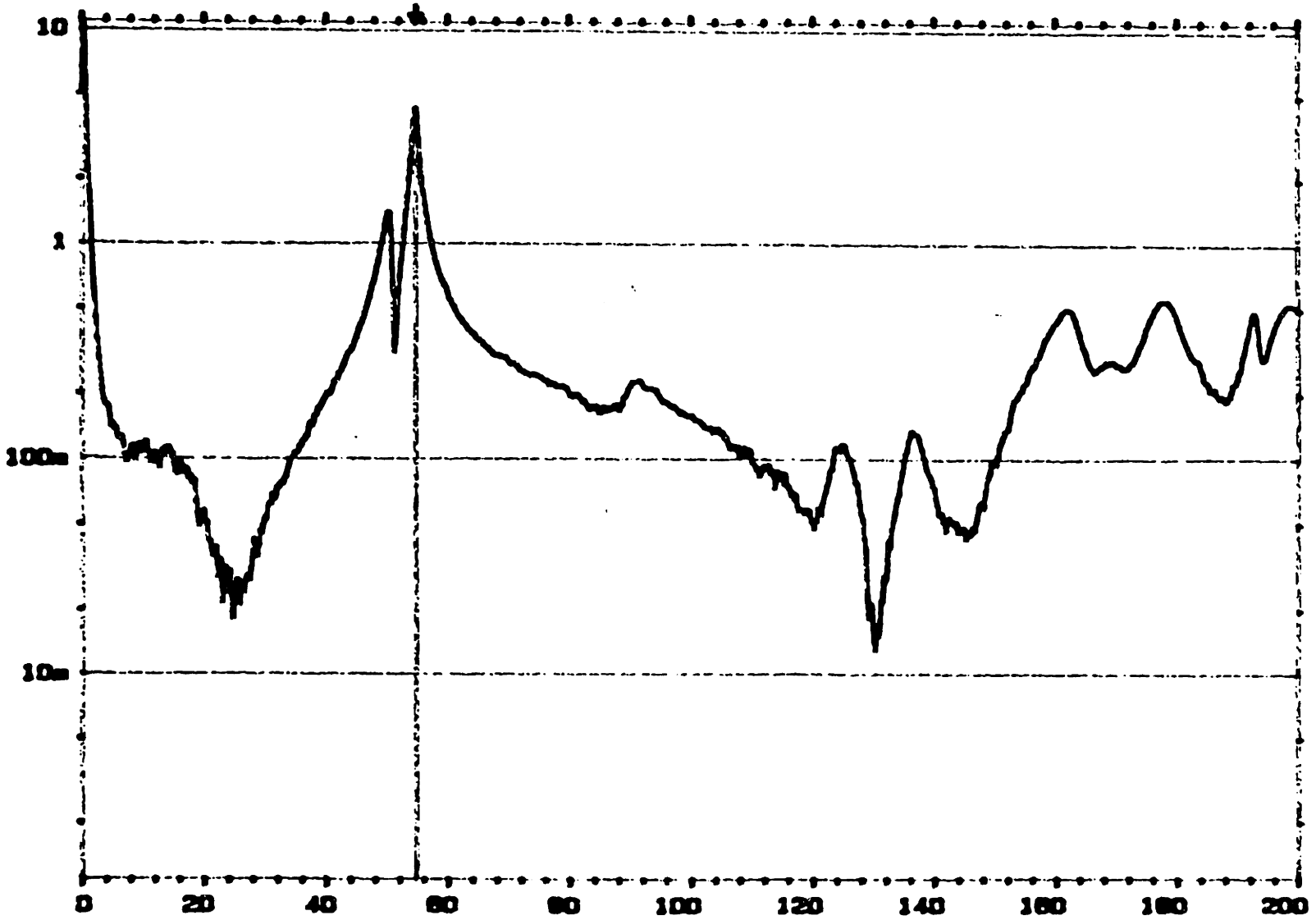

FIGURE C7 : TRANSFER FUNCTION (IN dB) FROM IMPULSE TEST
(Test # T 2 , on the drill collar model in y direction)

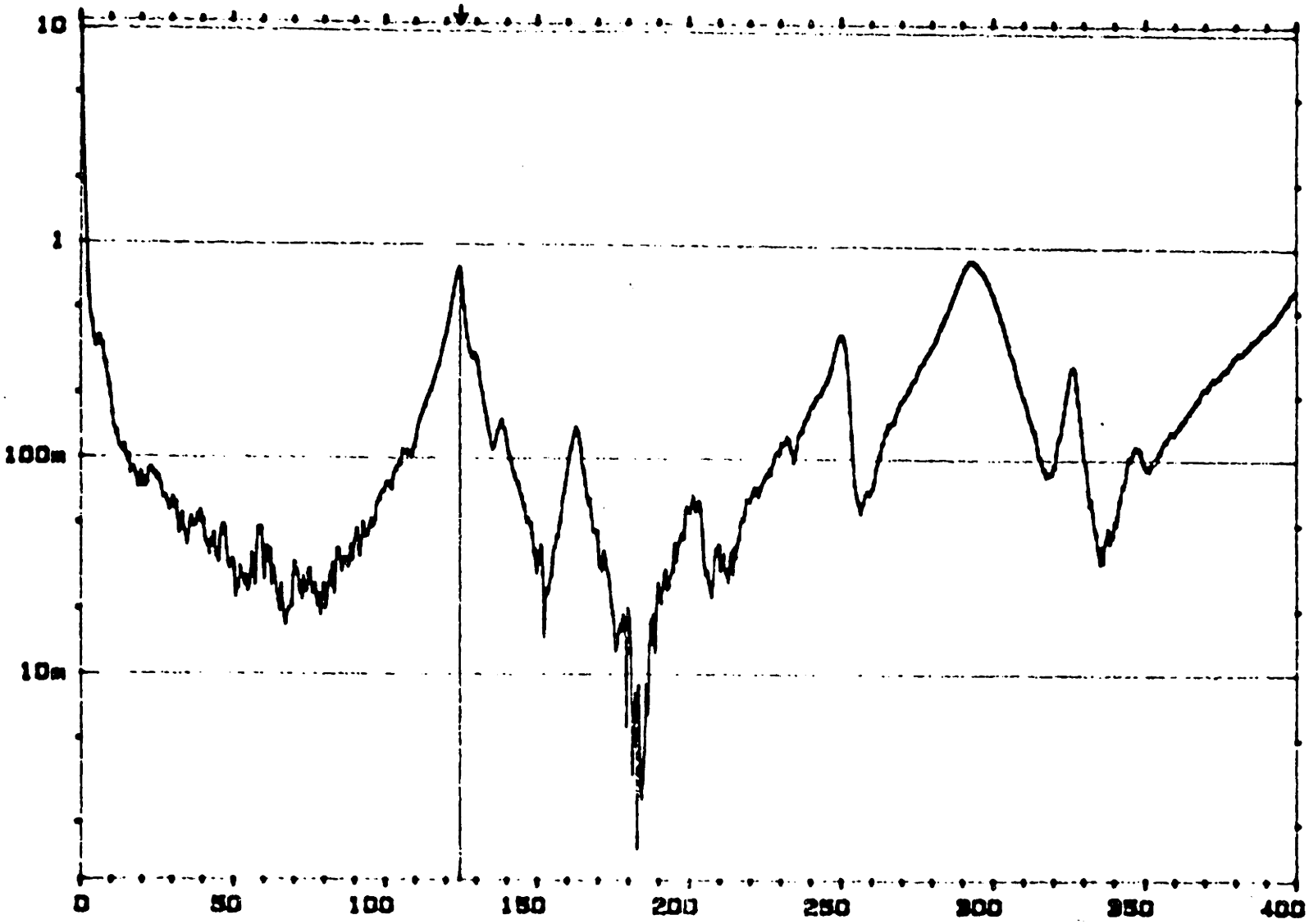

FIGURE C8 : TRANSFER FUNCTION (IN dB) FROM IMPULSE TEST
(Test # T7 , on the drill collar model casing)

APPENDIX D: DRILL COLLAR INPUT DATA

Based on the formulation presented in Chapter 6 a simple computer program was written to calculate the drill string response with/without rub. The inputs to this program are:

Length	= 59.2 feet
Collar outer diameter	= 7.00 inches
Collar inner diameter	= 2.810 inches
Hole diameter	= 8.75 inches
Mud density	= 11.000 ppg
Imbalance	= 0.010 feet
Coefficient of friction	= 0.30

APPENDIX E: ORBITAL PLOTS

TEST # 700

PLANAR MODEL (SPEEDING UP)
DRIVE SHAFT SPEED 14.1 HZ
DATA SAMPLED AT 500 HZ
100 POINTS PLOTTED
NO RUB

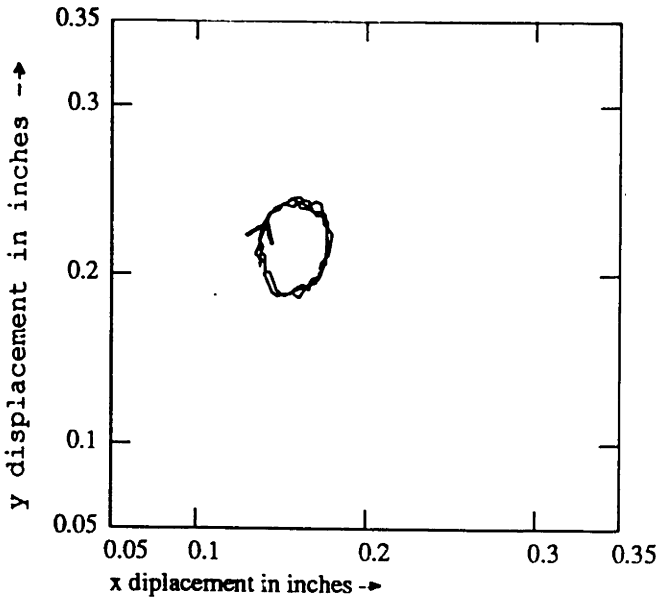

FIGURE # E 1

TEST # 701

PLANAR MODEL (SPEEDING UP)
DRIVE SHAFT SPEED 14.5 HZ
DATA SAMPLED AT 500 HZ
100 POINTS PLOTTED
PART RUB

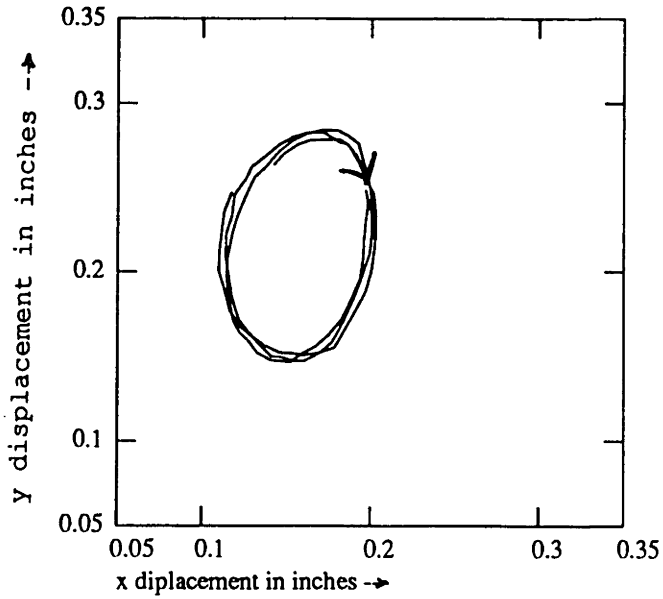

FIGURE # E 2

TEST # 702

PLANAR MODEL (SPEEDING UP)
DRIVE SHAFT SPEED 14.8 HZ
DATA SAMPLED AT 500 HZ
100 POINTS PLOTTED
PART RUB

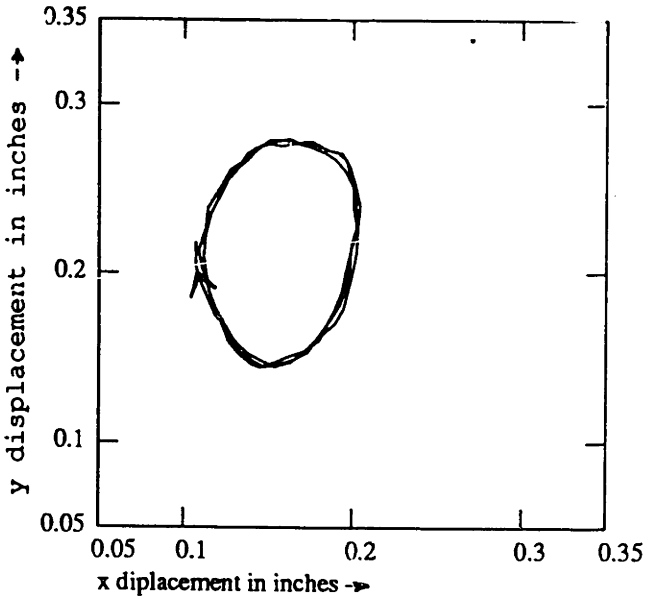

FIGURE # E 3

TEST # 703

PLANAR MODEL (SPEEDING UP)
DRIVE SHAFT SPEED 15.6 HZ
DATA SAMPLED AT 500 HZ
100 POINTS PLOTTED
FULL RUB

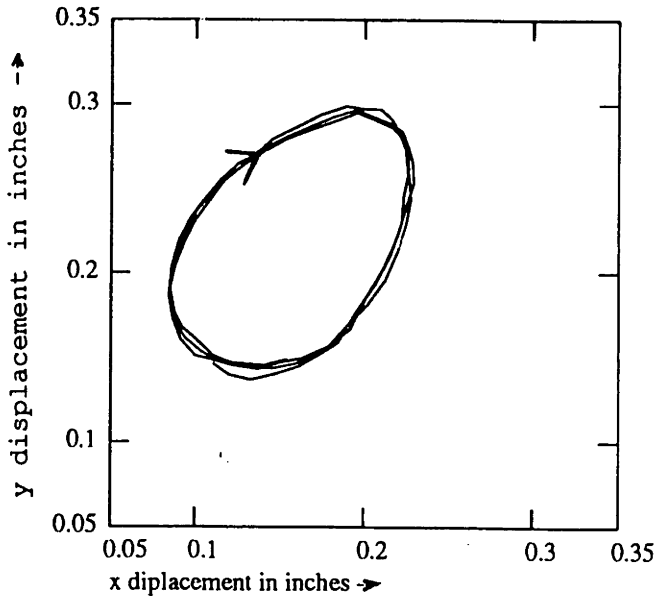

FIGURE # E 4

TEST # 704

PLANAR MODEL (SPEEDING UP)
DRIVE SHAFT SPEED 15.9 HZ
DATA SAMPLED AT 500 HZ
100 POINTS PLOTTED
FULL RUB, SOME WOBBLE

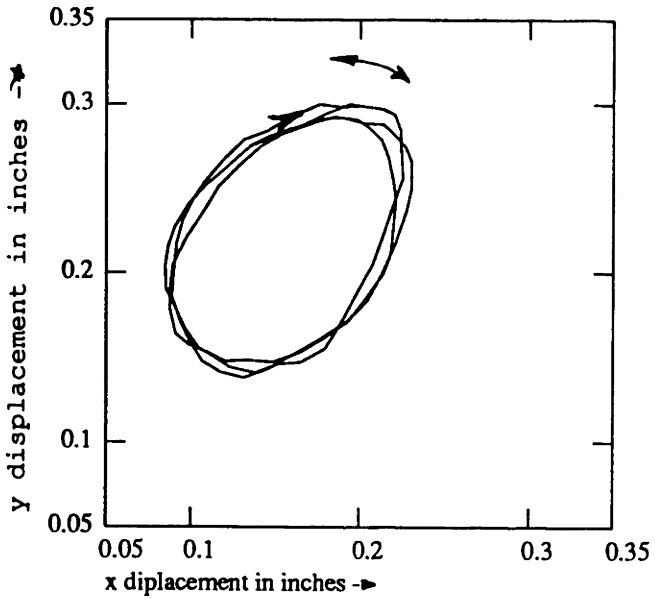

FIGURE # E 5

TEST # 705

PLANAR MODEL (SPEEDING UP)
DRIVE SHAFT SPEED 16.5 HZ
DATA SAMPLED AT 500 HZ
100 POINTS PLOTTED
FULL SYNCHONOUS RUB

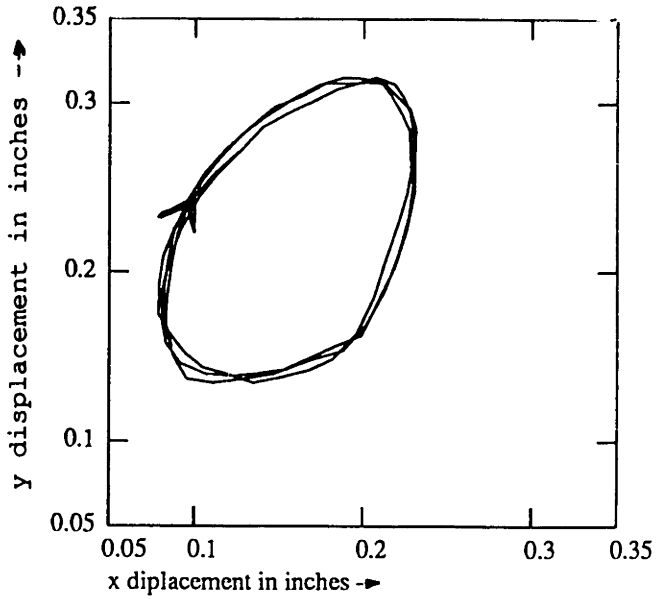

FIGURE # E 6

TEST # 706

PLANAR MODEL (SPEEDING UP)
DRIVE SHAFT SPEED 16.9 HZ
DATA SAMPLED AT 500 HZ
100 POINTS PLOTTED
FULL SYNCHRONOUS RUB

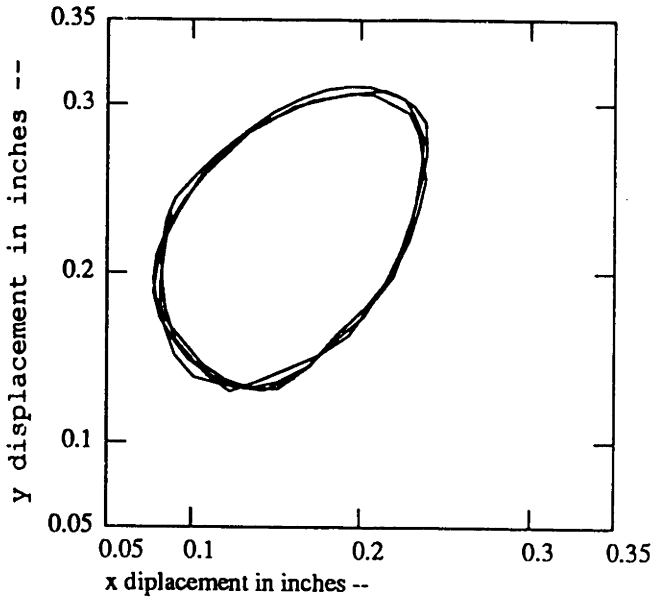

FIGURE # E 7

TEST # 708

PLANAR MODEL (SPEEDING UP)
DRIVE SHAFT SPEED 17.5 HZ
DATA SAMPLED AT 500 HZ
100 POINTS PLOTTED
FULL SYNCHRONOUS RUB

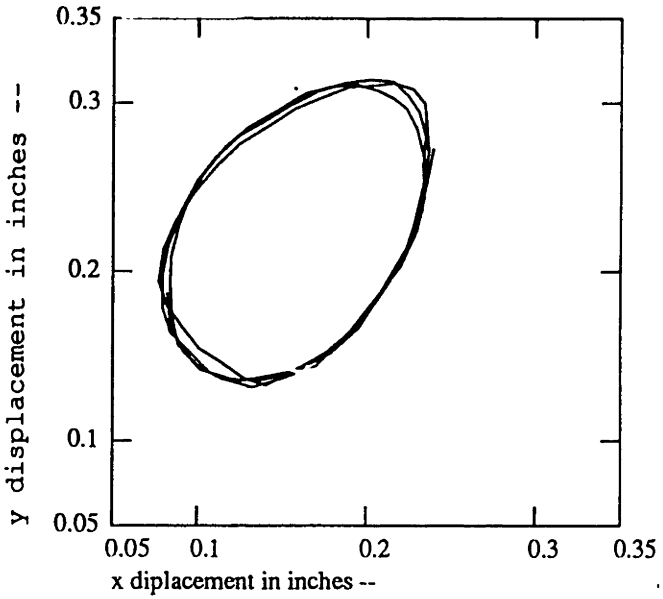

FIGURE # E 8

TEST # 707

PLANAR MODEL (SPEEDING UP)
DRIVE SHAFT SPEED 18.0 HZ
DATA SAMPLED AT 500 HZ
100 POINTS PLOTTED
PART RUB

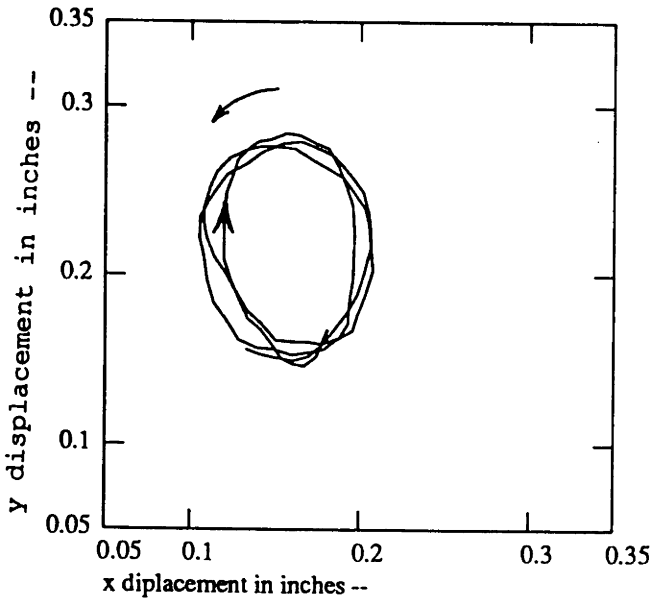

FIGURE # E 9

TEST # 709

PLANAR MODEL (SPEEDING UP)
DRIVE SHAFT SPEED 18.6 HZ
DATA SAMPLED AT 500 HZ
100 POINTS PLOTTED
PART RUB

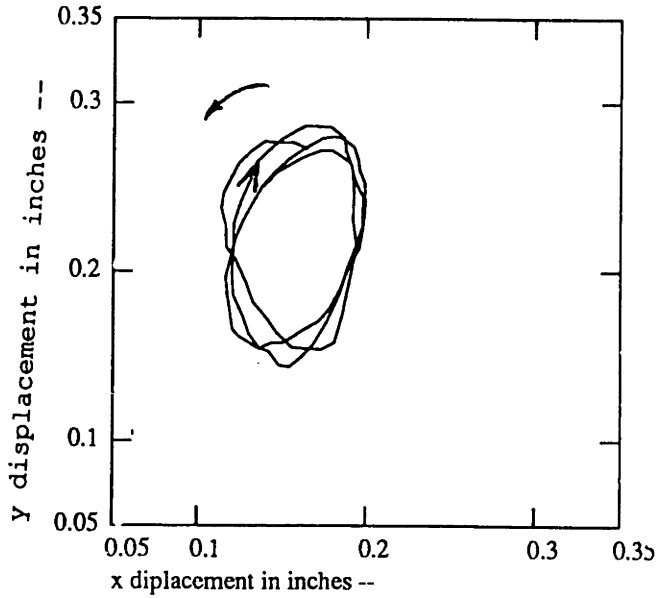

FIGURE # E 10

TEST # 710

PLANAR MODEL (SPEEDING UP)
DRIVE SHAFT SPEED 19.0 HZ
DATA SAMPLED AT 500 HZ
100 POINTS PLOTTED
PART RUB

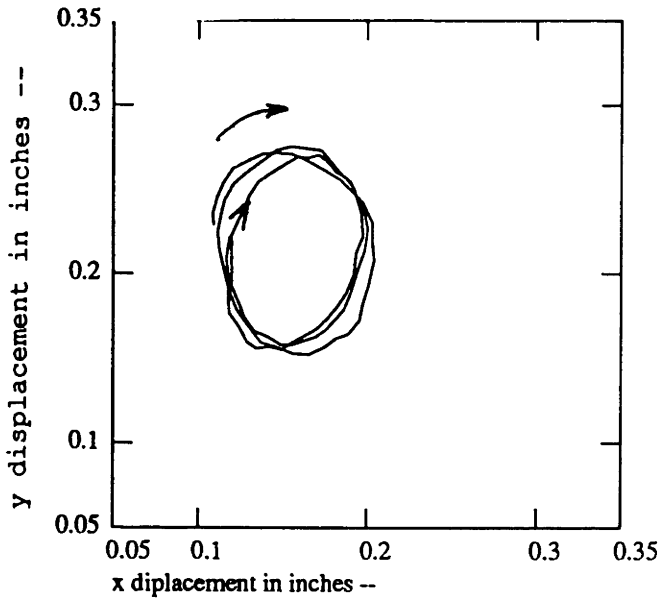

FIGURE # E 11

TEST # 711

PLANAR MODEL (SPEEDING UP)
DRIVE SHAFT SPEED 20.0 HZ
DATA SAMPLED AT 500 HZ
100 POINTS PLOTTED
PART RUB

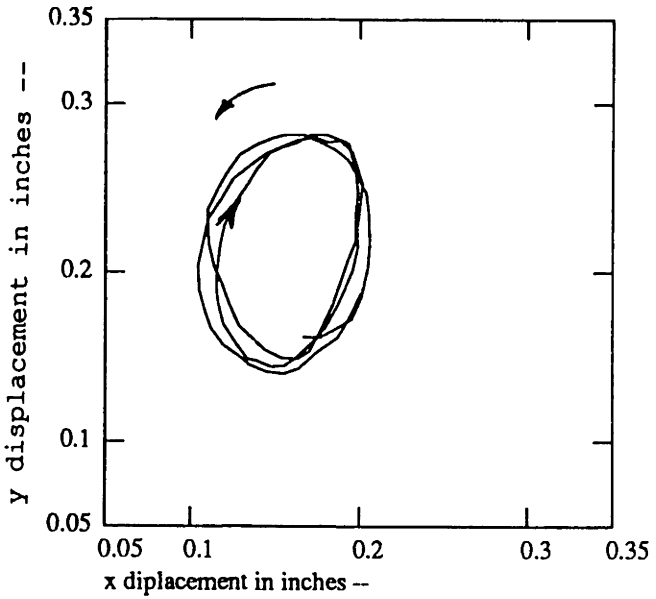

FIGURE # E 12

TEST # 712

PLANAR MODEL (PEAK SPEED)
DRIVE SHAFT SPEED 24.4 HZ
DATA SAMPLED AT 500 HZ
100 POINTS PLOTTED
MINIMAL RUB

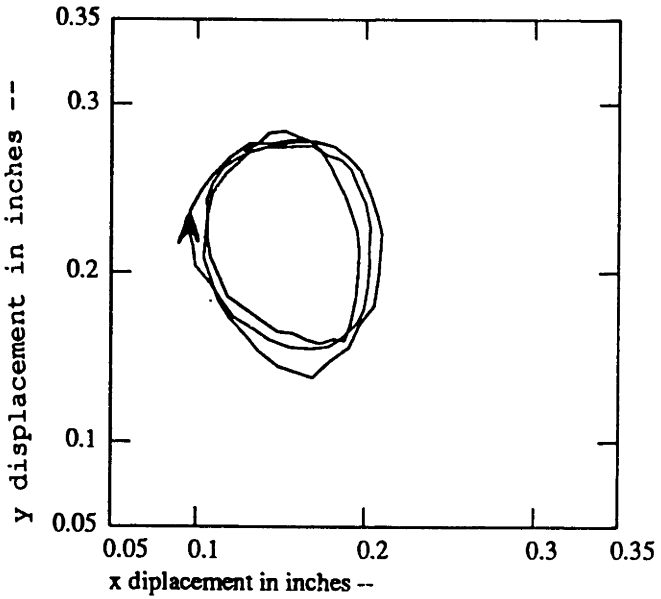

FIGURE # E 13

TEST # 713

PLANAR MODEL (SLOWING DOWN)
DRIVE SHAFT SPEED 20.4 HZ
DATA SAMPLED AT 500 HZ
100 POINTS PLOTTED
PART RUB

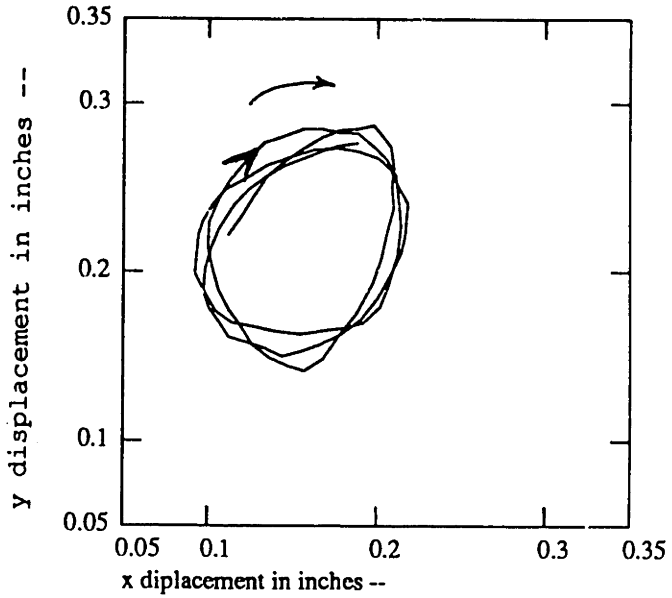

FIGURE # E 14

TEST # 714

PLANAR MODEL (SLOWING DOWN)
DRIVE SHAFT SPEED 19.1 HZ
DATA SAMPLED AT 500 HZ
100 POINTS PLOTTED
PART RUB

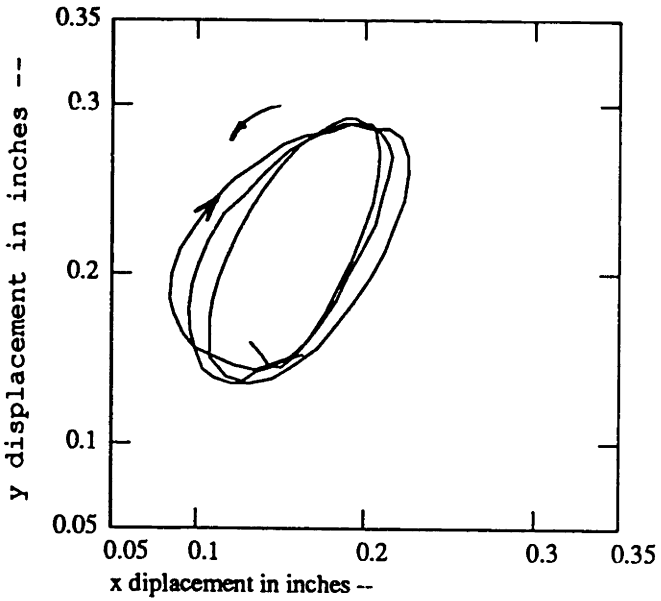

FIGURE # E 15

TEST # 715

PLANAR MODEL (SLOWING DOWN)
DRIVE SHAFT SPEED 18.6 HZ
DATA SAMPLED AT 500 HZ
100 POINTS PLOTTED
PART RUB

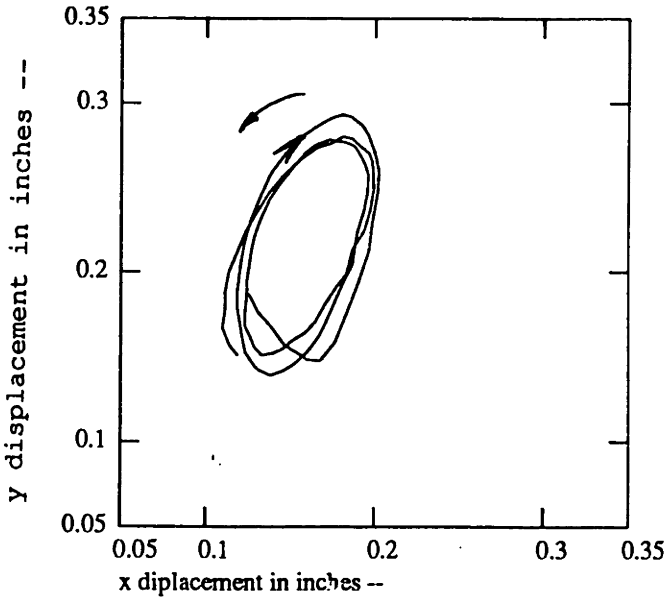

FIGURE # E 16

TEST # 716

PLANAR MODEL (SLOWING DOWN)
DRIVE SHAFT SPEED 17.8 HZ
DATA SAMPLED AT 200 HZ
40 POINTS PLOTTED
PART RUB

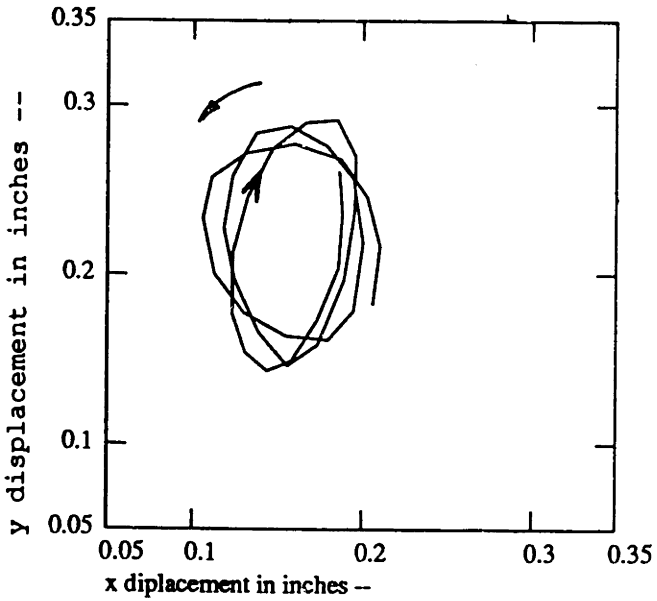

FIGURE # E 17

TEST # 717

PLANAR MODEL (SLOWING DOWN)
DRIVE SHAFT SPEED 17.5 HZ
DATA SAMPLED AT 200 HZ
40 POINTS PLOTTED
PART RUB

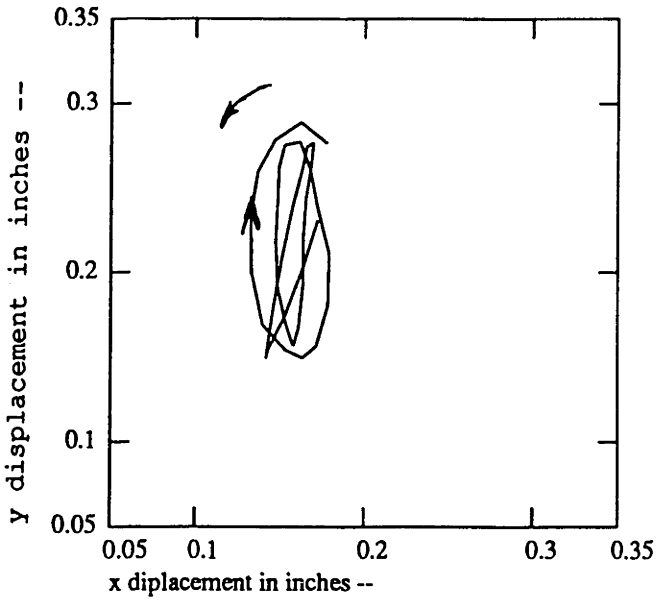

FIGURE # E 18

TEST # 718

PLANAR MODEL (SLOWING DOWN)
DRIVE SHAFT SPEED 17.1 HZ
DATA SAMPLED AT 200 HZ
40 POINTS PLOTTED
PART RUB

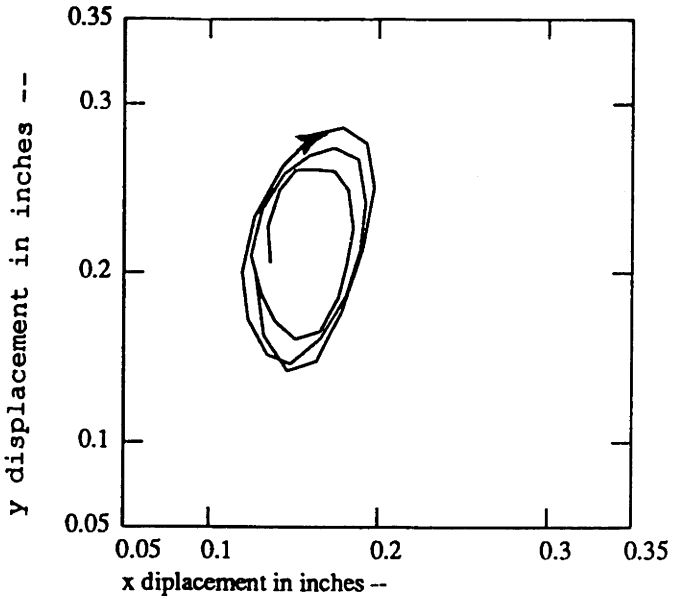

FIGURE # E 19

TEST # 719

PLANAR MODEL (SLOWING DOWN)
DRIVE SHAFT SPEED 15.5 HZ
DATA SAMPLED AT 200 HZ
40 POINTS PLOTTED
FULL SYNCHRONOUS RUB

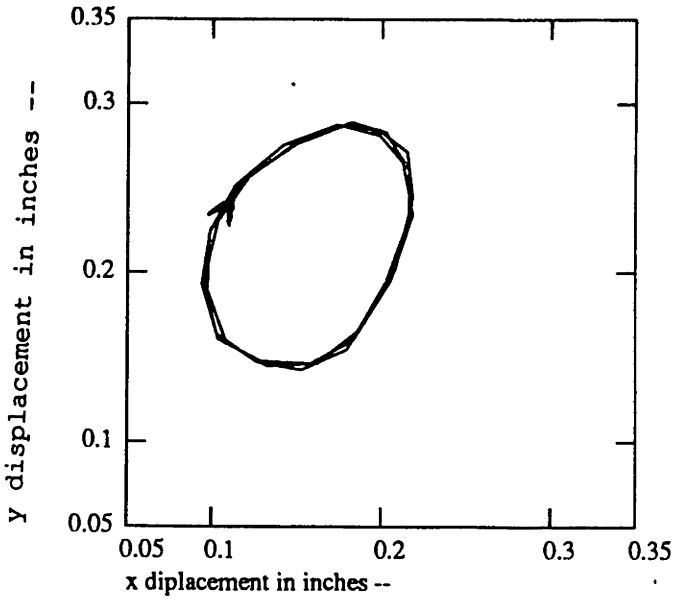

FIGURE # E 20

TEST # 720

PLANAR MODEL (SLOWING DOWN)
DRIVE SHAFT SPEED 14.8 HZ
DATA SAMPLED AT 200 HZ
40 POINTS PLOTTED
PART RUB

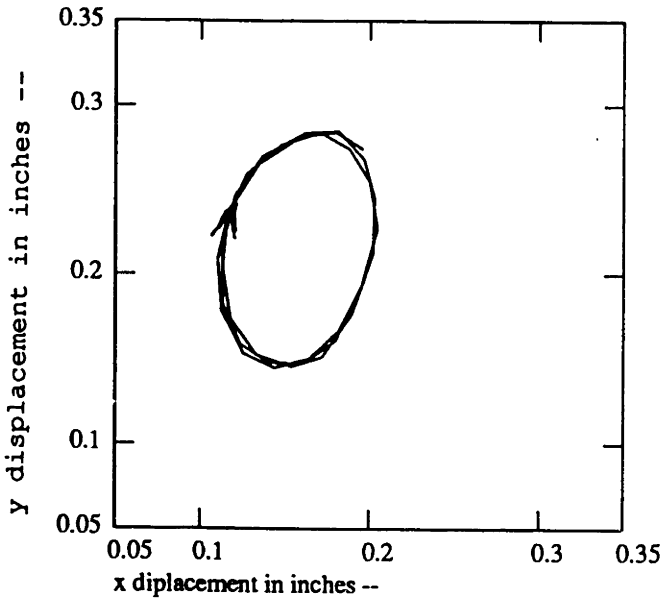

FIGURE # E 21

TEST # 721

PLANAR MODEL (SLOWING DOWN)
DRIVE SHAFT SPEED 14.4 HZ
DATA SAMPLED AT 200 HZ
40 POINTS PLOTTED
MINIMAL RUB

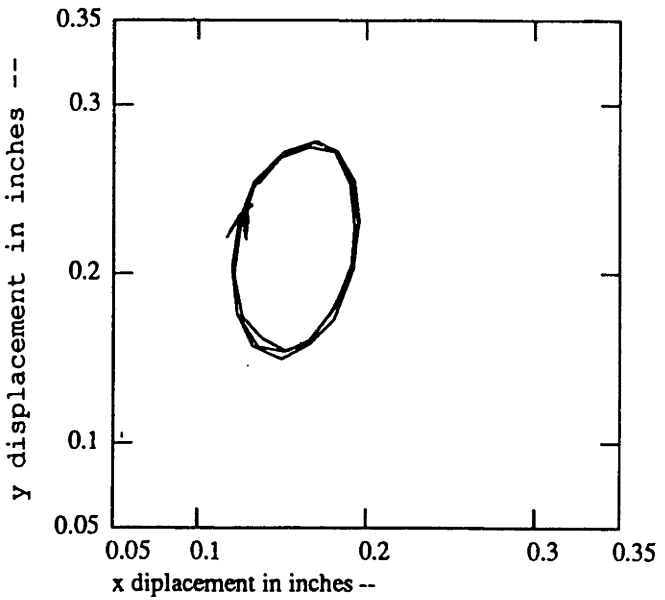

FIGURE # E 22

TEST # 722

PLANAR MODEL (SLOWING DOWN)
DRIVE SHAFT SPEED 13.5 HZ
DATA SAMPLED AT 200 HZ
40 POINTS PLOTTED
NO RUB

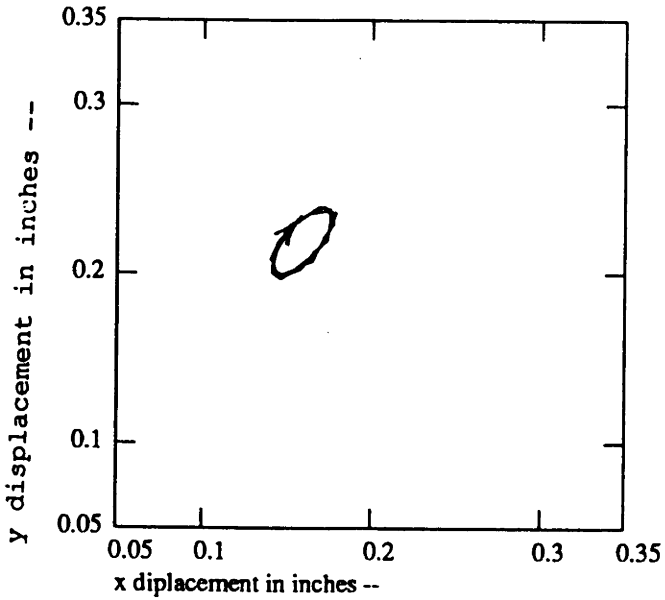

FIGURE # E 23

Test # 202

Drill Collar Model In Air
Drive Speed 12.8 Hz (Speeding up)
Data Sampled at 500 Hz
40 Points Plotted
Ordinate : Y displacement in inches

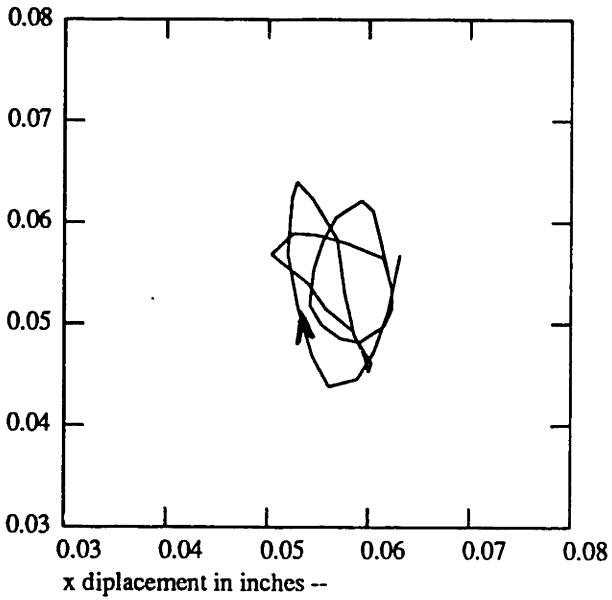

FIGURE # : E 24

Test # 203

Drill Collar Model In Air
Drive Speed 17.5 Hz (Speeding up)
Data Sampled at 500 Hz
40 Points Plotted
Ordinate : Y displacement in inches

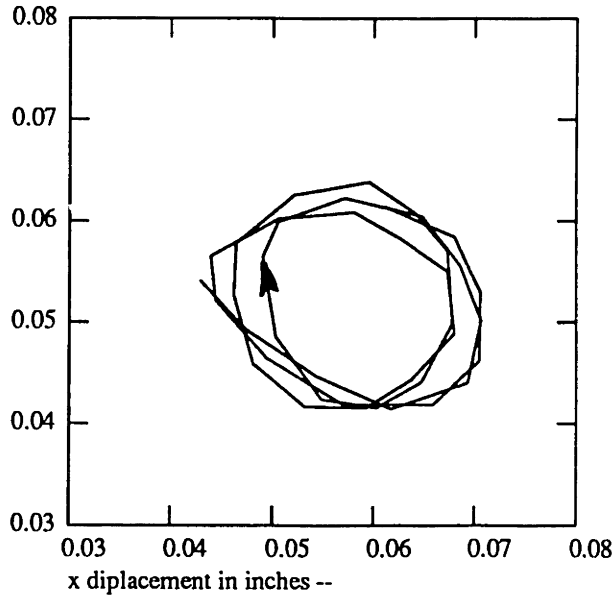

FIGURE # : E 25

Test # 204

Drill Collar Model In Air
Drive Speed 20.2 Hz (Speeding up)
Data Sampled at 500 Hz
40 Points Plotted
Ordinate : Y displacement in inches

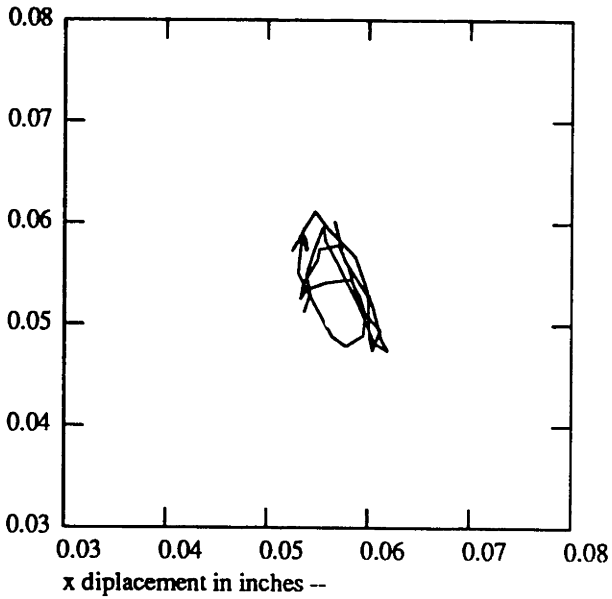

FIGURE # : E 26

Test # 205

Drill Collar Model In Air
Drive Speed 30.0 Hz (Speeding up)
Data Sampled at 500 Hz
40 Points Plotted
Ordinate : Y displacement in inches

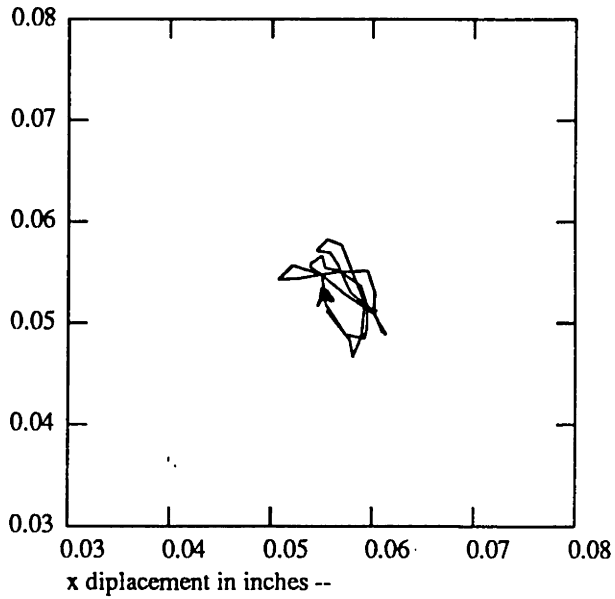

FIGURE # : E 27

Test # 206

Drill Collar Model In Air
Drive Speed 43.0 Hz (Speeding up)
Data Sampled at 500 Hz
40 Points Plotted
Ordinate : Y displacement in inches

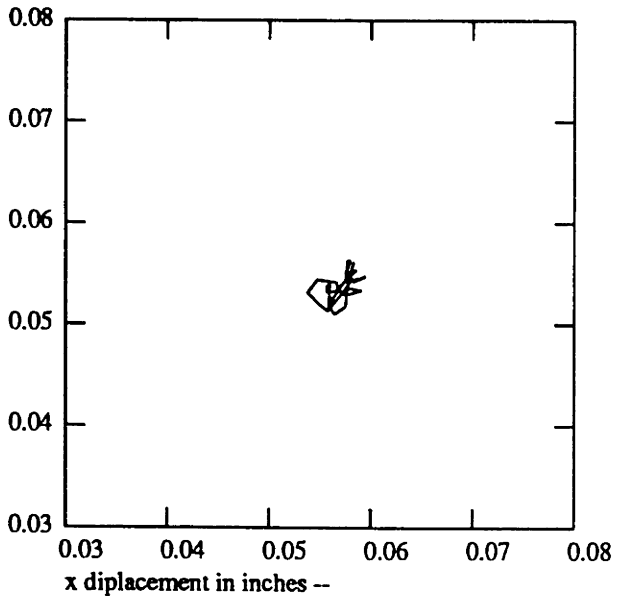

FIGURE # : E 28

Test # 207

Drill Collar Model In Air
Drive Speed 52.0 Hz (Speeding up)
Data Sampled at 500 Hz
40 Points Plotted
Ordinate : Y displacement in inches

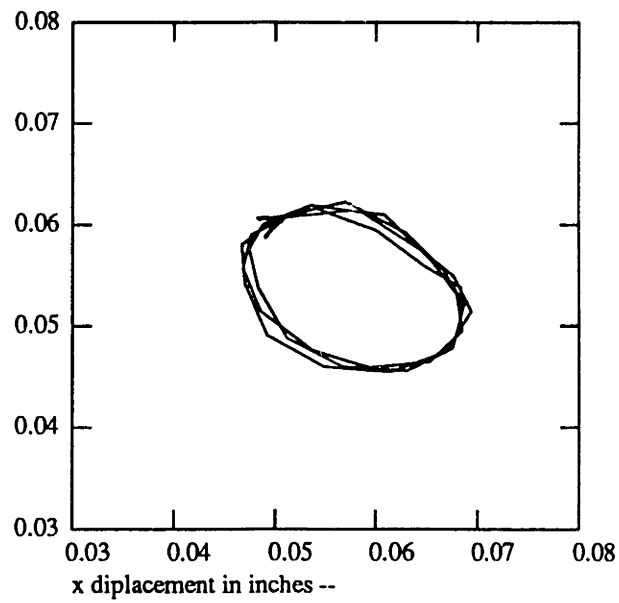

FIGURE # : E 29

Test # 208

Drill Collar Model In Air
Drive Speed 68.0 Hz (Peak Speed)
Data Sampled at 500 Hz
40 Points Plotted
Ordinate : Y displacement in inches

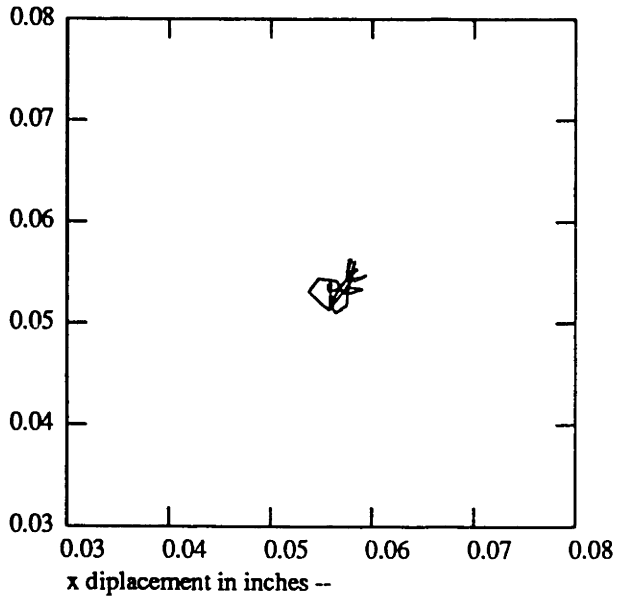

FIGURE # E 30

Test # 209

Drill Collar Model In Air
Drive Speed 55.0 Hz (Slowing down)
Data Sampled at 500 Hz
40 Points Plotted
Ordinate : Y displacement in inches

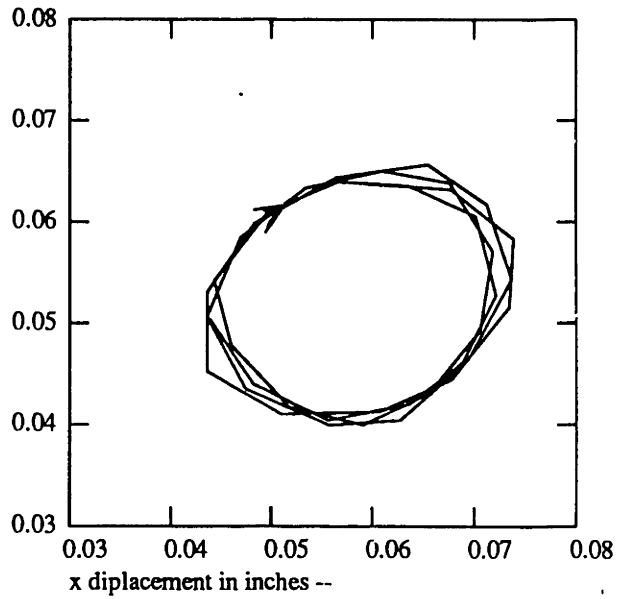

FIGURE # : E 31

Test # 210

Drill Collar Model In Air
Drive Speed 42.0 Hz (Slowing down)
Data Sampled at 500 Hz
40 Points Plotted
Ordinate : Y displacement in inches

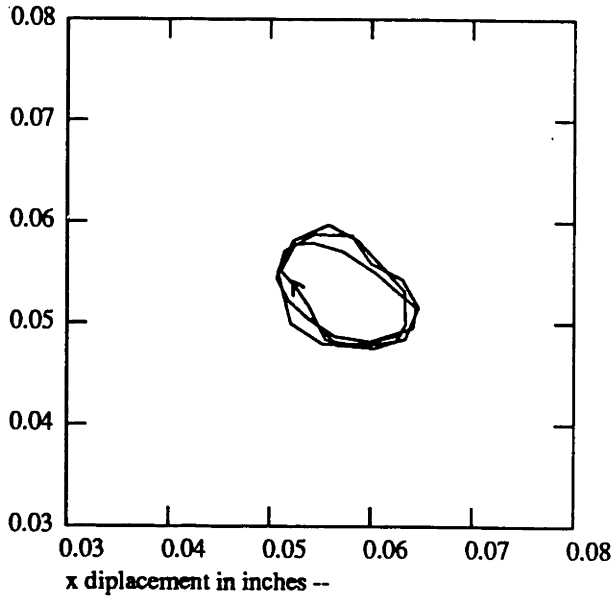

FIGURE # : E 32

Test # 211

Drill Collar Model In Air
Drive Speed 30.0 Hz (Slowing down)
Data Sampled at 500 Hz
40 Points Plotted
Ordinate : Y displacement in inches

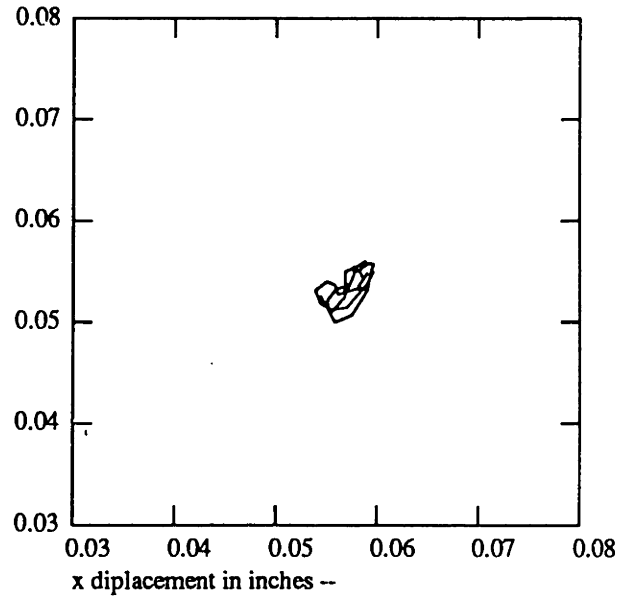

FIGURE # : E 33

Test # 212

Drill Collar Model In Air
Drive Speed 20.0 Hz (Slowing down)
Data Sampled at 500 Hz
40 Points Plotted
Ordinate : Y displacement in inches

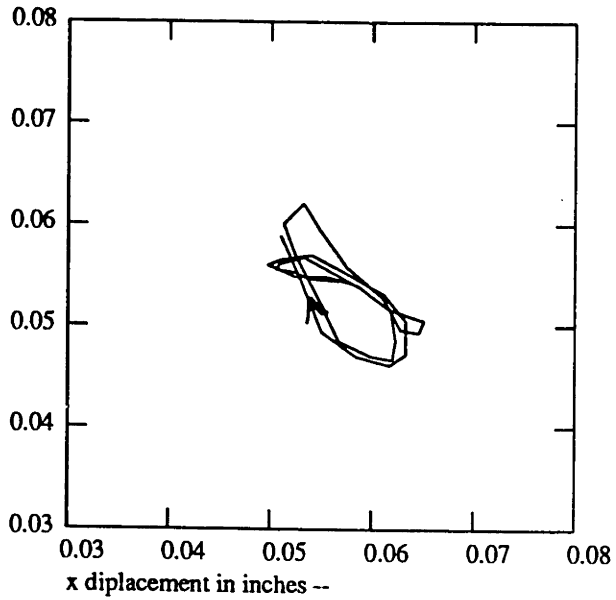

FIGURE # : E 34

Test # 213

Drill Collar Model In Air
Drive Speed 15.0 Hz (Slowing down)
Data Sampled at 500 Hz
40 Points Plotted
Ordinate : Y displacement in inches

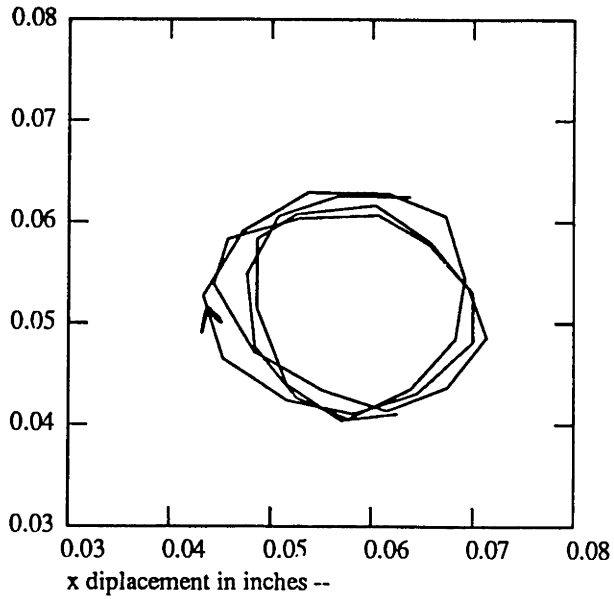

FIGURE # : E 35

Test # 214

Drill Collar Model In Air
Drive Speed 12.8 Hz (slowing down)
Data Sampled at 500 Hz
40 Points Plotted
Ordinate : Y displacement in inches

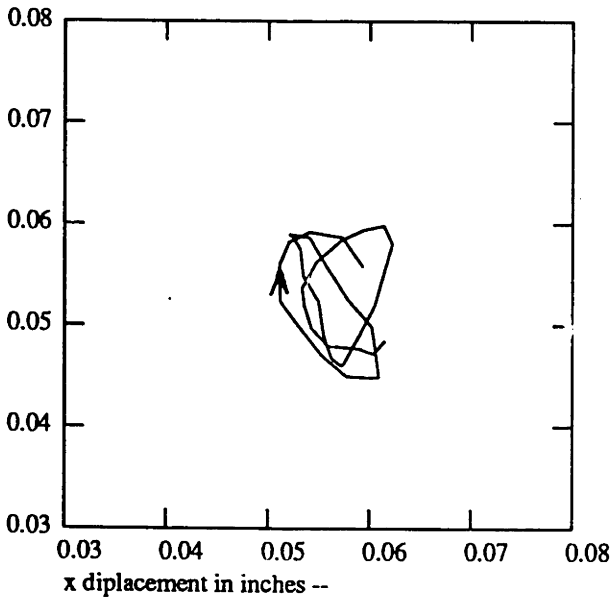

FIGURE # : E 36

Test # 215

Drill Collar Model In Water
Drive Speed 9.5 Hz (Speeding up)
Data Sampled at 500 Hz
40 Points Plotted
Ordinate : Y displacement in inches

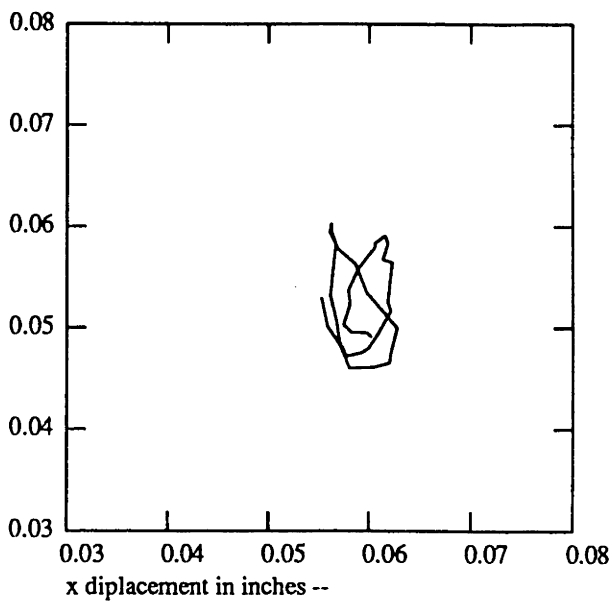

FIGURE # : E 37

Test # 216

Drill Collar Model In Water
Drive Speed 13.0 Hz (Speeding up)
Data Sampled at 500 Hz
40 Points Plotted
Ordinate : Y displacement in inches

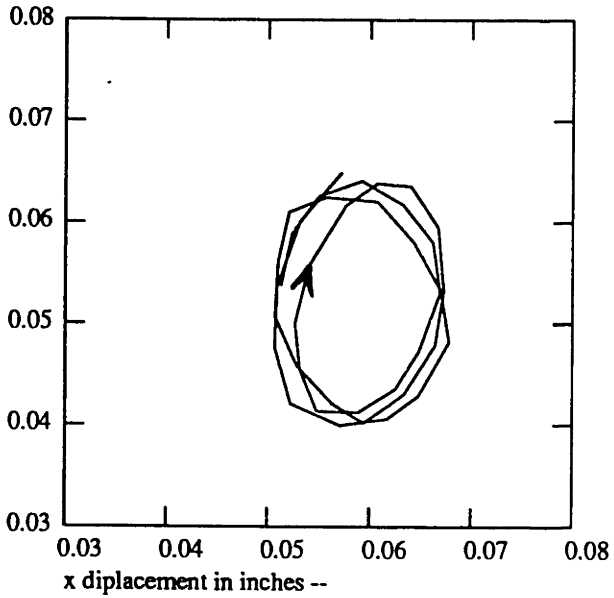

FIGURE # : E 38

Test # 217

Drill Collar Model In Water
Drive Speed 20.0 Hz (Speeding up)
Data Sampled at 500 Hz
40 Points Plotted
Ordinate : Y displacement in inc s

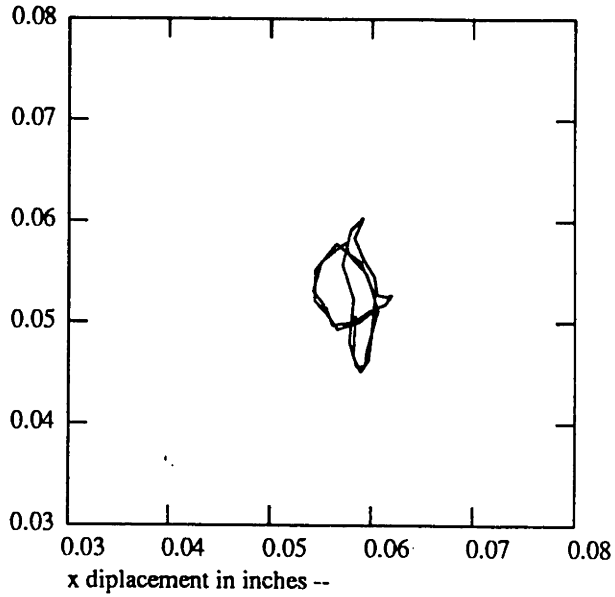

FIGURE # : E 39

Test # 218

Drill Collar Model In Water
Drive Speed 28.0 Hz (Speeding up)
Data Sampled at 500 Hz
40 Points Plotted
Ordinate : Y displacement in inches

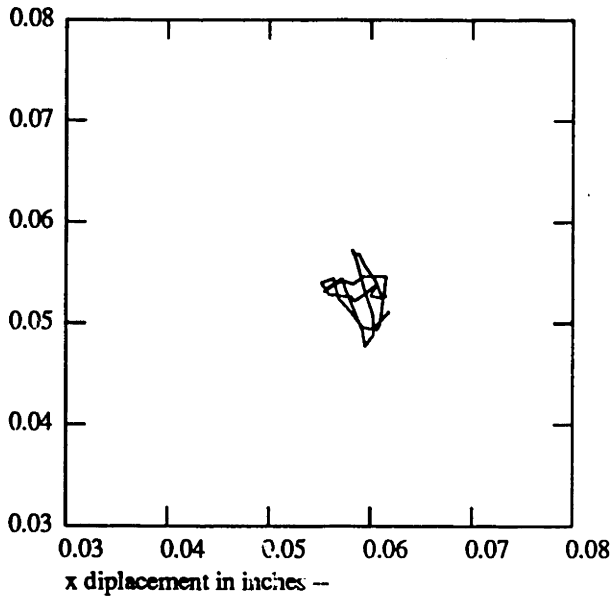

FIGURE # E 40

Test # 219

Drill Collar Model In Water
Drive Speed 38.6 Hz (Speeding up)
Data Sampled at 500 Hz
40 Points Plotted
Ordinate : Y displacement in inches

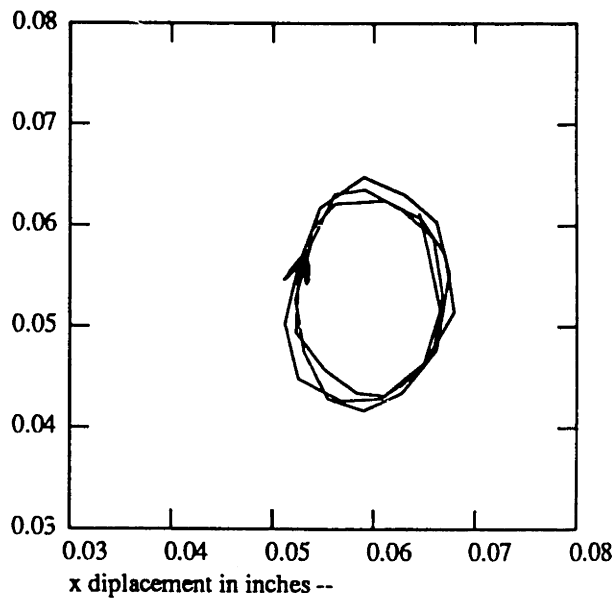

FIGURE #: E 41

Test # 221

Drill Collar Model In Water
Drive Speed 46.0 Hz (Slowing Down)
Data Sampled at 500 Hz
40 Points Plotted
Ordinate : Y displacement in inches

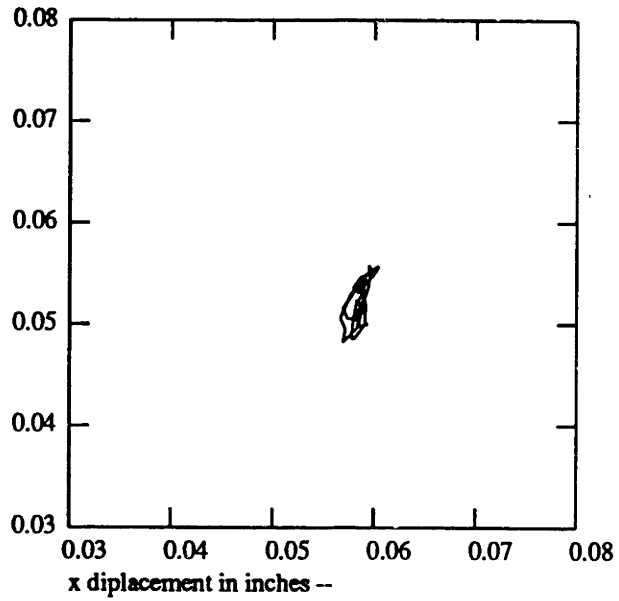

FIGURE # : E 42

Test # 220

Drill Collar Model In Water
Drive Speed 53.0 Hz (Peak Speed)
Data Sampled at 500 Hz
40 Points Plotted
Ordinate : Y displacement in inches

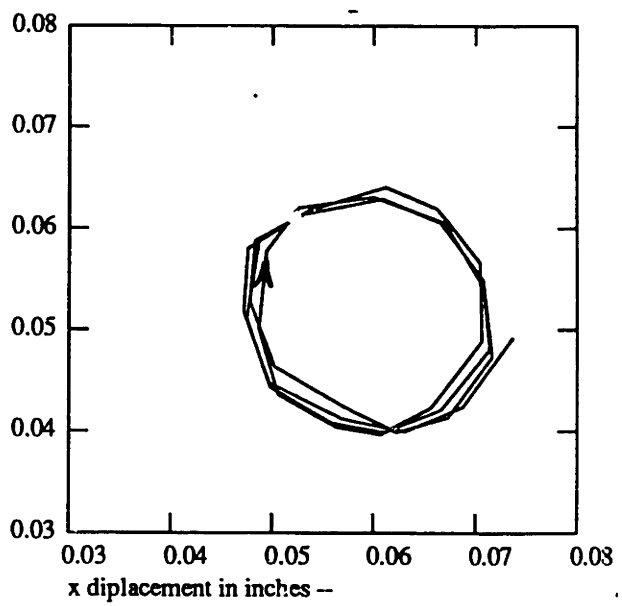

FIGURE # : E 43

Test # 222

Drill Collar Model In Water
Drive Speed 32.0 Hz (Slowing Down)
Data Sampled at 500 Hz
40 Points Plotted
Ordinate : Y displacement in inches

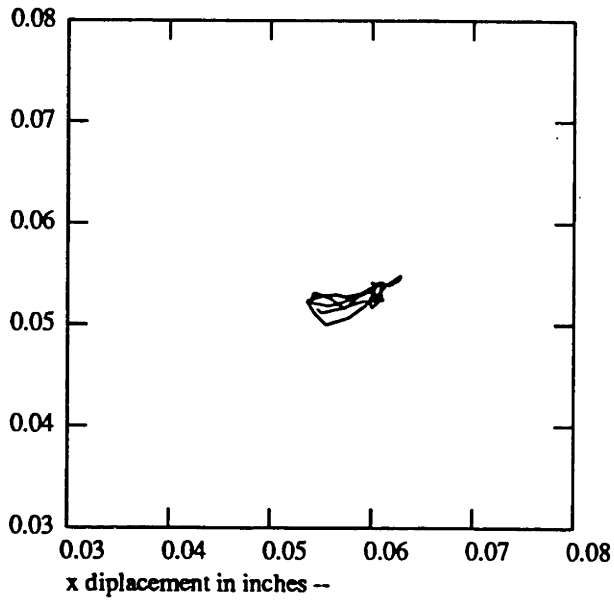

FIGURE # : E 44

Test # 223

Drill Collar Model In Water
Drive Speed 19.4 Hz (Slowing Down)
Data Sampled at 500 Hz
40 Points Plotted
Ordinate : Y displacement in inches

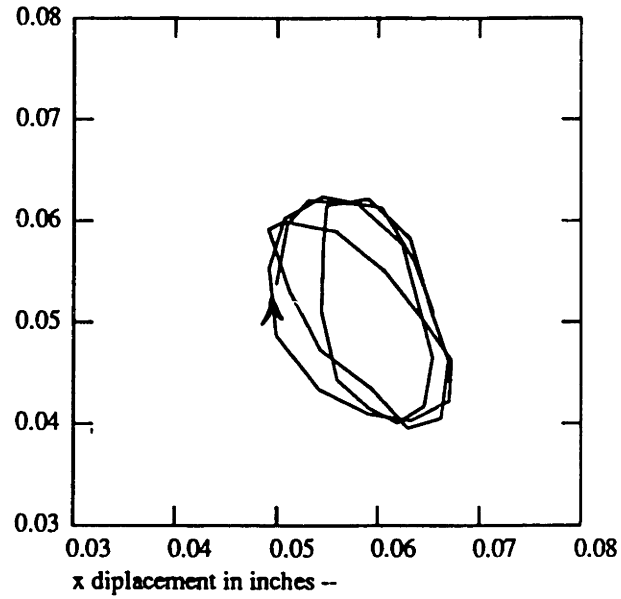

FIGURE # : E 45

Test # 224

Drill Collar Model In Water
Drive Speed 15.0 Hz (Slowing Down)
Data Sampled at 500 Hz
40 Points Plotted
Ordinate : Y displacement in inches

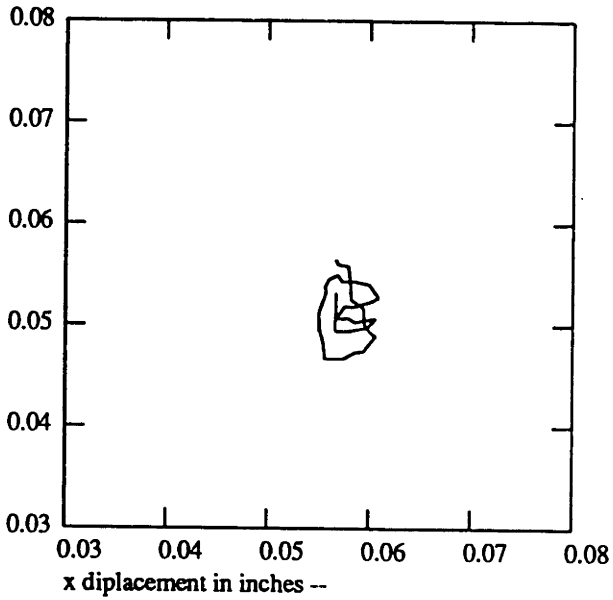

FIGURE # : E 46

Test # 225

Drill Collar Model In Water
Drive Speed 13.5 Hz (Speed up)
Data Sampled at 500 Hz
40 Points Plotted
Ordinate : Y displacement in inches

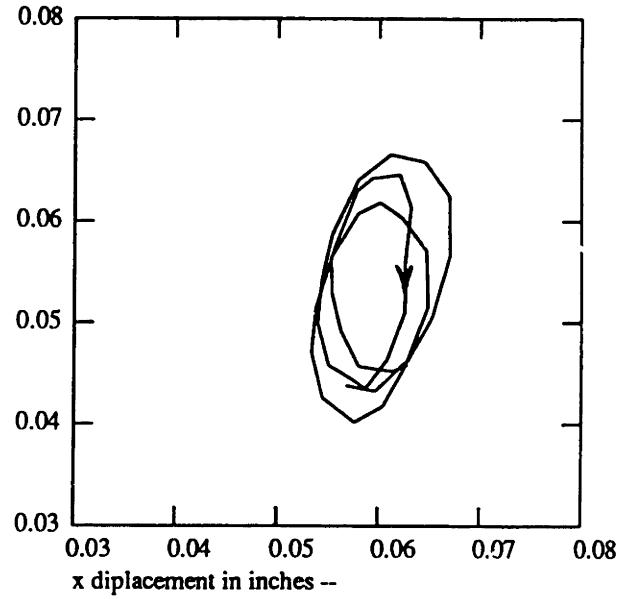

FIGURE # : E 47

Test # 226

Drill Collar Model In Water
Drive Speed 16.0 Hz (Peak Speed)
↑VData Sampled at 500 Hz
40 Points Plotted
Ordinate : Y displacement in inches

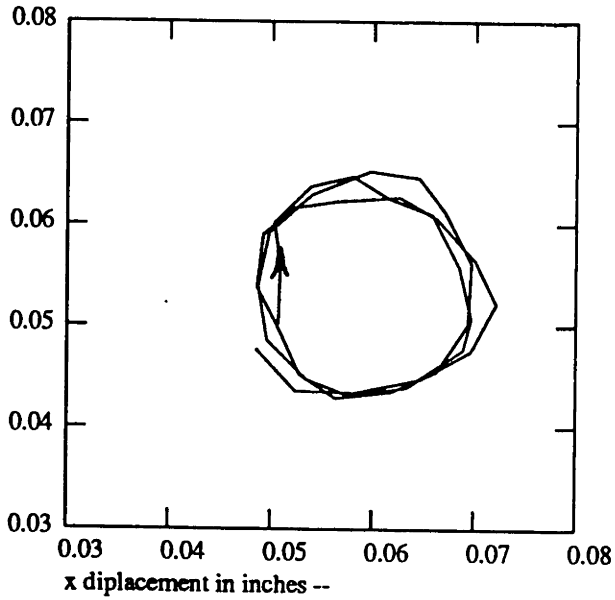

FIGURE # : E 48

Test # 227

Drill Collar Model In Water
Drive Speed 10.0 Hz (Slowing Down)
Data Sampled at 500 Hz
40 Points Plotted
Ordinate : Y displacement in inches

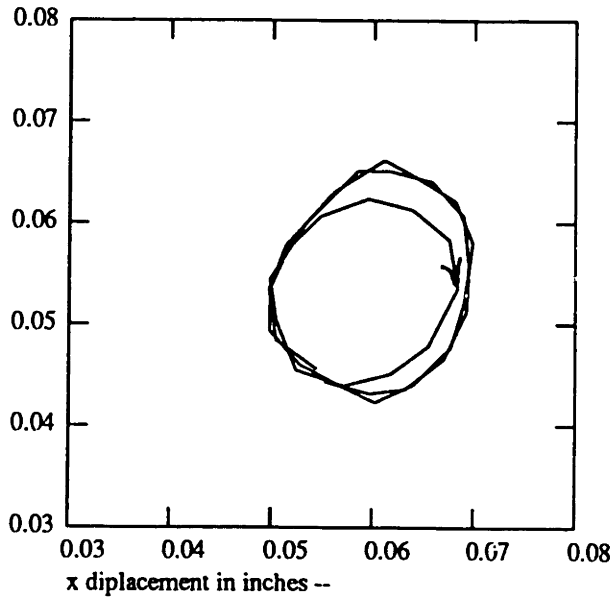

FIGURE # : E 49